ABSTRACT

Title of dissertation: NANOSCALE BEHAVIOR OF 90° DOMAINS IN FERROELECTRIC FILMS

Zhengkun Ma, Doctor of Philosophy, 2005

Dissertation directed by: Professor Alexander L. Roytburd
Department of Materials Science and Engineering
Professor John Melngailis
Department of Materials Science and Engineering

Investigation of ferroelectric and piezoelectric properties of ferroelectric films at nanoscale is not only of fundamental interest, but also critical to their applications as non-volatile ferroelectric memories and as microsensors and microactuators for microelectromechanical systems. Both intrinsic and extrinsic effects play a role in determining film properties. Although the extrinsic contribution from non-180° domain wall motion can be comparable to the intrinsic lattice contribution in bulk materials, this effect is largely suppressed in polycrystalline films because of film clamping by a substrate and pinning of 90° domain walls by defects.

Taking into account that integration of high quality ferroelectric films onto silicon based substrate is very important for the microelectronic industry, we choose the $PbZr_{0.2}Ti_{0.8}O_3$ film epitaxially grown on Si substrate by pulsed laser deposition to study the 90° domain behavior in the continuous films as well as in patterned islands, which can be used as nanodevices. The goal is to investigate the mobility of

90° domain walls and to determine their extrinsic contribution to the piezoelectric response of the epitaxial islands with reduced substrate clamping depending on island geometry.

The cubic and the strip-like islands have been fabricated from sub-micron films by focused ion beam milling. Ferroelectric and piezoelectric measurements on patterned structures with top electrodes have demonstrated the dramatic enhancement of their piezoresponse in comparison with a continuous film. Piezoelectric force microscopy has revealed highly mobile two-domain structure in the strip-like islands which show the maximumal piezoresponse. The intrinsic piezoelectric response of the patterned structure with an immobile polydomain structure is modelled using finite element analysis. The difference between the experimental measured and calculated piezoeffect has allowed us to estimate a large extrinsic contribution from the domain walls movement in the patterned structures. The study of patterned structures together with additional observations of the domain wall movement under local electric field in continuous films allow us to conclude that a relative small extrinsic effect in the continuous films is a result of the elastic substrate clamping rather than the domain wall pinning. Thus, the contribution of domain wall movement can be increased by engineering special domain architectures, for example, the plane-parallel domains in a film, which are patterned into the thin strips.

NANOSCALE BEHAVIOR OF 90° DOMAINS IN FERROELECTRIC FILMS

by

Zhengkun Ma

Dissertation submitted to the Faculty of the Graduate School of the
University of Maryland, College Park in partial fulfillment
of the requirements for the degree of
Doctor of Philosophy
2005

Advisory Committee:

Professor Alexander L. Roytburd, Chairman/Advisor
Professor John Melngailis, co-advisor
Professor Theodore L. Einstein, Dean's representative
Professor Manfred Wuttig
Professor Ichiro Takeuchi
Adjunct Professor James R. Cullen

DEDICATION

for my parents, my husband and my daughter.

ACKNOWLEDGEMENTS

I would like to express my sincere thanks to my dissertation advisors: Professor Alexander Roytburd and Professor John Melngailis. This research work would not has been realized without their combined academic and financial support over the years of my graduate study. I would like to begin my thanking by Professor Professor Alaxander Roytburd who introduced me the to the exciting field of ferroelectricity and advised me with the riches of his theoretical knowledge. His enthusiasm for research and devotion to science always inspire me and direct me during my research work. I will always remember his creative guidance and constructive criticism. I would like to thank John Melngailis who give me the opportunity to work in his group and create a great work environment. Thanks for all the encouragement and good advice throughout the thesis work. His enthusiasm and collaborative spirit as well as amazingly broad knowledge are truly invaluable for my future career.

I would like to thank Professor Ramesh for his guidance and technical insight throughout this project. His never-satisfied desire for perfection will always inspire me.

Particular gratitude goes to John Barry, who have helped me learn various aspects of focused ion beam technique. I am truly grateful for the valuable ideas he gave me during my experiments. I would like to thank Nolan Ballow for teaching me and helping me on the clean room techniques.

I would like to thank Jun Ouyang who helped me on PFM imaging and piezoelectric property measurement. Thanks for revising my papers and for the fruitful discussions during my research work. I would like to thank Jianhua Li who helped me on the measurements conducted at NIST. Special thanks to Lang Chen who helped me revise my paper and gave me many constructive suggestions.

I would like to thank Florin Zavaliche who helped me on PFM imaging characterization, Tong Zhao who helped me prepare the PZT samples, Haimei Zheng who helped me on TEM work, Junling Wang who trained me and helped me on XRD analysis, Ladan Mohaddes who helped me revise my paper, Seoungyong Yang who trained and helped me on dielectric measurement.

I would like to thank Yi Qi, Wen-Hsien Chuang and Sheng Li who borrowed me equipments weekly for setting up experiments.

I would like to thank Tim Zhang who helped me on AFM maintenance and problem solving.

I would like to thank Liyang Dai for teaching me Latex and Dorothea Brosius who helps me in latex programming and revising my thesis for grammar mistakes.

I would like to thank Lesly McAnelly, Swati Tiwari and Pragya Purohit for checking the chapters of my thesis.

I would especially like to thank all the members of my committee for their efforts on my behalf: Professor Alaxander Roytburd, Professor John Melngailis, Professor Theodore L. Einstein, Professor Manfred Wuttig, Professor Ichiro Takeuchi and Professor James Cullen.

Particular and heartfelt thanks go to all my friends who made my life in a foreign country colorful and enjoyable.

I would like to thank my family for their encouragement and support during

my Ph.D studies.

I apologize in advance to those whose important contributions have been overlooked here because of my own unfamiliarity with them or my inability fully to appreciate their significance.

TABLE OF CONTENTS

LIST OF TABLES

LIST OF FIGURES

Chapter 1

General Introduction

1.1 Motivation and Objectives of Research

In recent years, ferroelectric films have become a subject of intensive research because of their potential applications not only as non-volatile random access memories or dynamic random access memories but also as active components of sensors, actuators, and microelectromechanical systems (MEMS). These applications either require a high electrical field response to an external mechanical field (direct piezoeffect) for sensors, or a high strain response to an applied electric field (converse piezoeffect) for actuators and MEMS. However, the fundamental problem that limits their use is that ferroelectric films have inferior electrical and electromechanical properties compared to their bulk counterparts. Particularly, the effect of movement of boundaries between elastic (non-180°) domains on electromechanical properties (so-called extrinsic dielectric and piezoelectric effects) is much less prominent in the films than in bulk materials.

Discussion of this effect in constrained films has a long history. Since the formation of elastic domains is a mechanism of relaxation of film/substrate het-

erostructures approaching an equilibrium[1], it is possible to shift the equilibrium by applying an electric field and obtain reversible field-induced deformation due to change of domain structure[2]. This extrinsic converse piezoeffect was analyzed quantitatively, and it was shown that the contribution to the piezomodulus normal to film/substrate interface, d_{33}, of constrained ferroelectric film is significant and comparable with intrinsic piezomodulus of a single domain bulk crystal[3]. However, experimental observations neither show visible change of domain structure under electric field or the relatively large piezoeffect expected theoretically. Piezomoduli of polydomain films do not differ much from those of single domain films. This had led to a conclusion that in contrary to their bulk counterparts the elastic domain structure in epitaxial films is immobile because the domain walls are pinned by defects inside the films or at the film/substrate interface[4][5].

It has been suggested in [6] that the effect of domain wall movement on piezodeformation can be made much more visible if the elastic clamping decreases. One way to decrease the clamping is reducing the lateral dimensions of the film to make them comparable to the film thickness. According to the St. Venant principle, the internal stress due to constraint is located in a region near the film/substrate interface with a depth approximately equal to the lateral dimension of an island. The decrease of an average biaxial stress in an island can be described as an effective increase of the compliance,S, in the equation

$$d_{33}^f = d_{33} - \frac{2S_{13}^f}{S_{11}^f + S_{12}^f} d_{31} \tag{1.1}$$

where d_{33}^f is the converse longitudinal piezoelectric coefficient of the constraint film; d_{33} and d_{31} are piezomoduli of a free-standing film. $S_{11} + S_{12} = S$ is the elastic compliance of the film. This effective compliance increases with a reduction in the ratio of the lateral size of the island l to the film thickness h and approaches infinity

when l/h goes to zero. Then d_{33}^f of the islands approaches d_{33} of a free-standing single domain film or a bulk single domain crystal. For a polydomain film, the extrinsic effect due to domain wall movement is itself a result of clamping[2][3]. With decreasing clamping effect, theoretically this piezoresponse should increase infinitely, while practically it is determined by the remaining clamping effect as well as by finite mobility of domain walls.

Focused ion beam (FIB) technique provides the possibility to fabricate micron and submicron island by patterning the epitaxial films to decrease substrate clamping[7]. This method was applied to microfabricate $1 \times 1 \times 1\mu$m islands from $PbZr_{0.2}Ti_{0.8}O_3$ film grown on (001) $SrTiO_3$. Partially released clamping gives rise to substantial increase in the effective piezoelectric coefficient up to 3 times larger than its theoretical intrinsic value[8]. Piezoelectric force microscopy of the islands has revealed extensive domain wall movement under local electric field[9].

Since modern electronic industry has relied on the development of materials and processes compatible with silicon-based integrated circuit, it is of a great importance to reproduce the similar enhancement of piezoproperty in the islands fabricated from PZT films on Si-based substrate. To achieve this objective, it was necessary to obtain high quality epitaxial films on Si-substrates, to develop the FIB technique for the fabrication of not inferior ferroelectric micron and sub-micron islands with mobile domain structure, and to explore the possibility of controlling the domain nanoscale structure. Therefore, this research has been focused on the FIB fabrication of the micron size film islands of PZT epitaxial film on Si-substrate and on the study of their domain nanostructure and piezoproperties. Our research includes the study of:

1. the piezoresponse of ferroelectric islands and its dependence on the shape of

the islands;

2. the island domain structure and its evolution under local electric field;

3. the effect of local field on the domain evolution in continuous film to estimate mobility of domain wall in film on Si-substrate;

To determine extrinsic contribution of domain wall movement to piezoresponse of patterned islands, the intrinsic response of the polydomain islands with immobile domain walls is calculated using finite element method.

Combining the focused ion beam technique for nanopatterning of the film heterostructures, the structure and domain characterization, the measurement of ferroelectric and piezoelectric properties and their modeling, we have achieved the goals of this research.

1.2 Contributions

In summary, the contributions of this thesis work include:

1. We conducted the systematic investigation of local electric field on the domain structure, and to our knowledge we are the first to observe the self-organization of 90° domain in the constraint film;

2. We are the first to employ focused ion beam techniques to pattern the PZT film epitaxially grown on Si substrate to micron size capacitor and strip structure to decrease the constraint from the substrate;

3. We are the first to demonstrate the change of domain configuration from three-domain structure to two-domain structure in a strip structure by nanopat-

terning and show the resultant maximum enhancement of piezoresponse in the strip structure;

4. We are the first to model the micron size islands with immobile three-domain structure by the finite element method and calculate the intrinsic piezoresponse of the islands. We estimated the extrinsic contribution to the piezoresponse from 90° domain wall movement of the patterned structures;

5. We detected the piezoelectric response of nanopatterned capacitor by piezoelectric force microscope. We conducted systematic investigation of the dependence of the piezoelectric response on the DC and AC electric field as well as the effect of geometry of the patterned structures;

Chapter 2

Physics Background

2.1 Piezoelectricity and Ferroelectricity

The measured thermal, electrical and mechanical properties or their combinations under equilibrium state of crystal are reflections of different crystal symmetries and structures. From the crystallography point of view, all crystals can be classified to one of 32 point groups, in which 11 have a center of symmetry (they are *centrosymmetric*). The other 21 point groups are non-symmetric, *i.e.*, they lack a symmetry center. These low symmetry structure crystals, except one (Class 432), can exhibit a property called *piezoelectricity* when acted on by the electric and/or stress field.

2.1.1 Piezoelectricity

The term piezoelectricity is derived from the Greek word *piezein*, meaning to press. It was first discovered in quartz in 1880 by J&P Curie during the studies of pressure on the generation of electrical charge by crystals[10]. The piezoelectric effect is a linear and reversible electromechanical effect where the mechanical strain (S) and

stress (T) are coupled to the electric field (E) and displacement (or charge density D) linearly, as follows:

$$D = dT$$
$$S = dE \tag{2.1}$$

The first equation describes the charge density change when a stress is applied to the crystal, this is called *direct* piezoelectric effect. Similarly, the *converse* piezoelectric effect in the second equation states that the crystal will become strained when an electric field E is applied. The variable d in the above equations is the piezoelectric coefficient. If considering the linear elastic and dielectric relations, the piezoelectric constitutive equations can be written out in the full tensor form[11]:

$$D_i = \varepsilon_{ij}^T E_j + d_{ijkl} T_{jk}$$
$$S_{ij} = d_{kij} E_k + s_{ijkl}^E T_{kl} \tag{2.2}$$

in which s is elastic compliance, a fourth-rank tensor, and the second-rank tensor ε is the dielectric constant. The subscripts i, j, k, l are values between 1 and 3. The superscript E means that the elastic compliance is measured under the constant electric field (short-circuit condition), and T means the dielectric constant is measured under the constant stress. The values measured under constant electric field and under constant stress can be very different because of the electromechanical coupling effect. By using matrix notation, the number of suffixes can be reduced as shown in Table 2.1[12]:

In general, there are 27 independent piezoelectric coefficients, 3 independent dielectric constants and 36 independent elastic compliances. Since d_{ijk} are symmetrical in j and k, s_{ijkl} are symmetrical in i and j, k and l respectively, and ε_{ij} is

Table 2.1: Matrix Notation

Tensor Notation	11	22	33	23,32	31,13	12,21
Matrix Notation	1	2	3	4	5	5

symmetrical in i and j, independent components are reduced. For a given piezoelectric material, the number of independent parameters can be further reduced using symmetry relations in the material. For example, for tetragonal structure crystal which has a point group of $4mm$, and is poled in 3-direction, there are only 3 independent piezoelectric coefficients, 2 independent dielectric constants and 6 independent elastic compliances. The matrices of these parameters are as follows:

$$\begin{pmatrix} 0 & 0 & 0 & 0 & d_{15} & 0 \\ 0 & 0 & 0 & d_{15} & 0 & 0 \\ d_{31} & d_{31} & d_{33} & 0 & 0 & 0 \end{pmatrix}, \quad \begin{pmatrix} \varepsilon_{11} & 0 & 0 \\ 0 & \varepsilon_{11} & 0 \\ 0 & 0 & \varepsilon_{33} \end{pmatrix},$$

$$\begin{pmatrix} s_{11} & s_{12} & s_{13} & 0 & 0 & 0 \\ s_{12} & s_{11} & s_{13} & 0 & 0 & 0 \\ s_{13} & s_{13} & s_{33} & 0 & 0 & 0 \\ 0 & 0 & 0 & s_{44} & 0 & 0 \\ 0 & 0 & 0 & 0 & s_{44} & 0 \\ 0 & 0 & 0 & 0 & 0 & s_{66}[= 2(s_{11} - s_{12})] \end{pmatrix} \tag{2.3}$$

As mentioned above, the piezoelectric phenomenon is forbidden by the symmetry in crystals with a symmetric center. This is because the non-symmetric crystal can be polarized, *i.e.*, electrical dipole moment can be induced, due to the deformation of the crystal upon the application of proper external stress or electric field (and only if the crystal is an electrical insulator). If the center of symmetry is present, the crystal can not be polarized, which means the center of negative charges and positive charges will always be the same. For given piezoelectric materials, the polarization generation mechanisms are closely related to the crystal structure. For example, in a barium titanate (BTO) crystal, the generation of polarization is due to relative displacement of positive central Ti ion and negative oxygen ions which form octahedral structure around Ti ions.

Generally speaking, mechanical deformation can be induced by the application of the electric field in all materials, this is called *electric field induced strain*. In insulating low symmetry materials, the linear coupling (or primary coupling) between the strain and electric field is described by the converse piezoelectric effect. More generally, a secondary coupling in which the strain is proportional to the square of the electric field is present in all materials regardless of symmetry, this is called *electrostrictive effect*. This quadric nonlinearity between the strain and electric field is valid only in the single domain crystal and the state does not change with the electric field. The relation between the electrostrictive strain χ and the induced polarization P by the electric field is expressed as

$$\chi_{ij} = Q_{ijkl} P_k P_l, \tag{2.4}$$

where Q_{ijkl} are the four-rank tensors called *electrostrictive coefficients*. The above relationship holds for all the materials regardless of linearity or nonlinearity between the electric field and induced polarization. Due to the quadric term of polarization P, the electrostrictive coefficients are always positive, while the piezoelectric coefficient can be either positive or negative depending on the direction of the applied electric or stress fields and induced strain or polarization. When the external field is a combination of DC and AC electric fields, the interaction term of P_{DC} and P_{AC}, *i.e.*, $(QP_{DC})P_{AC}$ can be viewed as a piezoelectric effect in an induced non-symmetric system that is biased by the DC electric field[13]. This induced piezoelectric effect can be very large in certain systems such as relaxor-ferroelectrics[14].

2.1.2 Ferroelectricity

A subgroup of piezoelectric crystals (10 out of 20 point groups) has a unique polar axis. Crystals belonging to this group show an electric dipole moment even in the absence of an external field. The polarization associated with the spontaneously formed electric dipole moment is called *spontaneous polarization*, which is temperature dependent. When the temperature is changed, the electric charges will change on the surface of the crystal due to the change of the spontaneous

polarization. The phenomenon is called *pyroelectricity*[15], and may be written as

$$D_i = p_i \Delta T, \tag{2.5}$$

whereby p_i is the vector of the pyroelectric coefficient. If the orientation of spontaneous formed polarization can be switched by the external electric field (lower than the breakdown limit of crystal), then the crystal is said to be *ferroelectric*, or they have *ferroelectricity*. So by definition, ferroelectricity is a pyroelectric material with two or more stable states of nonzero polarization which can be switched by the application of a sufficiently strong electric field.

Different from dielectric materials, the switchability of the spontaneous polarizations causes the hysteretic relationship between the polarization and the electric field as shown in Figure 2.1, which is characteristic of the ferroelectric materials. The finite polarization in the absence of the electric field is called *remnant polarization* (spontaneous polarization), denoted as P_r. The voltage at which polarization changes direction is called *coercive field* V_c[16].

Ferroelectric materials usually undergo structural phase transition from high temperature non-ferroelectric phase to low temperature ferroelectric phase, which is a result of lowering the total free energy of the system. The first transition (if there is more than one structure transition) temperature to a ferroelectric phase is called *Curie temperature* T_c. Close to the Curie temperature in the paraelectric state, the dielectric constant falls off with temperature according to Curie-Weiss

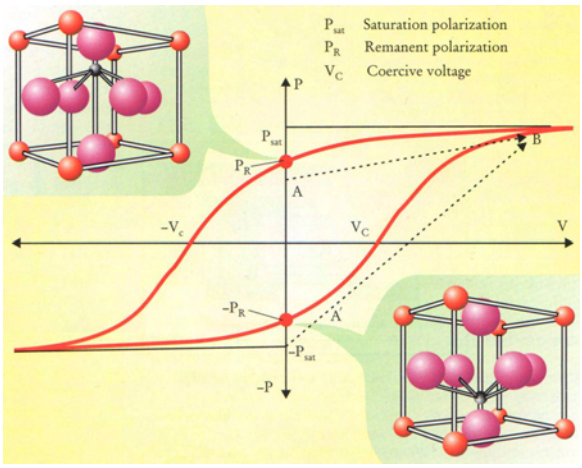

Figure 2.1: Hysteretic loop between the polarization and the electric field of ferroelectric materials, two remnant polarizations (spontaneous polarization) correspond to two lower stable states

Law as

$$\varepsilon_r = B + \frac{C}{T - T_c}, \tag{2.6}$$

where B and C are constants. At the lower temperature ferroelectric state, the two lower stable states correspond to spontaneous polarization $(+P_r, -P_r)$ as shown in Figure 2.1.

Ferroelectricity was first illustrated in Rochelle salt crystals in 1921 by J. Valasek[17]. According to Landoldt and Bornstein[18], there are about 600 ferro- and antiferroelectric materials have been discovered up to now. They can be divided into hydrogen bonded systems like KDP, ionic crystals as in perovskite crystals, and narrow gap semiconductors like GeTe. The most studied and frequently applied ferroelectric materials are those with perovskite-type structures and many are solid solutions of $PbTiO_3$. The general formula of the perovskite structure is ABO_3, which A and B are cations such as Pb^{2+}, Ti^{4+} and O is oxy-

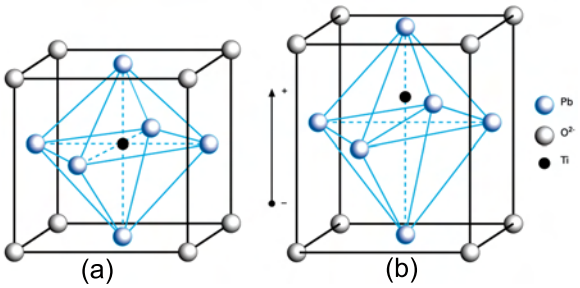

Figure 2.2: Unit cell of perovskite structure $PbTiO_3$ (a) cubic structure at paraelectric state; (b) tetragonal structure at ferroelectric state

gen anion O^{2-}. The cubic unit cell of the perovskite $PbTiO_3$ (PTO) is shown in Figure 2.2(a), in which Pb^{2+} ions sit at the corner of the cubic unit cell, O^{2+} ions are located at the face center, while Ti^{4+} ions are at the body center. The whole structure can be viewed as consisting of TiO_6 octahedron surrounded by Pb^{2+} ions. The T_c of $PbTiO_3$ is $490°C$. Above $490°C$, PTO is paraelectric with the cubic structure; lower than $490°C$, it is ferroelectric. The Ti^{4+} ion displaces toward one of its six neighboring oxygens and the crystal becomes slightly elongated to form the tetragonal structure. The spontaneous polarization occurs as a result of the relative shift of Ti^{4+} ion and O^{2-} octahedra with respect to the Pb^{2+} ion as shown in Figure 2.2(b). This shift breaks the cubic symmetry, resulting in six symmetry-equivalent variants with polarizations along the x, y, and z direction of the pseudocubic axis.

The ferroelectric phase transition in the equilibrium state can be treated phenomenologically by the Laudau-Ginzburg-Devonshire (LGD) thermodynamic theory[19][20]. The theory describes the macroscopic picture of ferroelectrics based on Gibbs free

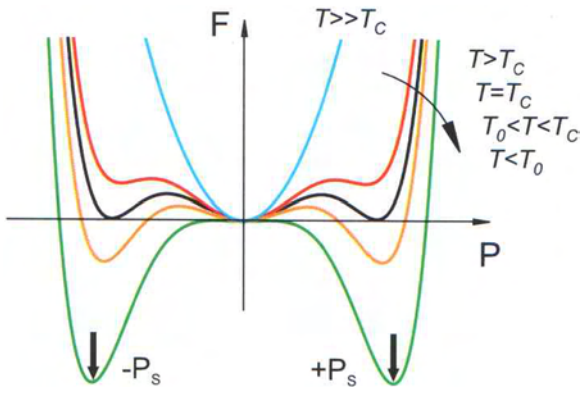

Figure 2.3: The free energy as a function of polarization for a ferroelectric with a first-order phase transition as a function of temperature.

energy, which is expressed as

$$G = G_0 + \frac{1}{2}\beta(T - T_0)P^2 + \frac{1}{4}\gamma P^4 + \frac{1}{6}\delta P^6, \tag{2.7}$$

where β, γ and δ are constants. β and δ are found to be positive in all known ferroelectrics, while γ can be either positive or negative. Figure 2.3 shows the characteristic curves of the Gibbs free energy (G) *vs.* polarization for ferroelectrics with a first-order transition in different temperature ranges. T_0, T_c, T_1, and T_2 are a series of special temperatures characterizing the transition from the ferroelectric phase to the paraelectric phase.

As mentioned above, all the ferroelectric materials are pyroelectric, while not all the piezoelectric materials possess ferroelectric properties. The relationships between piezoelectrics, pyroelectrics and ferroelectrics are illustrated in Figure 2.4.

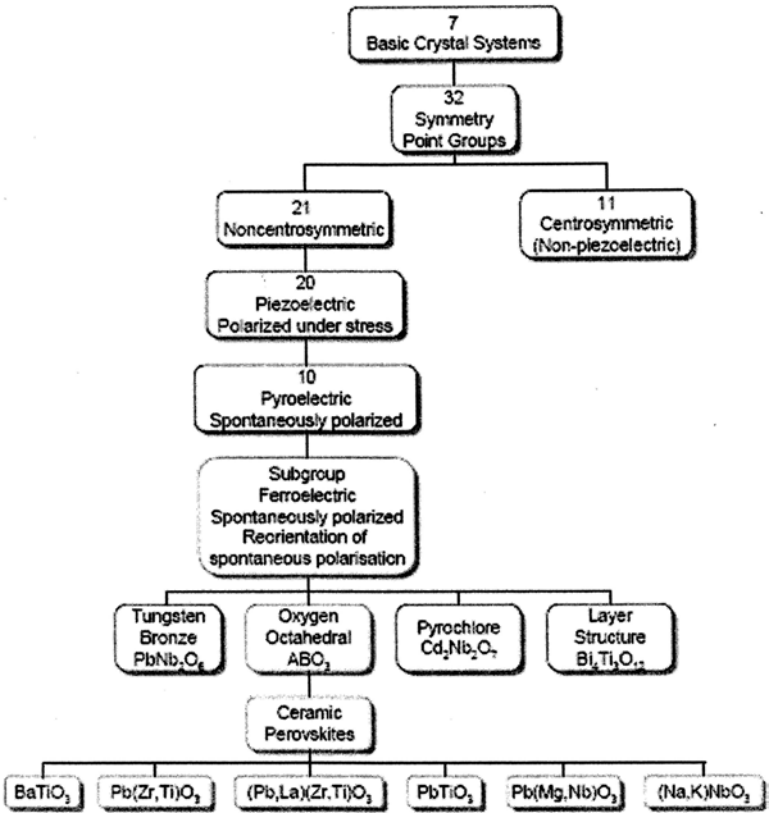

Figure 2.4: Relationship between piezoelectrics, pyroelectrics and ferroelectrics

2.1.3 Ferroelectric domains

When ferroelectric materials cool down from high temperature, the crystal is subdivided to regions with different spontaneous polarization orientations to minimize the electrostatic energy of depolarization fields and the elastic energy due to mechanical constraints. The region that has the uniform spontaneous polarization orientation is called a ferroelectric *domain*. For a fully compensated ferroelectric single crystal of a suitable orientation, a single domain state is the lowest free energy. However, in most cases, different domains will form which is driven by electrical or mechanical boundary conditions. As in the example of $PbTiO_3$, six equivalent polarizations can possibly form in the crystal depending on the stress and electric field conditions in the crystal during the cooling. The domains with out-of-plane polarization are called c domains, while the domains with in-plane polarization are called a domains. The boundary of different domains is called *domain wall*. If the angle between the spontaneous polarization orientations of the neighbor domains is 180° apart, the domain wall is called the 180° domain wall; if the angles are not 180° apart, for example, they are 90°, 71° apart as in a tetragonal structure and rhombohedral structure, these domains are called 90° or 71° domain wall, or generally, the non-180° domain wall.

In the tetragonal structure crystal, both 180° and 90° domain walls can form in the crystal; however, the formation mechanism is slightly different. The formation of both the 180° and 90° domain wall can minimize the depolarization field by

compensating for the surface charge in an unpoled ferroelectric ceramics, but only the formation of the 90° domain wall can release the elastic energy stored in the crystal. Moreover, both the 180° and non-180° domain wall motion will increase the dielectric properties, while only non-180° domain wall motion will affect the piezoelectric response. Because the lattice parameters of the unit cells at both sides of 180° domain wall are the same, the movement of the 180° domain wall will not induce piezoelectric strain. However, the different lattice parameters along the 90° domain wall will induce large piezoelectric strain[21][22]: in the tetragonal crystal, the strain induced will approach the tetragonality of the crystal and increase the piezoelectric properties as shown in [23] and illustrated in Figure 2.5 . It is worth mentioning that the movement of 180° domains wall can increase the apparent piezoelectric response when the applied electric field reached the coercive field. This is due to the fact that the amount of domains that have the same spontaneous polarization orientation with the electric field increases and these domains expand along the electric field direction, while the amount of domains with opposite polarization direction decreases and the domains shrink under the electric field. This is illustrated in [24].

The switching of polarization leads to the hysteresis relationship not only between polarization and the electric field, but also between the strain and electric field, which is in a butterfly shape as shown in Figure 2.6(a)[13]. Ideally, both the hysteresis loops are linear, caused only by the pure piezoelectric effect; while in the

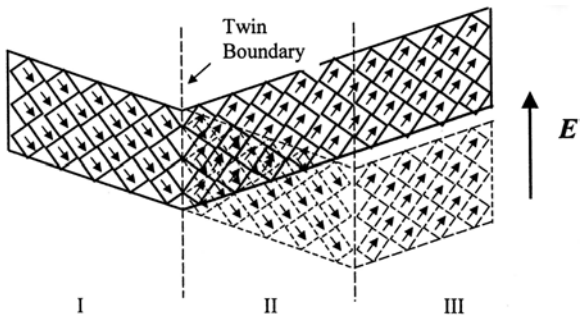

Figure 2.5: Movement of 90° domain and induced piezoelectric strain

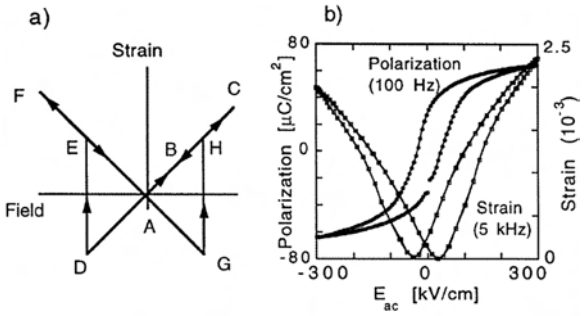

Figure 2.6: Strain vs. electric field (χ vs.E) hysteresis loop (butterfly loop) in ferroelectrics: (a) idealized loop in a crystal in which polarization reverses only by 180° and (b) actual polarization and strain loops measured on (111)-oriented, 322 nm thick, sol-gel $Pb(Zr_{0.53}Ti_{0.47})O_3$ thin film (Damjanovic,1998)

actual crystal, due to the switching and movement of the domain wall (especially non-180° domain wall movement), the actual hysteresis loop is more complicated. Figure 2.6(b) shows the typical hysteresis loop observed in the experiment.

The general ferroelectric domain structures in equilibrium is a result of minimizing the overall deformation and the electrostatic energy.

$$\mathcal{W}_{tot} = W_M + W_E + W_{DW} + W_S = min, \tag{2.8}$$

where W_M is the elastic energy, W_E is the electric energy, W_{DW} is the domain wall energy, and W_S is the surface energy. The static ferroelectric domain mi-

crostructure in single crystals, powders, and ceramics has been observed by many techniques including optical microscopy, scanning electron microscopy, transmission electron microscopy and recently atomic force microscopy. In ferroelectric ceramics, each region of the material is not free to deform due to the surrounding constraint, so complicated domain patterns form consisting of randomly orientated grains. Polycrystalline thin films, however, often exhibit preferred orientation of polar axis due to the strong interaction with the substrate and the domain reversal processes are expected to be rather complicated and limited by the mechanical constraining of film lattice to substrate. Such a constraint is most significant in epitaxial ferroelectric films; it is responsible for the unique periodic domain structure formation which will be discussed later.

2.2 Piezoelectric response in ferroelectric materials

Ferroelectric materials exhibit piezoelectricity. The direct and converse piezoelectric properties have been used as sensors and actuators, respectively, due to the high piezoelectric coefficients of many ferroelectrics. A good example of such ferroelectric materials is $Pb(Zr_{1-x}Ti_x)O_3$, or PZT, the solid solution of lead titanate ($PbTiO_3$) and lead zirconate ($PbZrO_3$), which has been intensively investigated and widely used in the past decades. Zr and Ti ions randomly occupy the center

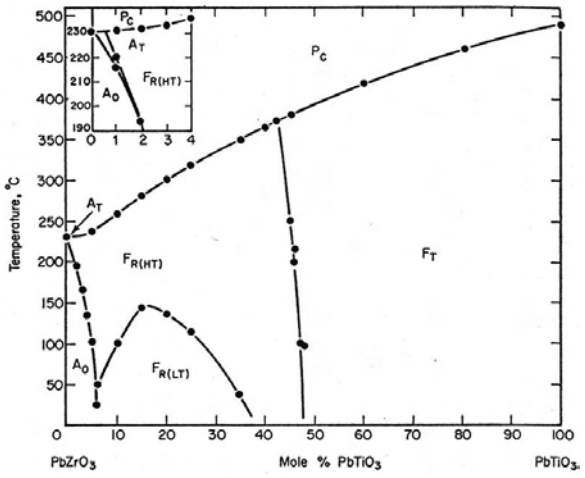

Figure 2.7: Phase diagram of $PbZrO_3 - PbTiO_3$ (PZT)

of the perovskite lattice (B site). In the formula, x is the probability of finding Ti atoms at the center of the unit cell, whereas $(1 - x)$ is the probability of finding Zr atoms that occupy the center of the unit cell. The equilibrium phase diagram of $PbZrO_3 - PbTiO_3$ solid solution is shown in Figure 2.7[10]. The line that separates the tetragonal and rhombohedral structure in the middle of the diagram is called *morphortropic phase boundary* (MPB) with Zr/Ti the ratio of 52/48 at room temperature. This composition of PZT has particularly interesting properties from the application point of view due to the fact that the maximum piezoelectric coefficient and dielectric constant appear at this composition. For ferroelectric ceramics, a process called *poling* (the application of a high external electric field to align domains in the polycrystalline materials) is necessary for the materials to exhibit a bulk piezoelectric effect.

Different from the piezoelectric materials that is non-ferroelectric, due to the

existence of spontaneous polarization in ferroelectrics, the piezoelectric coefficient of ferroelectric materials can be expressed in a way that is related to the value of spontaneous polarization. According to the LGD theory, in a mono-domain tetragonal structure ferroelectric crystal, the piezoelectric coefficient along 3-axis can be written as

$$d_{33} = 2\varepsilon_0\varepsilon_{33}Q_{11}P_s \tag{2.9}$$

in which Q_{11} is the electrostrictive coefficient, ε_0 is the dielectric constant in vacuum, ε_{33} is the dielectric constant of crystal along the 3-axis, and P_s is the spontaneous polarization. It indicates that the realization of large piezoelectric coefficients in ferroelectric materials depends on a combination of large electrostriction coefficients, large spontaneous polarization, and dielectric constant values. The piezoelectric properties of ferroelectrics can be adjusted by changing these parameters.

2.2.1 Intrinsic and extrinsic response

Generally speaking, two types of contributions to the piezoelectric effect in ferroelectric materials are distinguished, *intrinsic* contribution and *extrinsic* contribution. The intrinsic contribution originates from the piezoelectric deformation of mono-domain single crystal, as described in Equation (2.1). The extrinsic contribution comes from any other extrinsic factors that may cause additional displacement or strain under the electric field in a "real"crystal such as polycrystalline

or thin film materials. It is mainly due to the ferroelectric-ferroelastic (non-180°) domain wall motion; also it can comes from field-induced phase transitions, the grain boundary effect, and/or the effect of defects. The extrinsic contribution of 90° domain movement to the total piezoresponse has been extensively studied since the 1950's[25][17][26]. The extrinsic contributions account for 60-70% of the piezoelectric and dielectric properties in BTO and PZT[27][28][29]. This is very important to practical applications as actuators and capacitors.

Based on the phenomenological LGD theory, the intrinsic piezoelectric response of PZT can be deduced not only for single crystal but also for polycrystalline materials. This property depends on the crystal orientation. The piezoelectric strain along the normal direction $n = n_i n_j$ can be expressed in pseudo cubic coordinates as

$$\chi_{ij,n} = d_{kij} n_i n_j l_k E \tag{2.10}$$

in which $\chi_{ij,n}$ is the normal strain along the normal direction n, d_{kij} is the piezoelectric coefficient, while the electric field $E_k = l_k E$, in which l_k is the direction cosine. If the electric field is applied along the normal direction n, then the piezoelectric coefficient can be simplified to

$$d_{nn} = d_{kij} n_k n_i n_j E, \tag{2.11}$$

Figure 2.8[30] shows the orientation dependence of the intrinsic piezoelectric response of PZT bulk materials; for the tetragonal structure, the maximum value of

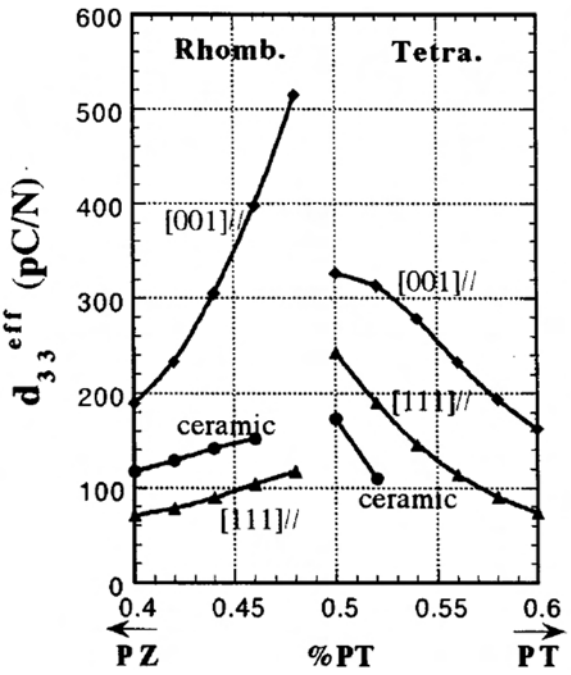

Figure 2.8: Orientation dependence of effective piezoelectric coefficients of PZT

longitudinal piezoelectric constant d_{33} is obtained along the polarization direction [001], while for the rhombohedral structure, the maximum value is 56.7° away from the polarization direction [111], close to the pseudo cubic [001] direction.

The movement of the non-180° domain under applied electric field can significantly contribute to the extrinsic piezoelectric response of ferroelectric materials. The domain wall can be pinned by defects [31] and grain boundaries of the crystal and depinned under certain electric field. The contribution from the irreversible displacement of the domain walls leads to a nonlinear and hysteretic piezoelectric response, even at relatively low driving electric fields or pressures. In order to determine the extrinsic piezoelectric effect, detailed information about the domain wall structure, distribution and nature of defects and grain boundaries needs to be

known. However, the complexity of polycrystalline ferrolectric materials makes it very difficult to calculate the extrinsic piezoelectric effect. In the following, a brief review will be given to the previous work on the 90° domain wall movement in the tetragonal structure ferroelectrics and its extrinsic contribution to the piezoelectric response.

2.2.2 Non-180° domain movement in ferroelectric materials

Bulk ferroelectric materials

It is widely accepted that the domain wall motion is a major source of piezoelectric nonlinearity and strain hysteresis in bulk ferroelectric materials. Special distribution, relative volume fraction, and dynamic motion of these domains controls the properties of the ferroelectric devices including the field-induced change in strain for the piezoelectric devices and birefringence for the electro-optic devices. Therefore, the study of non-180° domain and domain wall behavior under electrical and stress fields is of great importance to the design and optimum functional ferroelectric devices.

Among the many factors that affect the domain wall motion, the width of the domain wall and domain wall energy are most important. Domain wall width plays an important role in the mobility of the non-180° wall. Thicker walls are difficult to move, while thinner walls tend to move relatively easy. However, how wide the domain walls are and whether they are mobile or not are still controversial

in literature. Some earlier researchers claim the 90° domain walls are much more wider (hundreds of Å) than the 180° domain walls and are immobile. For example, Bursill *et al.* [32] estimated the 180° domain wall in $BaTiO_3$ to be 5-20 Å, while the 90° domain wall is much broader with a thickness of 50-100 Å. Observations of the domain wall has been done by HRTEM by different researchers. Tsai *et al.*[33] observed in $BaTiO_3$ and $Pb(Zr_{0.52}Ti_{0.48})O_3$ a diffuse dark contrast about 4-10 unit cells wide due to lattice distortion and ionic displacements. Stemmer *et al.*[34] measured the width of the 90° domain wall in PTO to be 1063 Å, and domain wall energy is estimated to be 50 mJ/m^2. Foeth[35] *et al.* confirmed the width of 1563 Å at room temperature. In contrast, recent researches show that 90° domain walls are extremely narrow, comparable to that of 180° domain wall. Floquet *et al.* [36][37] combined the study of HRTEM images and x-ray diffraction of $BaTiO_3$, concluded the width of the 90° domain wall to be 40-60 Å where the crystallographic discontinuity is accommodated by irregular atomic displacements. For micron-sized grains, they propose a wall thickness of only 1.0 ± 0.3nm for PTO.

Similar to the domain wall width, reports on domain wall energy are diverse. Padilla[38], Zhong[39], and Vendabilt[40], who investigated tetragonal BTO using an effective Hamiltonian derived from first-principle calculations, shows the 180° domain wall energy to be 16 mJ/m^2. Poykko and Chadi[41], on the other hand, found a much higher domain wall energy for BTO. First principle calculations by Meyer and Vanderbilt[40] showed that the 180° domain wall energy is 132

mJ/m^2, and the 90° domain wall has a much lower domain wall energy of 35 mJ/m^2, combined with the calculated 90° domain wall width of around one lattice parameter, $\sim$ 5Å, their work supports the idea that 90° domain walls are very narrow and easier to form than 180° domain wall. The barrier for the movement of these domain walls are very low; they should be move easily. They also explained why the domains appear to be wider than actual at room temperature, which is due to the thermal fluctuation.

To describe the extrinsic contributions to the piezoelectric properties from the 90° domain motion, several models have been set up. Basically, the 90° domains are viewed as pinned by the randomly distributed defects; the potential energy of domain walls are irregular as shown in Figure 2.9[42]. Either *reversible* movement (vibration near the equilibrium position at the minimum point of potential wall) or *irreversible* movement (depinned from the defect and across the potential barrier) of the 90° domain wall will contribute to the piezoelectric response of the ferroelectric materials. Arlt *et al.*[43],[44] expressed phenomenologically the relationship between domain wall displacement and the combination of electric and elastic energy, and calculated the contribution of the reversible 90° domain motion to the dielectric and piezoelectric effect. The field and frequency dependence of piezoelectric response, which is closely related to irreversible 90° domain movement, can be described by the Raleigh law at low to moderate driving field[45],[46].

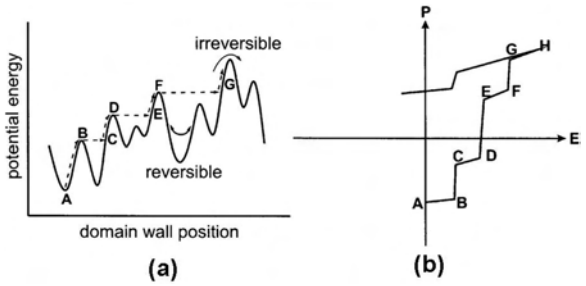

Figure 2.9: Motion of a 90° domain wall in the potential (a) and correlated hysteresis loop (b)(Waser, 2003)

In addition, several methods can be applied to differentiate the intrinsic contribution and extrinsic contribution from the 90° domain wall motion. For example, the domain wall does not contribute to the total dielectric constant at high frequencies in the GHz range, where dielectric relaxation can be observed due to the 90° domain motion; moreover, from the temperature dependence measurement of piezoelectric and dielectric properties, the intrinsic contribution can be distinguished around 0 K where all the 90° domain wall motion is frozen[27],[47].

Ferroelectric films and size effect

In the past 20 years, research on ferroelectrics has shifted from bulk ferroelectric materials (ceramics, single crystal) to ferroelectric thin films. Major driving forces for ferroelectric applications are initially non-volatile memories [48] and high-K dielectics. Now much research is being done in the area of microelectromechanical systems (MEMS) [49]. In order to introduce ferroelectrics to microelectronic industry, the properties of ferroelectrics at a small scale must be competitive with the existing technologies such as DRAM, EEPROM and flash memory. Current

memory densities in DRAM have reached the 1-Gbit level, the dimension of capacitor is about 0.13 μm, and the dielectric thickness is in the range of 5-30 nm . At this low dimension scale, it is expected that the properties of ferroelectric materials will be altered along with the vertical and/or lateral reducing of the materials. For example, if we compare ferroelectric films to bulk ferroelectric materials, bulk ferroelectric materials are usually good insulators; however, as the thickness of the film decreases, the film behaves similar to semiconductors with large bandgap. In addition, the high field required to switch the polarization state in bulk materials can be realized at low voltages for thin film, which is suitable for the integrated electronics applications.

The most important difference between three-dimensional bulk materials and two-dimensional thin film, however, is that due to the clamping of the film by a substrate, the measured properties of thin-films reflect the response from the whole system (film, interface, electrodes and substrate) rather than the film itself. The strain in the film plays an important role in tailoring the property of the film which can be considerably different from the bulk materials. In an epitaxial film in which the film is grown on a substrate of similar crystal structure but with different lattice parameters, such as tetragonal film on cubic substrate, the thinner film is stressed to fit the substrate. When the thickness is beyond certain a critical point, the domain patterns will form to release the elastic energy in the film. The ferroelectric film under tensile stress typically has dominant in-plane

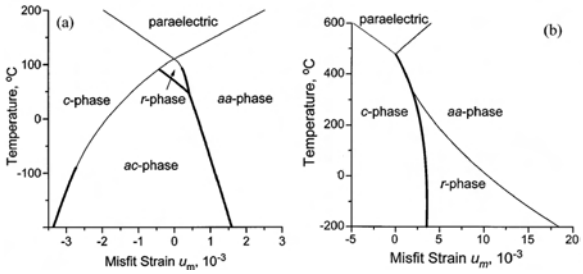

Figure 2.10: Phase diagrams of (001) single-domain (a) $BaTiO_3$ and (b) $PbTiO_3$ thin films epitaxially grown on different cubic substrates providing various misfit strains u_m in the heterostructures (Pertsev, 2003)

polarization; while predominantly out-of plane polarization appears in the film under compressive stress. Many PZT films grown on Si substrate are under certain in-plane tensile stress due to the thermal expansion coefficients mismatch between the film and substrate during cooling from the Curie temperature. The misfit strain between the film and substrate affect not only the domain configuration, but also the thermodynamic stability of the ferroelectric phases. Pertsev *et al.*[50] derived the phase diagram of BTO and PTO in the form of film as a function of misfit strain, which is shown in Figure 2.10. It can be seen that the order of phase transition changes from first to second, and the rhombohedral phase is stabilized to a very high temperature.

From a microstructure point of view, both bulk ceramic and thin film consists of grains with different polarization in the polycrystalline form. The change of grain size and domain configuration inside will be reflected in the change of properties; this is called *size effect*. In large grains, the formation of domain pattern effectively reduces the misfit energy. While in the fine grain ceramic, the domains can not

form properly so the misfit energy can be considerably large. For example, when the grain size is in the range of 0.2-10 μm, the non-180° domain size drops with the square root of the domain size[51]. In small grains under 0.2 μm, there are only simple twin bands. Thus poling efficiency which requires the coordination of neighboring grains will be decreased and the residual stresses in grain will be increased, which in turn affects the piezoelectric and ferroelectric properties. In thin films, the grain size is fine and can be comparable to film thickness, and the clamping from the substrate exists even in thick films.

The intrinsic and extrinsic contribution from the non-180° domain motion both change with size. For intrinsic contributions, the ferroelectric transformation shifts to low temperature for smaller grain size, and the temperature dependence of peak value parameters (such as dielectric constant)will be decreased and broadened [51]. For extrinsic contributions, both domain population and domain wall mobility need to be taken into account. They are all affected by the ferroelectric phase size or grain size. Experiments show that over half of piezoelectric responses are from domain wall motion in some large grained PZT ceramics, while for fine grain ceramics, the contribution from domain wall motion is limited. In thinner polycrystalline PZT film ($< 1\mu m$ thick), little contribution from non-180°domain wall movement is observed even under a moderate external stress field ($\sim$100 MPa)[52],[53]. The relaxation behavior at high frequency dielectric measurement is also not observed indicating that the non-180° domain wall movement is strongly suppressed in the

film. The small grain size, the high stress level, and/or a high concentration of mobile defect dipoles such as $V''_{Pb} - V^{\cdot\cdot}_{O}$ leads to lower non-180° domain wall mobility by stabilizing the domain structure.

In thin films, the piezoelectric properties are generally much lower than the properties of bulk ceramics. In addition to the reduction of the extrinsic contribution, clamping of the film by the substrate also plays an important role. The piezoelectric coefficient measured in the film is actually an *effective* piezoelectric coefficient due to the in-plane constraint[54]. In PZT films, this clamping effect is significant due to the larger in-plane constraint ($d_{33} \sim -2d_{31}$). If the in-plane constraint is reduced, as in Ca-doped PTO films with lower d_{31} values, the film will have d_{33} that is very close to those of the bulk materials[52]. On the other hand, the clamping effect also has some effect on the non-180° domain wall motion. For example, piezoelectric properties of a 12 μm thick PZT film are still lower than bulk material values due to the clamping by the substrate[55]. Therefore, the reduction of the clamping effect will help on improving the piezoelectric properties of the film by increasing both the intrinsic and extrinsic response of the film, especially in epitaxial film where defects in the film are less than in polycrystalline film and the clamping effect plays a more important role. This has been demonstrated in epitaxial PZT20/80 film grown on STO substrate and patterned by a focused ion beam, where the piezoelectric response is shown to be drastically increased in the discrete island. In this work, we will use Si substrate instead to show the re-

duction of the clamping effect on the piezoelectric response increase and the effect of different substrates.

2.3 Applications of ferroelectric materials

The birth of ferroelectric materials as a useful class of materials came from the understanding of both ferroelectricity and piezoelectricity through three critical discoveries[56]. First, the discovery of an unusually high dielectric constant in barium titanate; second, the discovery that the origin of the high dielectric constant was due to the permanent internal dipole moment-ferroelectricity; third, the discovery that by electric poling, single crystal-like properties can be obtained in the ceramics.

The ferroelectric materials now are widely used for a variety of applications. In bulk form, its high permittivity over a wide temperature and frequency range can be used as dielectrics in capacitors, its high piezoelectric coefficient is widely used as transducers, and its pyroelectricity have potential application in infrared imaging system. In thin film form, they are candidates for integration in the microelectronics industry. The large dielectric constants in the paraelectric state are attractive for transient charge storage as in capacitors in dynamic random access memories (DRAM)[57]. In the ferroelectric state, the reversible spontaneous polarization is very promising for non-volatile ferroelectric memories (NVFRAM)[58]; especially, $PbTiO_3$-rich compositions are very suitable for ferroelectric memory

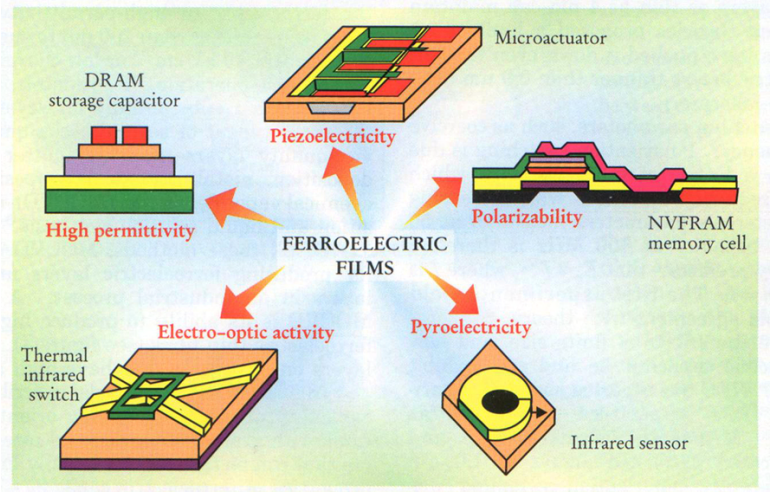

Figure 2.11: Typical applications for ferroelectric film

applications due to the large spontaneous polarization available and more squarer of tetragonal composition comparing to rhombohedral composition. In the micro-electromechanical systems (MEMS) area, many efforts have been made to make use of the piezoelectric properties of the film, mainly thick PZT film, which has been reviewed by Muralt[49][59][60]. Also, relaxor ferroelectrics such as PMN-PT are of great interest for many applications because of its giant piezoelectric constants (>2500 pm/V) that can be achieved along pseudo-cubic [001] direction[14]. Typical applications for ferroelectric film are shown in Figure 2.11.

Chapter 3

Domain Structure in Epitaxial Ferroelectric Film on Si-Substrate and Its Changes Under Local Electric Field

In this chapter, we describe how we grew high quality $PbZr_{0.2}Ti_{0.8}O_3$ ferroelectric film epitaxially on Si substrate by pulsed laser deposition, investigated the domain structure in the continuous film and studied the domain evolution under the local electric field by the piezoelectric imaging technique.

3.1 Sample preparation

All the ferroelectric PZT samples used in this study were prepared by pulsed laser deposition, which will be introduced first.

3.1.1 Pulsed laser deposition technique

Ferroelectric films can be prepared using several different methods[61], including sputtering [62][63][64][65], sol-gel[66][67], MOCVD [68][69][70], and pulsed laser deposition [71][72][73]. Pulsed laser deposition (PLD) as a film growth technique was used successfully to grow high-temperature T_C superconducting YBCO films in 1987[74], and has since attracted widespread interest. During the past decade, pulsed laser deposition has been employed in fabricating thin films of epitaxial quality. It remains an important research tool for growing high quality multi-component oxide ceramic thin films, such as ferroelectric films, high temperature superconductor films, ferromagnetic multi-layers, and colossal magneto-resistive (CMR) films. PLD has even been reported as an effective technique in the synthesis of nanotubes, nanopowders, and quantum dots.

Figure 3.1 shows a schematic diagram of a typical PLD system. During operation, a short pulsed laser beam from a KrF excimer laser is focused onto a target inside a vacuum chamber. The high pulse energy density ($\sim$1 J/pulse) leads to rapid evaporation of the target materials due to the high resulting energy density ($\sim$3-5 J/cm^2) at the target surface. The evaporated materials include both highly

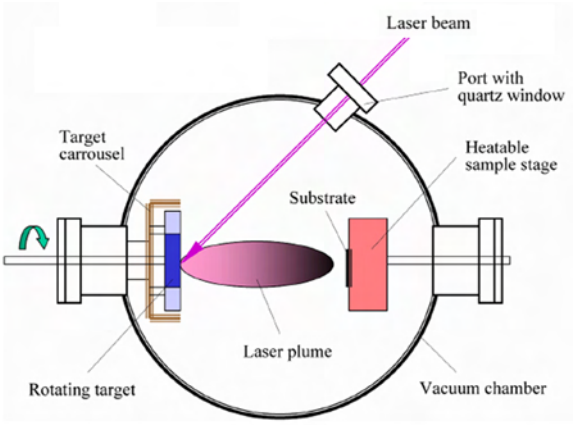

Figure 3.1: The schematic diagram of a pulsed laser deposition system

excited and ionized species. They present themselves as a glowing plasma plume immediately in front of the target surface. The target, which can be any bulk material of interest, is placed in a target holder and rotated continuously during deposition. The substrate is mounted onto the substrate holder, and is placed parallel to the target, about 10 cm away; the close proximity helps in obtaining the maximum film uniformity. The substrate is heated, by an oxidation-resistant heater, to the required elevated temperature during deposition.

PLD deposition offers many advantages when compared with other film deposition techniques. The most important feature of PLD is that the stoichiometry of the target can be retained in the deposited films. This is the result of the extremely high heating rate of the target surface (108 K/s) when subjected to pulsed laser irradiation. As such, polycomponent materials can be deposited onto substrates to form remarkably stoichiometric thin films. In addition, since the target size is smaller than in conventional PVD techniques, multiple targets can be loaded to-

gether in the chamber, allowing formation of multi-layered, multiple composition films. Another attractive feature of PLD is that the growth rate of a film can range anywhere from one atomic monolayer per second to 10 μm/s simply by varying the repetition rate; hence, both ultrathin films and thick films can be grown by this method.

A major drawback to the PLD method is the splashing of particulates onto the films due to subsurface boiling. Such particulates, up to a micron in size, will greatly affect both the growth of the subsequent layers as well as the overall electrical properties of the films. Inserting a shadow mask is one effective way to block the large particulates. Another problem with PLD is the narrow angular distribution of the ablated species, which limits the large-area uniformity of thin films. Rotating both the target and substrate can help to mitigate this problem.

In order to grow films of high quality, the following parameters of deposition need to be controlled and optimized for a specific film's growth. First, the lattice constants and the thermal expansion coefficients of the substrate and a desired film have to be matched, in order to minimize decrease the stress and avoid crack formation in the film. Moreover, the laser energy density and pulse repetition rate have to be controlled to minimize the possibility of creating the micron-sized particulates mentioned above. Because oxygen is easily lost during the deposition process, one must also ascertain the oxygen partial pressure (working pressure) which corresponds to the desired fraction of oxygen incorporated in the resulting

film. The deposition temperature, or temperature at the substrate, is very important when growing high quality films (from a crystallization point of view), since a suitably high temperature tends to assist in the nucleation of deposited elements at their correct positions/sites.

3.1.2 Sample preparation

In our study, all the PZT films were grown in a PLD system using a KrF laser with a wavelength of 248 nm and pulse width of 30 ns[75]. The nominal Zr/Ti ratio of the target was 20/80 for $PbZr_{0.2}Ti_{0.8}O_3$(PZT20/80) film growth. A (001) oriented Si single crystal wafer, with lattice constant a = 5.4308 Å, was selected as the substrate material, particularly since Si would be compatible in the application of integrating a functional oxide film within the microelectronics industry. PZT film cannot be grown directly on a Si substrate due to the large mismatch strain between the film and the substrate; however, in this work, a ferroelectric $Pb(Zr_{0.2}Ti_{0.8})O_3$ epitaxial film was successfully grown on Si substrate using $SrTiO_3$ template layer with a perovskite structure[76]. The thickness of the pre-deposited $SrTiO_3$ (001) template layer was 200 Å, grown by molecular beam epitaxy. Prior to the PZT film deposition, the 80 nm thick epitaxial $La(Sr_{0.5}Co_{0.5})O_3$ (LSCO) bottom electrode was in situ deposited onto the substrate by pulsed laser deposition at 600°C, in an oxygen pressure of 100 mTorr. During the PZT film deposition, the substrate temperature was maintained at 650°C with an oxygen pressure of 400 mTorr. The

repetition rate of the laser was 4 Hz, and the beam energy was 400 mJ/cm^2. After growth, the sample was cooled in an oxygen pressure of 300 Torr. The cooling rate was kept low (3°C/min) to avoid cracking. LSCO and Pt top electrodes, about 50 nm thick each, were also deposited by PLD to form capacitors for piezoelectric and polarization measurement.

Figure 3.2 is a cross section of a 1 micron thick $PbZr_{0.2}Ti_{0.8}O_3/SrTiO_3/Si$ film heterostructure. Two thicknesses, 1μm and 0.5μm, were prepared for the study. It is known that the film is in a paraelectric state at the growth temperature (650°C), with a cubic structure. Then during subsequent cooling, the film undergoes a cubic-tetragonal transformation at 420°C (Curie temperature T_c), and becomes tetragonal at room temperature. The film composition obtained by this work is the same as the target as confirmed by energy dispersive spectroscopy. To apply the local electric field, a conductive PFM tip was scanned on the naked surface of the film. A weak AC electric field, combined with a DC bias, was applied between the tip and bottom electrode. Since there was no top electrode on the film surface, the PFM tip served as a movable electrode. Prior to measuring the ferroelectric and piezoelectric properties, Pt was deposited by pulsed laser deposition onto the film surface, which had been patterned using standard lithography. The resulting capacitor size was 52 microns in diameter. For each film, five capacitors were tested, and the results were averaged. Measurements were made at the center of each capacitor to avoid the edge effect.

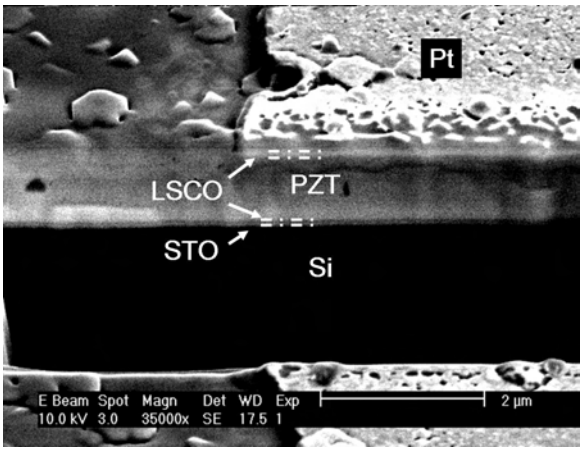

Figure 3.2: Cross section of a $1\mu m$ thick PZT20/80 film grown on Si substrate

3.2 90° domains in ferroelectric films on Si substrate

3.2.1 Domain visualization and manipulation by PFM

Various scanning probe microscopies (SPM) have been developed and have become power tools for studying ferroelectric materials. These techniques include electrostatic force microscopy, piezoelectric force microscopy, scanning capacitance microscopy and scanning non-linear dielectric microscopy[77]. Of the many different ferroelectric imaging techniques, Piezoelectric Force Microscopy (PFM) has rapidly become one of the primary tools for ferroelectric thin film research. PFM can be used for static domain structure imaging, with a resolution up to 10 nm. In addition, by locally poling the different regions, the dynamic domain evolution under external thermal, stress and electric field can be detected [78][79], and

electromechanical properties can be quantified by local hysteresis measurement. Moreover, the domain size and density can be manipulated precisely by varying the electric field[80][81]. In this chapter, we will focus on the domain imaging technique. In next chapter, piezoelectric coefficient measurement by PFM will be employed.

Piezoelectric force microscopy is a voltage modulated scanning probe microscopy, and is based on the detection of bias-induced surface deformation[82]. It can be used to image the ferroelectric film surface[83], and to measure the local piezoresponse of the film[84] by a lock-in technique. In image mode, an AC biased conducting AFM tip scans the naked surface of a ferroelectric film. In contact mode, local piezoelectric amplitude, phase information and topography can be recorded simultaneously. The contrast of the piezo-image shows the contours of the domain pattern, each representing a different polarization direction. This is realized by a technique called Phase-Sensitive Detection (PSD), performed by a four-quadrant (A,B,C,D) laser photo detector (phase sensitive detector, shown in Figure 3.3), which is the heart of the lock-in amplifier. For c domains, the polarization vector is aligned either 0° to the electric field ("in phase") or 180° from the electric field ("out of phase"). The tip vertical displacement can be written as:

$$\Delta z = \int_0^{t_f} d_{33}^{thin\ film} E(z,t) dz \tag{3.1}$$

where $E(z,t)$ is the electric field as a function of time t and displacement z. t_f is the thickness of the ferroelectric layer. The displacement can be detected by tracking

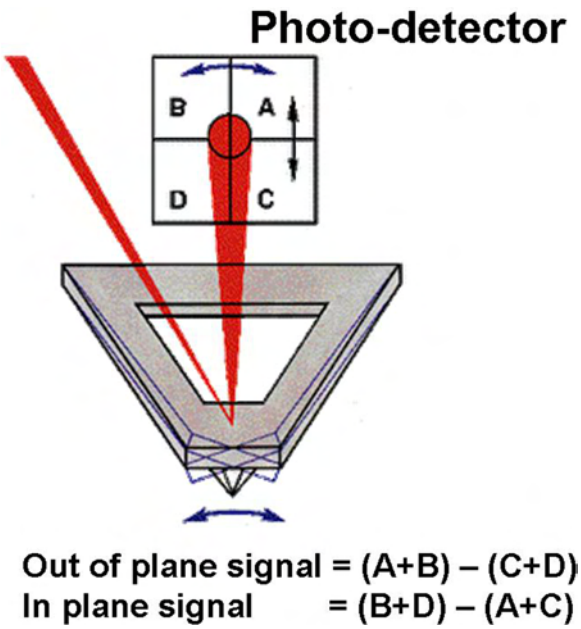

Figure 3.3: Phase-Sensitive Detection (PSD) technique

the signal difference between upper and lower detectors (A+B) and (C+D); for a domains, the polarization aligns in the surface, and the shear effect of d_{15} generates a torque on the cantilever which can be approximated as:

$$\Delta\theta = \frac{1}{\sqrt{2t_F}} \int_0^{t_F} d_{15} E_{AC}(Z) dz \tag{3.2}$$

This lateral displacement can be detected by the signal difference between left and right detectors (B+D) and (A+C). The above signals are sent to two different lock-in amplifiers and compared to the reference signal which is fed to the tip. Both the amplitude, which is proportional to the piezoelectric coefficient, and the phase, which is the angle difference φ between the piezoresponse and electric field, are detected and separated. The "in phase"domain ($\varphi = 0°$) shows black contrast and the "out of phase"domain ($\varphi = 180°$) shows white contrast. From the typical

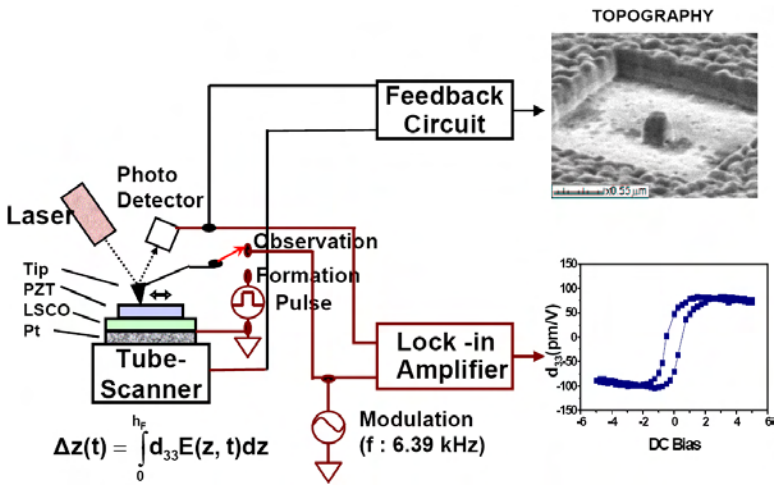

Figure 3.4: Piezoelectric force microscope setup for ferroelectric domain imaging and piezoelectic coefficient measurement

PFM image shown in Figure 3.5(a) one can clearly differentiate neighboring 180° domains due to the contrast mechanism. The PFM setup used for domain imaging in our study is schematically shown in Figure 3.4.

Despite the wide application of PFM as a domain imaging tool, there is still some controversy regarding the contrast formation mechanism. The experimentally measured piezoresponse amplitude can be expressed as:

$$A = A_{el} + A_{piezo} + A_{nl} \tag{3.3}$$

In addition to the electromechanical response A_{piezo} from the sample surface, the PFM signal also includes contributions from long range electrostatic forces A_{el} as well as non-local contributions A_{nl} due to capacitive cantilever-surface interactions. According to the Contrast Mechanism Map developed by Kalinin *et al.*[85], regions with strong indentation are the areas where piezoelectric response is dominant. These regions depend on the contact radius and the indentation force. In addition,

non-local interactions by the cantilever can be minimized by using stiff cantilevers with spring constants k_{eff} >1 N/m. In our work, the conductive PFM tip is a Ti/Pt coated Si tip with an apex radius of 20nm and a spring constant of 5 N/m, the resonant frequency is 75 KHz, and the contact force is estimated to be 70∼100 nN.

3.2.2 Observation of 90° domain motion in the film

$1\mu m$ thick film

The out of plane signal PFM and SEM images of the 1 micron thick film are shown in Figure 3.5(a) and (b).The film is observed to consist of three domain variants: $c, a1$ and $a2$, respectively. For the (001) oriented tetragonal film, the three-domain variant pattern is energy favorable due to the symmetric biaxial in-plane stress. Three variants form a cellular grid-like pattern on the film surface, in accordance with the theoretical prediction[1][86] and the experimental observation of PZT 20/80 films with thicknesses larger than 300 nm[87]. This structure is called the $c/a1/c/a2$ domain structure. Two polarization directions are associated with each of these variants. In Figure 3.5 (a) and (b), the needle like domains are the a domains. $a1$ and $a2$ are two sets of a domains which are orthogonal and interlocked to each other. Because a domains have in-plane polarizations, the contrast of the a domains are gray in the out-of-plane signal PFM image. The polarizations of c domains point preferentially towards the bottom electrode, and nonzero

remnant polarization exists without the presence of an electric field (poling). This has been observed in epitaxial PZT films grown on (001) single crystalline $SrTiO_3$ substrate with $La_{0.5}Sr_{0.5}CoO_3$ electrode[88]. This self-polarized polarization can be explained by the internal electric field induced by a nonsymmetric electrode[89]. X-ray diffraction (D500, Brucker-AXS) was also performed for the above film (Figure 3.5(c)). The films were shown to consist of only c domains and a domains, and no other phases (such as pyrochlore phase) exist. Figure 3.5(e) shows the ϕ- scan of the (101) peaks, indicating the epitaxial nature of the film. The domain fraction of the film was determined by rocking curves. Rocking curves of $c(002)$ and $a(200)$ are consulted to quantitatively determine the relative amounts of these domains in the films, as shown in Figure 3.5(d). There are about $55-60\%$ a domains in the film, in agreement with the PFM images. The observed small FWHM widths indicate that the film has good crystallinity. The (001) lattice parameter of the film is 4.097Å, close to the calculated bulk value of 4.135Å, indicating that the film is close to a fully relaxed state due to the formation of polydomain structure.

Cross-section transmission electron microscopy (TEM) was performed for the film grown on Si. It clearly shows a mixture of c as well as one set of a domains in the film (Figure 3.6). It can also be seen that the a domain tilts about 45° away from the substrate, and the thickness of the a domains is about 40 nm. The other set of a domains, which is orthogonal to the first a domain and parallel to the sample length, is missing in the TEM picture. The missing set of a domain, had

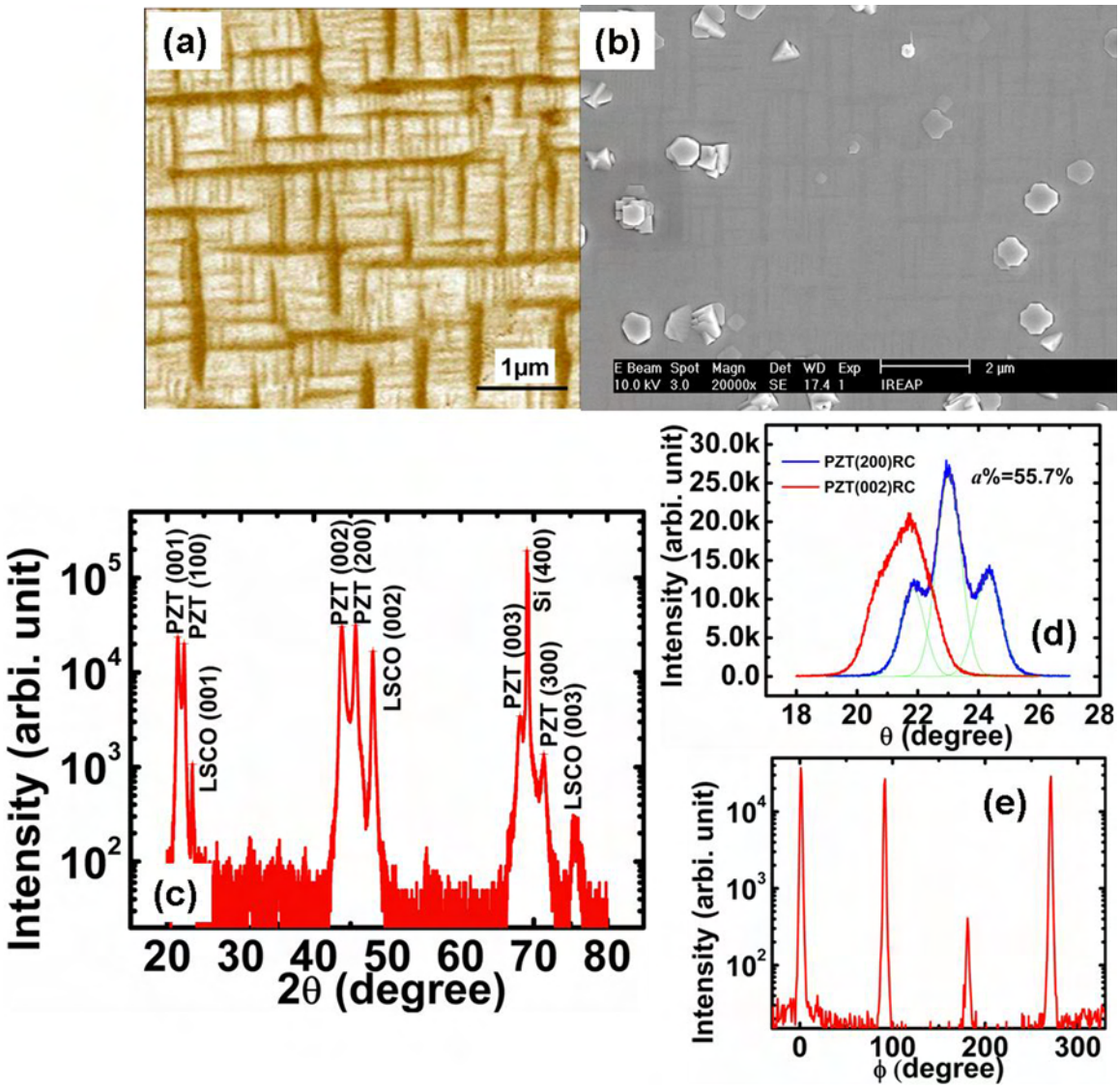

Figure 3.5: Characterization of $1\mu m$ thick PZT20/80 on Si substrate.(a) out-of-plane PFM image;(b) SEM image of the film surface; (c) X-ray diffraction of the film; (d) rocking curve of PZT (200) and PZT (002) peak; (e) φ-scan of the film

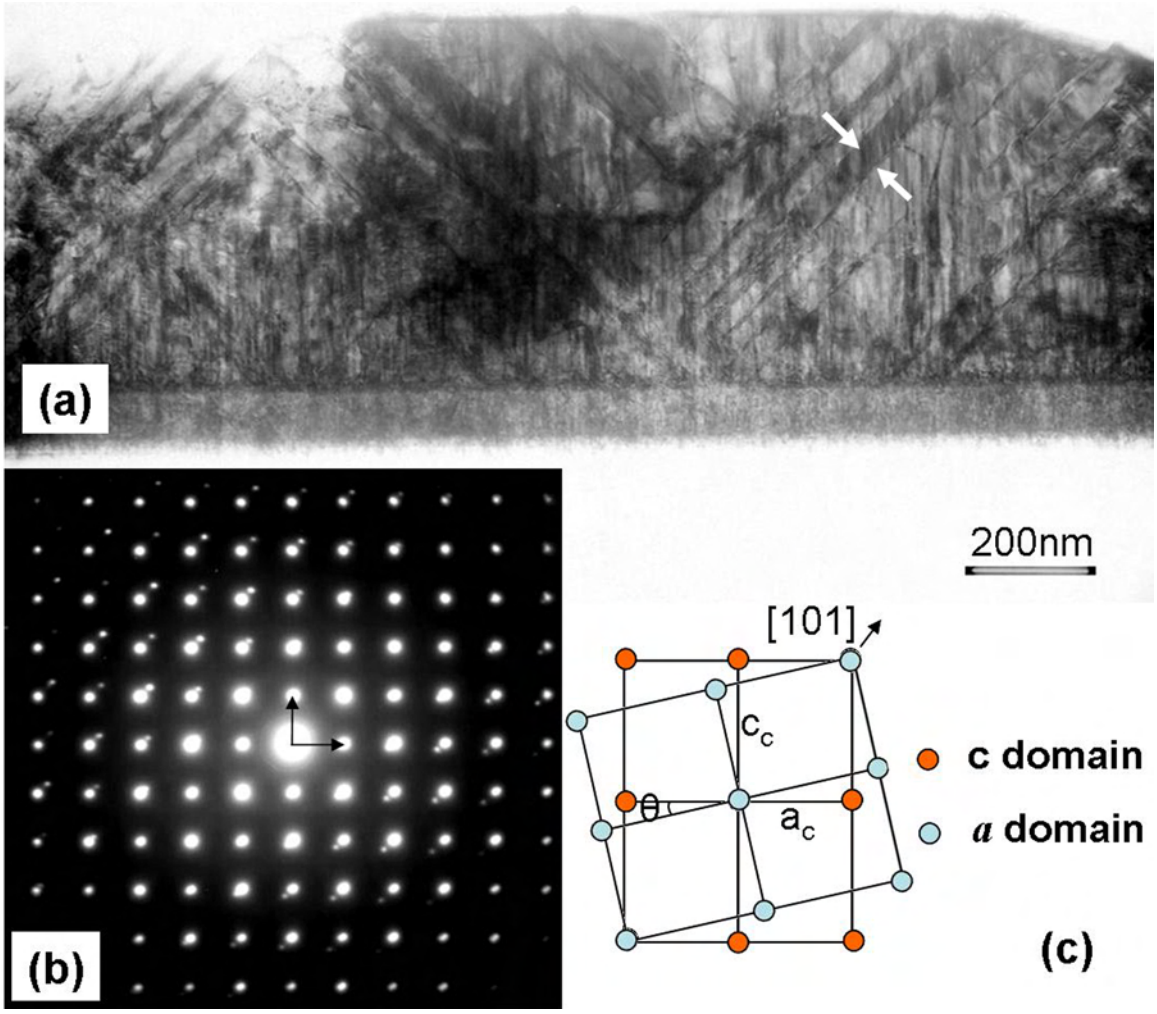

Figure 3.6: TEM analysis of 1 micron thick PZT20/80 film epitaxially grown on Si substrate. (a) bright field image;(b) diffraction pattern; (c) illustration of the diffraction pattern of polytwin

they appeared in the picture, would be observed as short bars parallel to the film surface, yet it is observed neither in the above TEM picture, nor in the accompanying diffraction pattern. This phenomenon will be discussed further later. The c and a domains are twins, they are tilted toward different sides of the shared(101) plane. The theoretical tilt angle θ between the c and a domain can be calculated from the following equation:

$$\theta = 2\tan^{-1}(\frac{c}{a}) - \frac{\pi}{2} \tag{3.4}$$

The calculated tilt angle is 2.9° for bulk $Pb(Zr_{0.2}Ti_{0.8})O_3$. The measured and calculated tilt angle from the diffraction pattern is 2.8° $\sim$ 2.9°, which is in good agreement with the theoretical tilt angle of bulk materials. The lattice tetragonality in the film calculated from reciprocal mapping (Phillips MPD system) measurements is 1.042, which is close to the theoretical tetragonality value (1.045) of bulk PZT. The observations indicate that the stress that could arise due to the lattice mismatch and thermal mismatch between the PZT film and Si substrate is almost released because of 90° domain formation.

Taking a close look at the a domains in the PZT20/80 film grown on Si substrate, Figure 3.5(a) shows that the a domain thickness is not uniform. There are thick domains (about 100 nm) as well as thinner ones about 20 $\sim$ 40 nm thick in the film. In addition, PFM observation of the thick domains reveals that this is not a single domain, but polytwin plate consisting of alternation of $a1$ and $a2$. These fine $a1$ and $a2$ domains are about 45° to the [010] or [100] direction. The

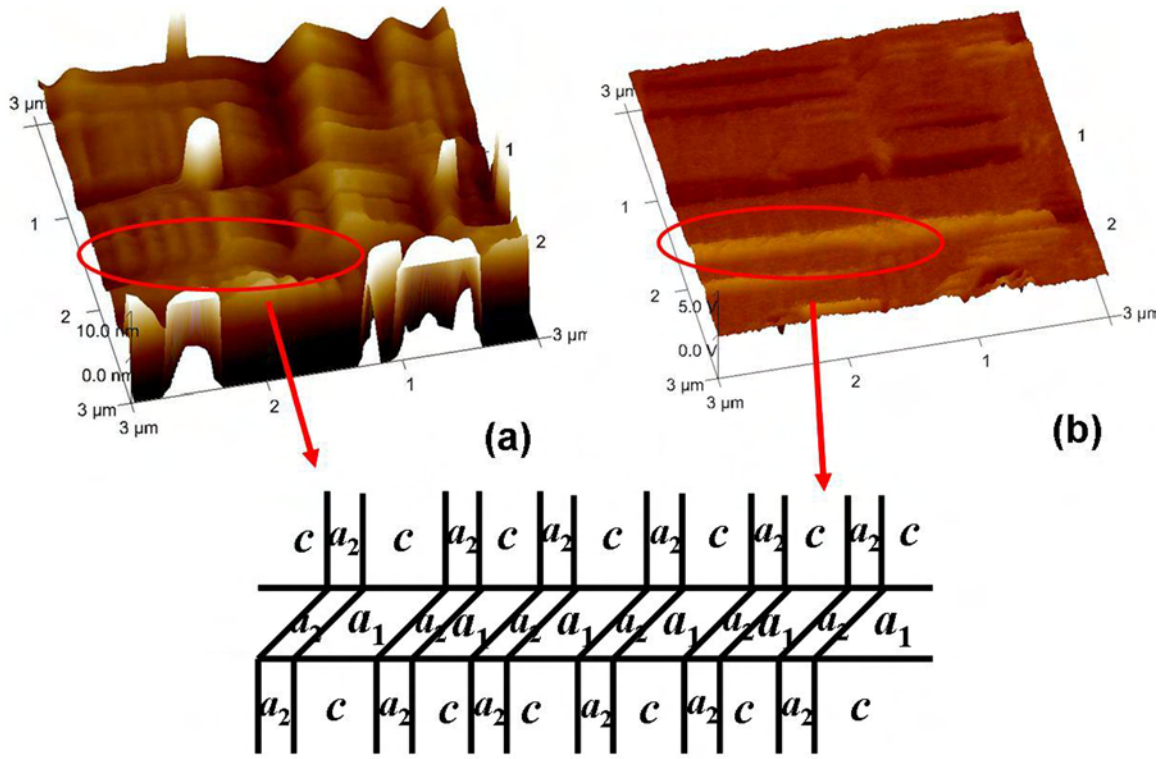

Figure 3.7: Polytwin domain structure in 1 micron thick epitaxial PZT20/80 film on Si substrate. (a) three dimensional topography image;(b) corresponding in-plane signal PFM image. Below is the illustration of the polytwin domain structure

illustration of the fine polytwin domain structure is shown in Figure 3.7. These polytwins are unstable under local electric field.

Figure 3.8(a)-(c) show the topography, in-plane and out-of-plane PFM image of a polytwin plate in the absence of electric field. Figure 3.8(d)-(f) show the same area after locally applying electric field. The $1 \times 1\mu m$ area film is scanned by rastering the conductive PFM tip. There was -15V (i.e. -15MV/m) and +15V (+15MV/m) bias between the tip and the film. It is seen that polytwin disappears under the applied field. The change of topography shows that it transforms to c

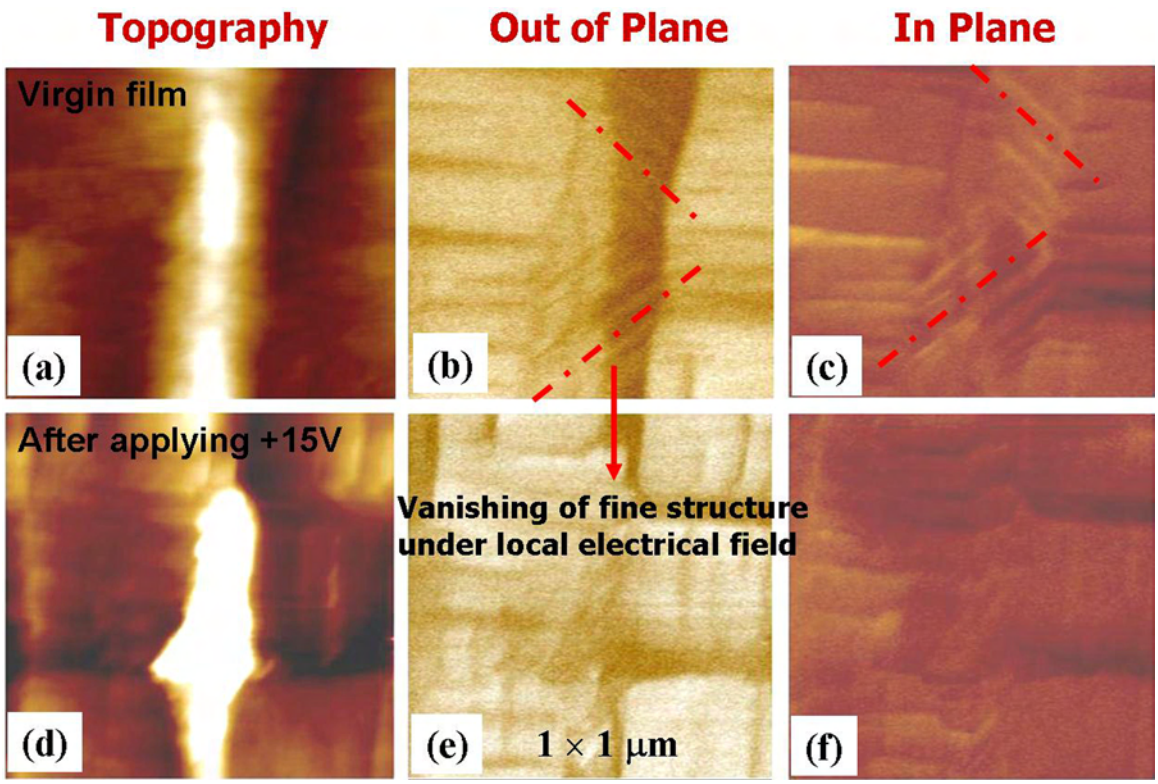

Figure 3.8: domain structure change in thicker a domain (a)-(c) are topography, out of plane, in plane piezoimage of the $1 \times 1\mu m$ area of the $1\mu m$ thick PZT20/80 film before applying electric field (d)-(f) are are topography, out of plane, in plane piezoimage of the same area after applying -15V and +15V voltage in the area

domains.

500 nm thick film

The a domain wall motion under local electric field observed in the 1 μm thickness film can also be observed in a 500 nm film. The 500 nm thick film was characterized and shown in Figure 3.9. There are fewer a domains in 500 nm thick films than in 1μm thick films. Figure 3.10 shows topography and out-of-plane PFM image of a 500 nm film before and after applying local electric field. Before applying

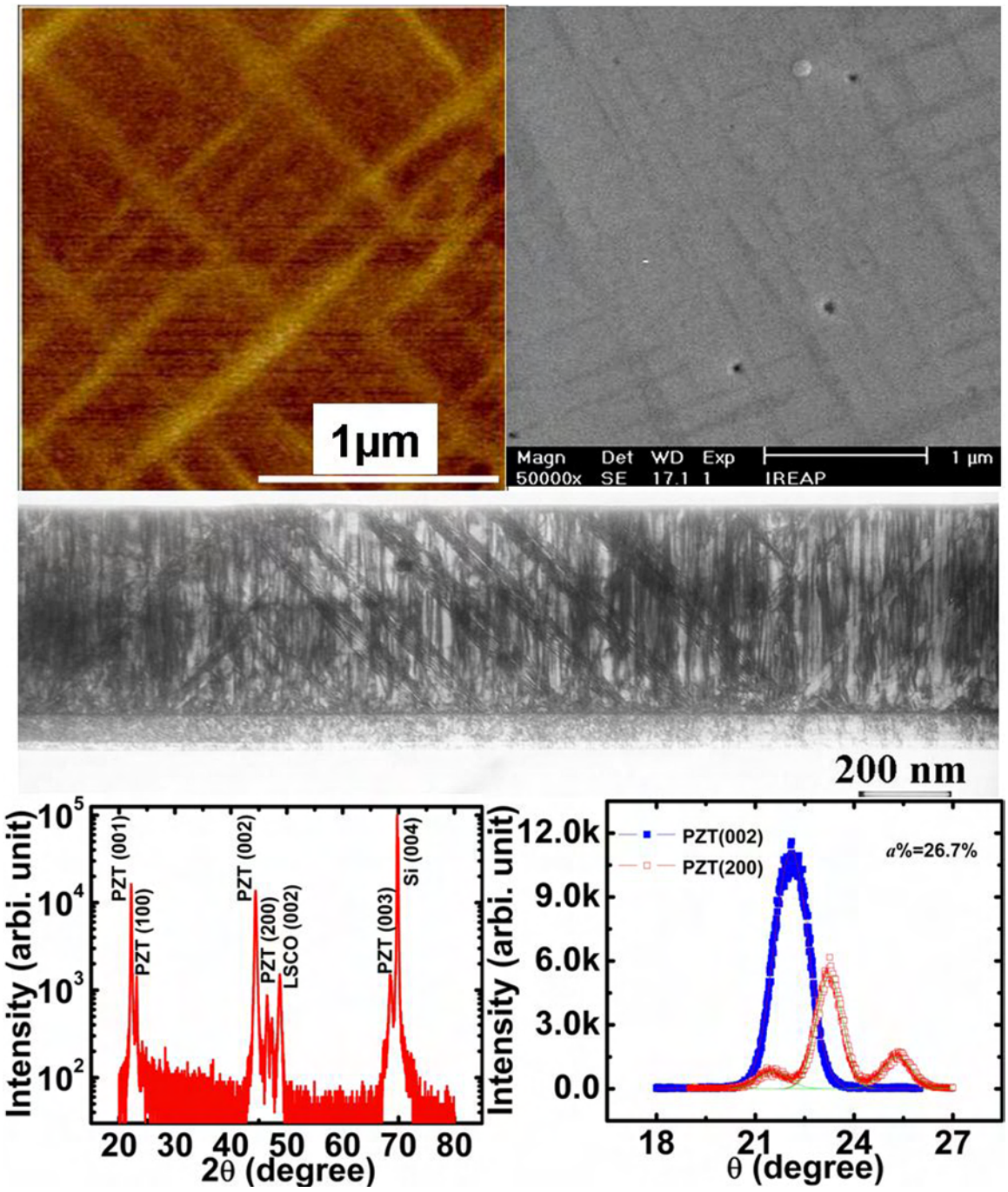

Figure 3.9: Characterization of 500nm thick PZT20/80 on Si substrate.(a) out-of-plane PFM image;(b) SEM image of the film surface; (c) TEM picture of the film; (d) X-ray diffraction of the film;(e) rocking curve of PZT(200) and PZT(002) peak

electric field, there is a long vertical a domain about 100 nm wide. After the center area of $3 \times 3\mu$m is scanned by the PFM tip with a bias voltage of -15V and +15V, this vertical a domain cannot be seen, while the initial c domain has grown about 100 nm to the right, and the topography of the image shows a "bump"in the initial position. Figure 3.11(a) is the line cross section of the topography the same location before and after applying electric field. Figure 3.11(b) and (c) schematically illustrate the change of topography, *i.e.*, how the previous a domain was in-situ transformed into the c domain. According to previous research, the electric field distribution in the film under an applied electric field is highly non-uniform. The actual electric field at the surface of the film can be very high. The a domain may become unstable when the electric field is applied.

3.2.3 Morphological transition of domain structure

Figure 3.12 shows out-of-plane piezoelectric image of a $1\mu m$ thick film before and after applying local electric field. $3 \times 3\mu m$ area of the film is scanned with a -10V bias between the tip and the film. Comparing to the cellular structure of the original film shows that the fine a domains in the center region (where polarization is reversed) were rearranged and formed the hierarchical structure (Figure 3.12(a)(c)). As has been shown by phase field modeling of domain structure in an epitaxial film (Figure 3.13[90][91]), a hierarchical structure becomes more stable than the cellular one with decreasing the fraction of out of plane c do-

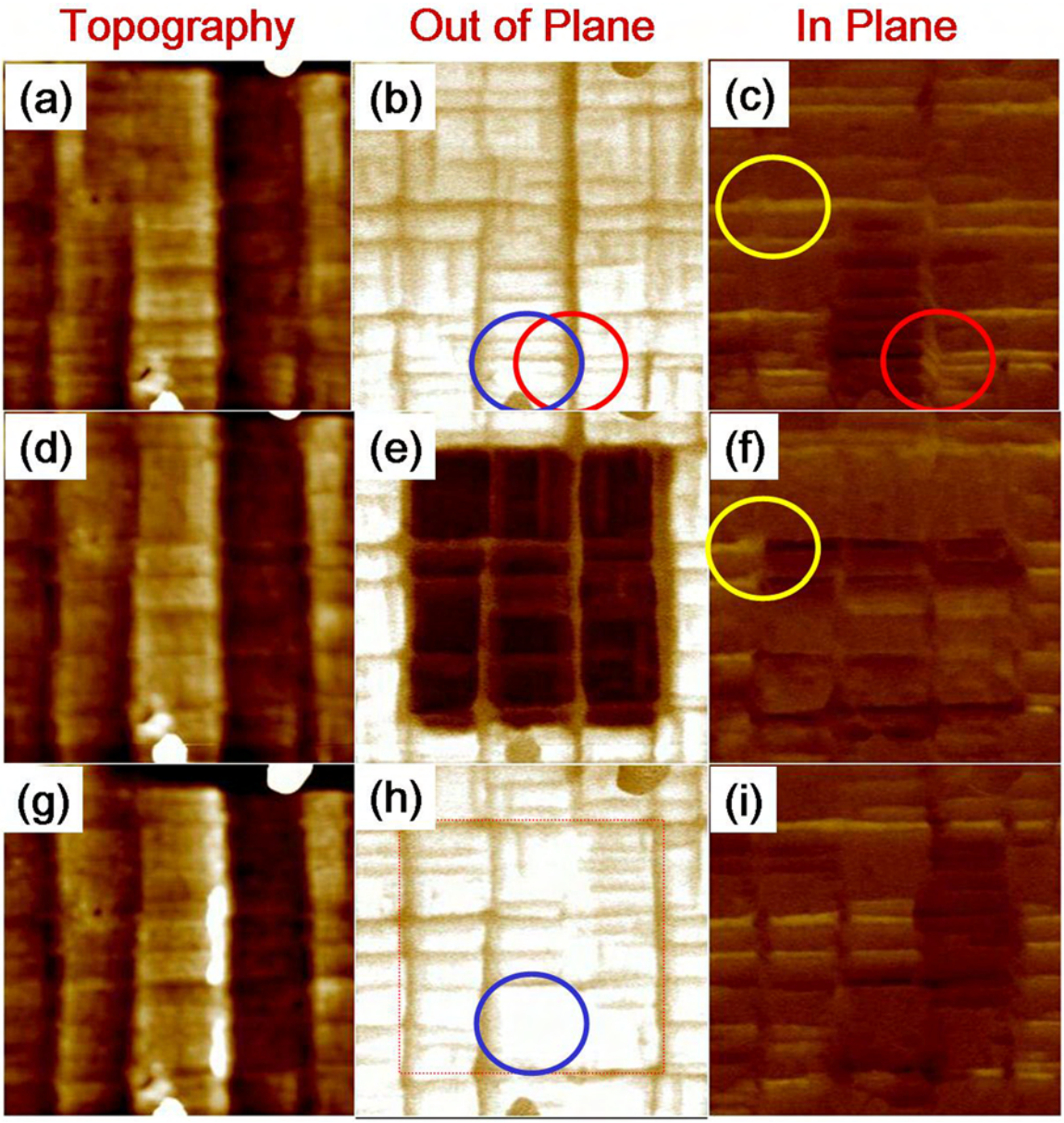

Figure 3.10: Change of domain structure under local electric field in the 500nm film. (a)-(c) are topography, out of plane, in plane piezoimage of the $5 \times 5\mu m$ area of the $500nm$ thick PZT20/80 film before applying electric field (d)-(f) are are topography, out-of-plane, in-plane piezoimage of the same area after applying -15V in the center of the $3 \times 3\mu m$ area and, (g)-(i)after applying +15V voltage in the whole $5 \times 5\mu m$ area

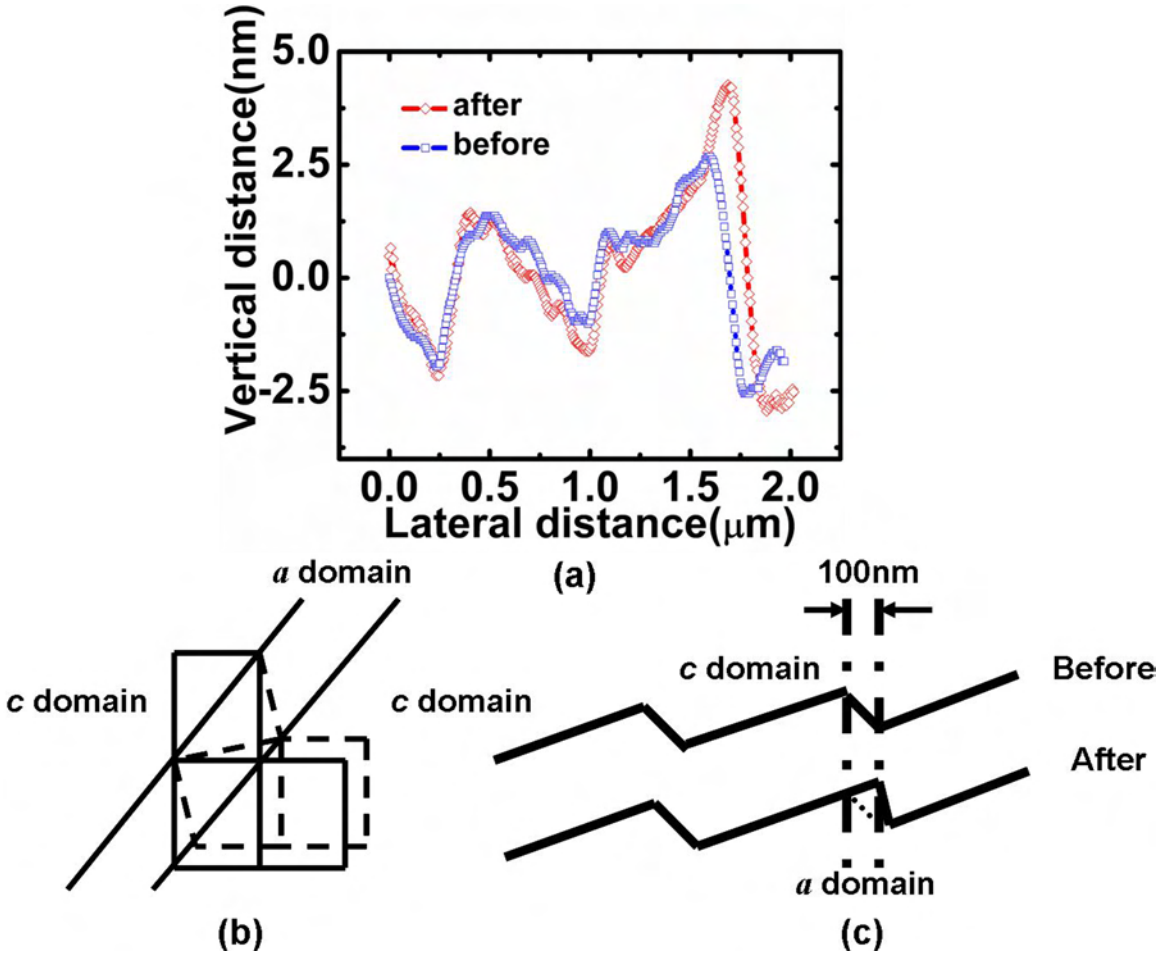

Figure 3.11: Illustration of the change of a domain to c domain under the local electric field. (a) the topography change of the same position before and after applying the electric field; (b) the lattice change before and after a domain changes to c domain; (c) the explanation of topography change before and after a domain changes to c domain

mains(Figure 3.13(b)[90]).In our experiment, the reversed electric field results in decreasing the built-in field which poled the initial film and stabilized the cellular structure, therefore, the fraction of c domain decreases and the cellular structure transforms into the hierarchical one.

The sequences of the images presented in Figure 3.14 and Figure 3.15 demonstrate that the morphology transition does not depend on the size of the area with polarization reversed by local electric field. Figure 3.15 demonstrates that this transformation can be repeated by applying field of the opposite sign.

3.3 Conclusion

Domain structures of $PbZr_{0.2}Ti_{0.8}O_3/SrTiO_3/Si$ continuous films has been investigated by piezoelectric force microscopy (PFM). It is shown that the cellular structure in the films on Si substrate is more complex than has been observed in films on $SrTiO_3$ substrate. It contains polytwin $a1/a2$ plates as well as simple a domains embedded in c domain matrix. The movement of domain wall under local electric field has been observed. Morphological transition between cellular and hierarchical structure theoretically predicted has been observed in the area of reversed polarization. It is shown that this transformation does not depend on the size of switched area. The study allows us to conclude that the domain structure in the PZT film on Si substrate is more flexible than the film on $SrTiO_3$ substrate.

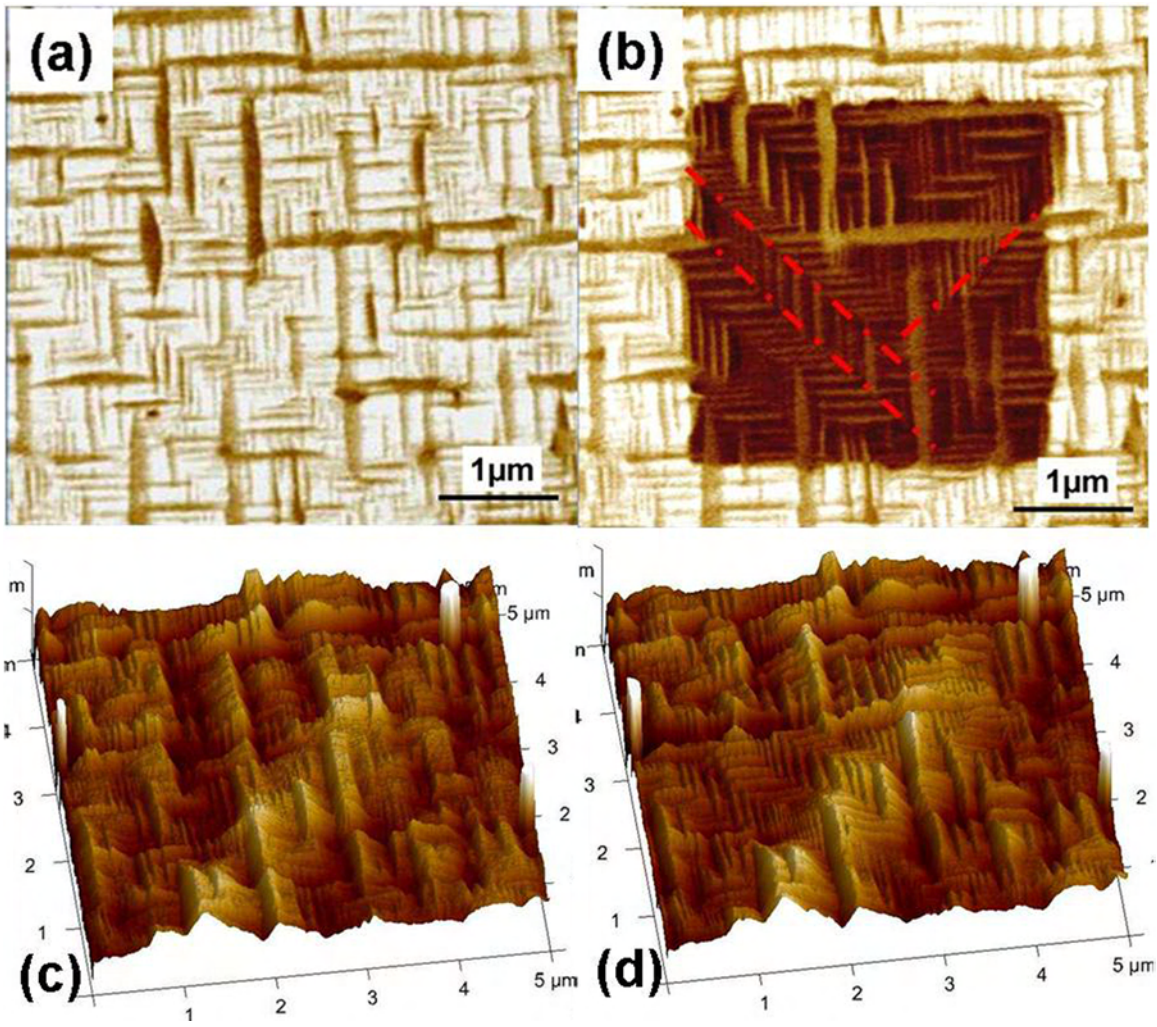

Figure 3.12: Formation of self-organized 90° domain in the $1\mu m$ thick PZT20/80 film grown on Si substrate.(a) out of plane piezoelectric image of virgin film; (b)the out of plane PFM image of the same film after applying electric field of 10MV/m in the center $3 \times 3\mu m$ area; (c)and (d) are three-dimensional images of (a) and (c), respectively

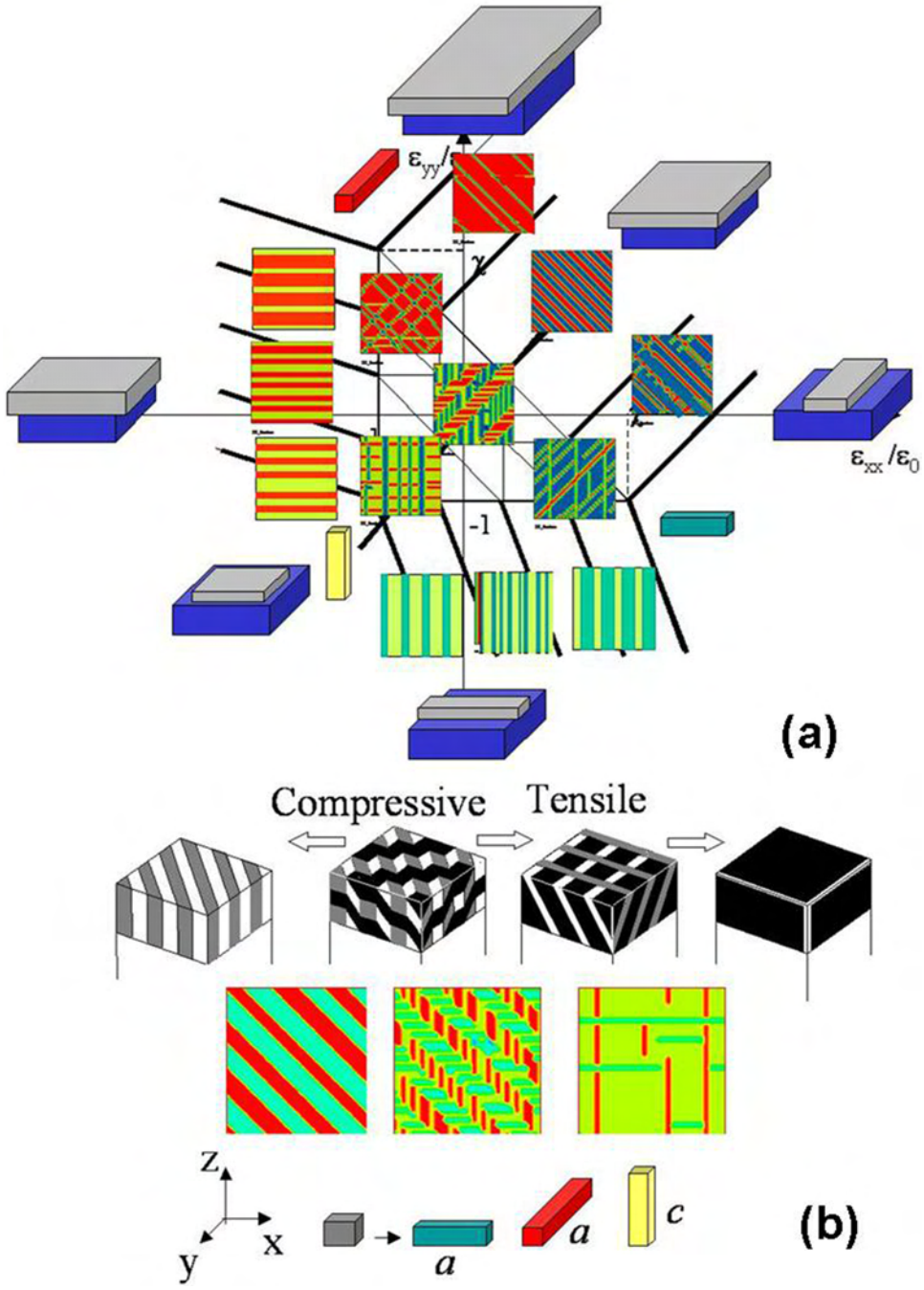

Figure 3.13: Phase field modeling showing (a) polydomain structure in a constrained (001) layers at different biaxial misfit, $(\varepsilon_{xx}, \varepsilon_{yy})$(Slutsker, 2004); (b) The evolution of three-domain polydomain architecture from a two-domain structure to a single- domain one with change of misfit(top). The plane view of the structures obtained by modeling with increasing fraction of out-of-plane domain(bottom)(Slutsker, 2002).

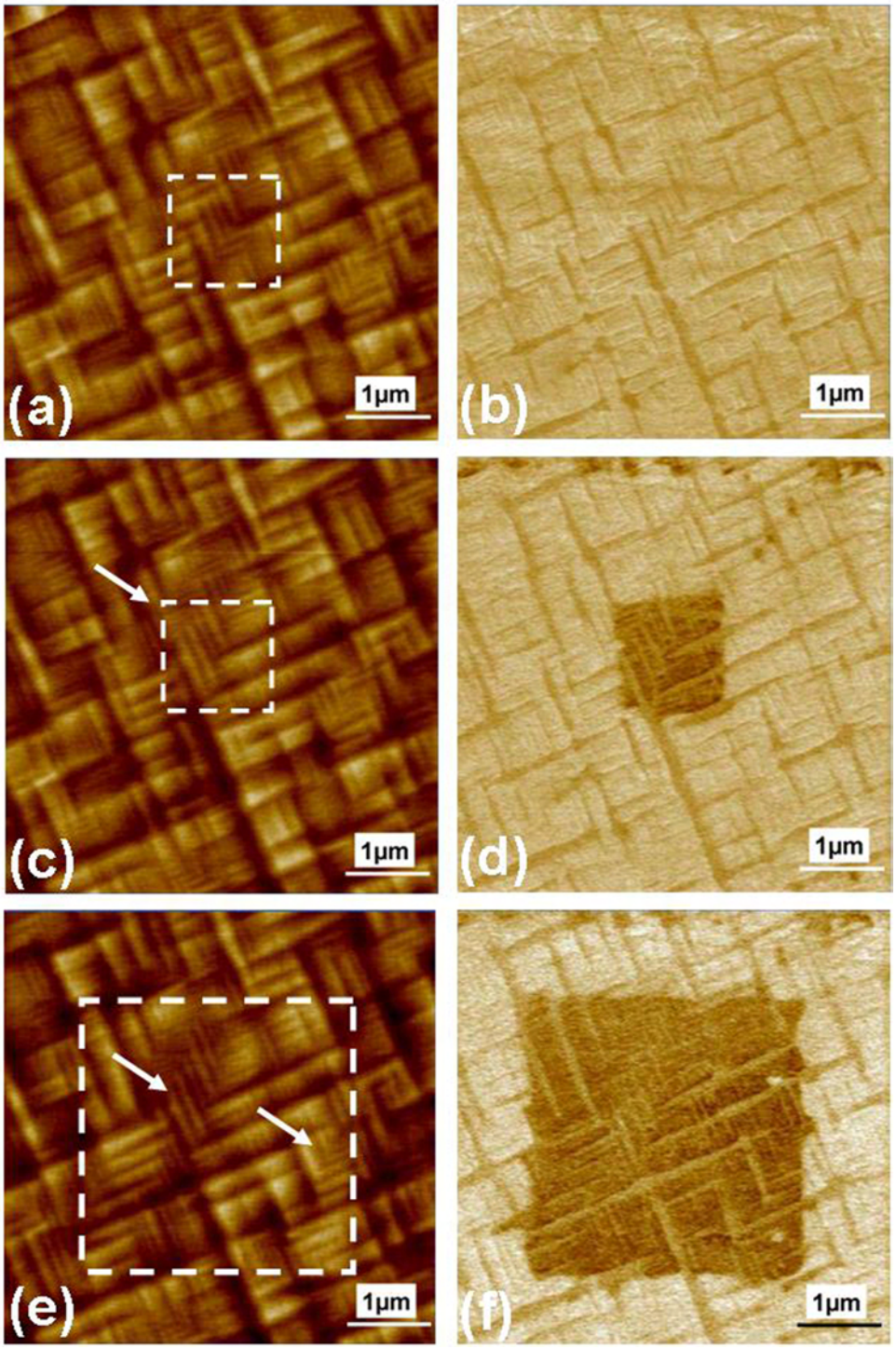

Figure 3.14: The hierarchical domain pattern formation after local electric field application in a $1\mu m$ thick PZT20/80 film grown on Si substrate.(a)(c)(e) topography image of the film; (b)(d)(f) out of plane PFM image of the same film; (a)(b) virgin film of $5 \times 5\mu m$; (c)(d) after applying electric field of -12MV/m in the center area of $1 \times 1\mu m$; (e)(f)after applying electric field of 12MV/m in the center area of $3 \times 3\mu m$. The arrows indicate the positions where hierarchical structures form

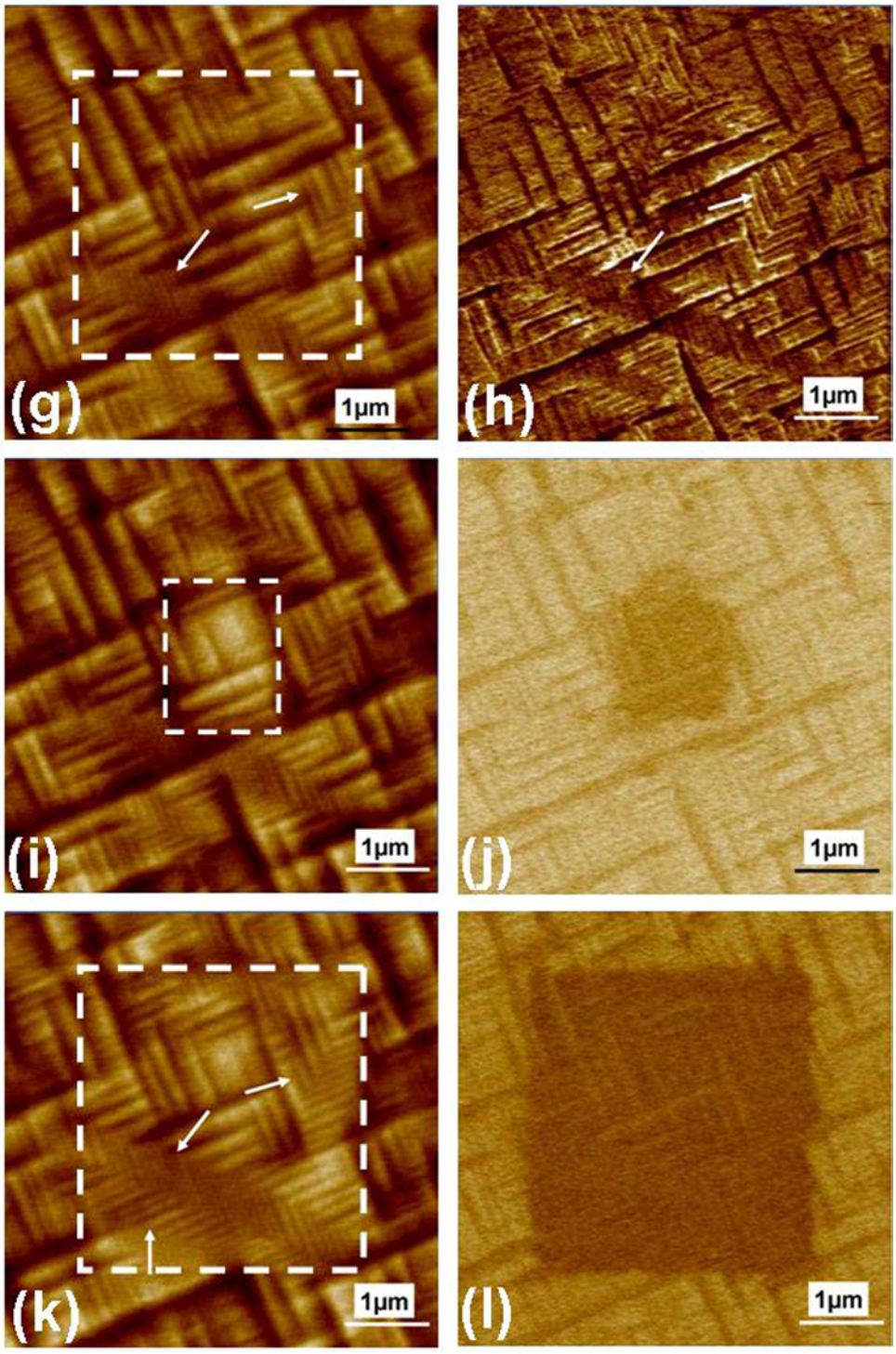

Figure 3.15: The hierarchical domain pattern formation after local electric field application in a $1\mu m$ thick PZT20/80 film grown on Si substrate (continuing).(g)(i)(k) topography image of the film; (h)(j)(l) out of plane PFM image of the same film; (g)(h)after applying electric field of 12MV/m in the whole area of $5 \times 5\mu m$; (i)(j) after applying electric field of -12MV/m in the center area of $1 \times 1\mu m$; (k)(h)after applying electric field of 12MV/m in the center area of $3 \times 3\mu m$.The arrows indicate the positions where hierarchical structures form

Chapter 4

Nanopatterning Effect on Domain Structure and Its Mobility

In this chapter, we first introduce the measurement of converse piezoelectric coefficient by PFM and the polarization measurement, then discuss the domain movement in the FIB patterned cubic and strip-like island island of a 1 micron thick PZT film and square island of a 500 nm thick PZT film. Finally, the study of patterned cubic islands on a 3μm thick lead magnesium niobate-lead titanate (PMN-PT) ferroelectric film is presented.

4.1 Experimental techniques

4.1.1 Nanopatterning of ferroelectric film by Focused Ion Beam technique

Presently much attention has been focused on the application of ferroelectric film as a high density gigabit non-volatile data storage media. As the active memory element shrinks to the nanoscale, due to the increasing high aspect ratio and high surface to volume ratios, the ferroelectric element is subject to problems such as polarization relaxation, fatigue, imprint, and leakage. Thus, it is imperative to understand the fundamental ferroelectric phenomenon at shrinking dimensions. To pattern the film into smaller features, traditional processes in the semiconductor industry include lithography and etching. The former defines the lateral structure by patterning the resist; the latter removes the materials selectively by a developing process. However, for complex oxides such as PZT, etch techniques are still not fully developed. These materials suffer from the common problem that their possible etch products have a very limited volatility, even if reactive gases are used.

In our study, we use the focused ion beam (FIB) technique to pattern the ferroelectric films to micron size scale. This method provides a convenient and flexible way to pattern ferroelectric films. It has the advantage of high resolution (image resolution<50 nm, cut accuracy $\sim$0.1μm) and flexible layout patterning offering either milling or deposition on a maskless surface with or without gas

assistance.

The earliest focused ion beam for microfabrication was produced in Hughes laboratories in 1973 with a beam spotsize of 3.5μm[7]. Currently most FIB systems use a high quality, long-life liquid metal ion source (LMIS) developed in the 1970s, which allows the system to accomplish the tasks more readily[92]. A beam of Ga ions is focused and scanned over the surface of the sample. The interaction of the ion beam with the sample results in ejection of atoms from the surface (sputtering) and the production of secondary electrons and ions. Deposition is also possible in the presence of an organometallic gas, but only under specific operating conditions. An electron flood gun can be used to compensate for the charging induced by the ion beam and to keep the sample more neutral.

Sputtering is the basic ionic impact phenomenon during the process of FIB microfabrication. It is an atomic cascade process, in which the accelerated ions transfer their energy in a series of primary collisions to the surface of substrate, and cause the ejection of surface atoms and ions as well as further collisions within the substrate atoms. The sputter yield, which is the number of substrate atoms removed per incident ion, is generally $1 - 10\%$ per ion, depends on the materials, incident angle of the ion beam and energy of the beam, usually determined by the experiment. Ion milling occurs if the sputter yield is greater than unity. The sputter rate can be increased through gas-assisted etching. The key feature of FIB technology is its capability to localize the modification to only the area requiring

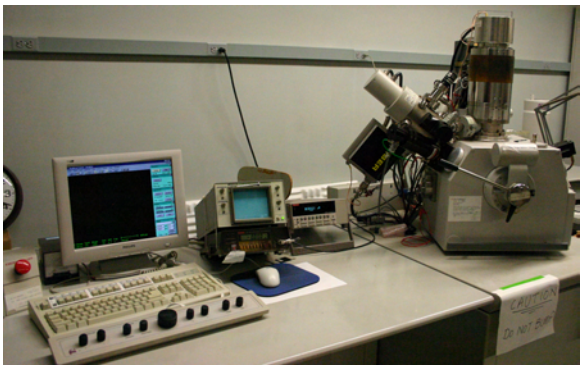

Figure 4.1: Focused Ion Beam equipment.

alteration. FIB systems can be employed to make precision modifications to a variety of samples. This makes the FIB systems an indispensable tool for failure analysis and test structures analysis at chip level as well as the repair of nearly-functional parts. The typical application of the FIB includes: nanoscale device fabrication, optical lithography mask repair or modification, circuit modification, and TEM sample preparation.

Although FIB process has the drawback of low throughput which is not suitable for mass production, the system is good for the specialty devices production with complete flexibility. The FIB equipment used in this work are the Micrion FIB 2500 and the Dual Beam FIB 620 (Figure 4.1). They are both equipped with a liquid gallium ion source. While the former operates at an accelerating voltage of 50 kv with a 5 nm ion column, the latter has a constant operation voltage of 30 kv and 20 nm. The Micrion 2500 has an increased available beam current with a smaller beam spot size, thus it has both a higher resolution and a higher sputter rate. In addition, the Dual Beam combined the FE-SEM with FIB into a single integrated

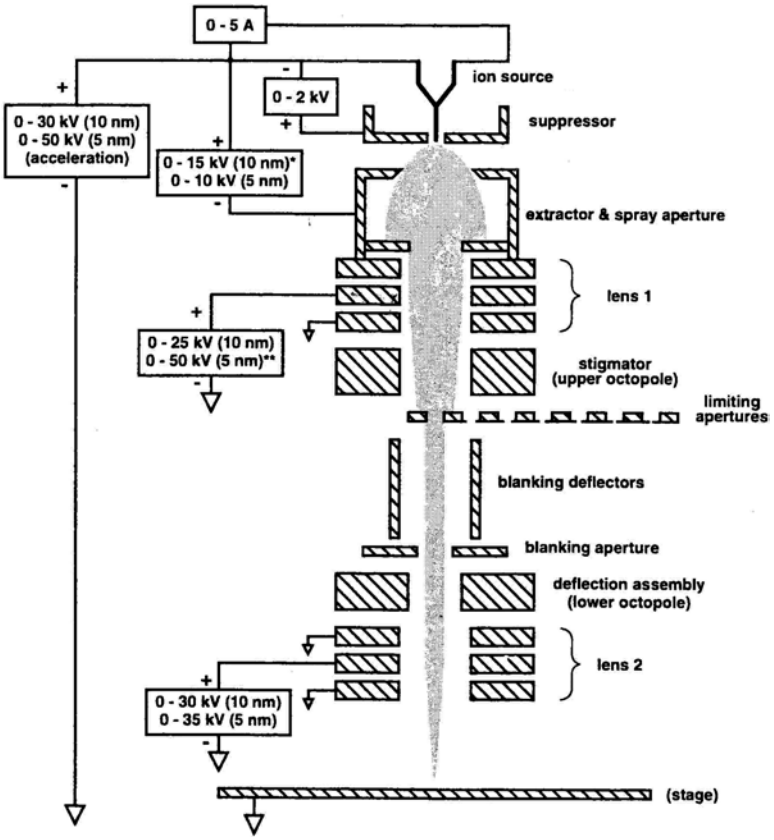

Figure 4.2: Schematic ion column structure of focused ion beam

system, and can provide cross section images real time during FIB milling or afterwards without ion beam erosion or gallium implantation. Figure 4.2[93] shows the schematic picture of the inside structure of an ion column.

In order to decrease the substrate clamping effect[94], the ferroelectric films are patterned into discrete islands by using focused ion beam[95]. The patterned capacitor structure in PZT film is shown in Figure 4.3. The typical heterostructure of the film is Pt/LSCO/PZT/LSCO/STO/Si. The capacitor forms in the film by milling grooves of a certain pattern, and the maximum depth of the removed materials in this work is 1 μm. The typical beam current used is in the range

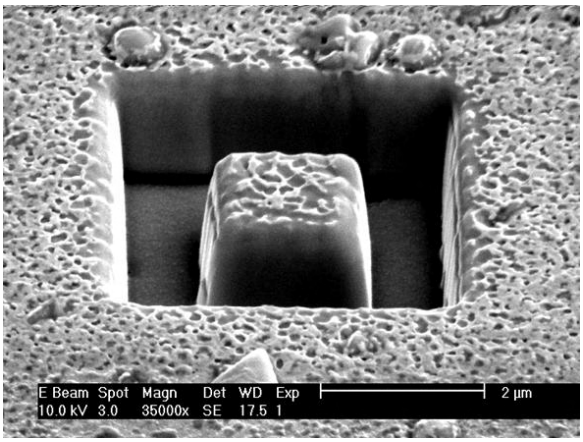

Figure 4.3: $1 \times 1 \times 1 \mu m$ cubic island milled by focused ion beam

of 70-1000 pA, and the corresponding beam diameter is 20-100 nm. The beam scans the desired pattern(s) in parallel or in series by digital serpentine scan, or, *rastering* process as is shown in Figure 4.4. The dwell time in each pixel is set to 10-50 ms. The overlap of the beam is 50% to make sufficient exposure of the film under the beam. The total materials removed by the beam is determined by both the dose (in nC/mm^2) and the sputter yield. To fabricate the capacitor, the milled groove needs to stop at either the PZT layer or the LSCO bottom layer. The end-point analysis curve can help in estimating the stop point during real time milling. It is a graphical representation of the intensity of secondary particle emission. When layer boundaries of dissimilar materials are crossed, the secondary emission rate changes, and the curve rises or falls as each underlayer is uncovered. The schematic end-point analysis curve is shown in Figure 4.5[93]. The ion milling is effective in making most structures, but there are some drawbacks which need to be mentioned. When fabricating narrow deep grooves, redeposition of the sputtered

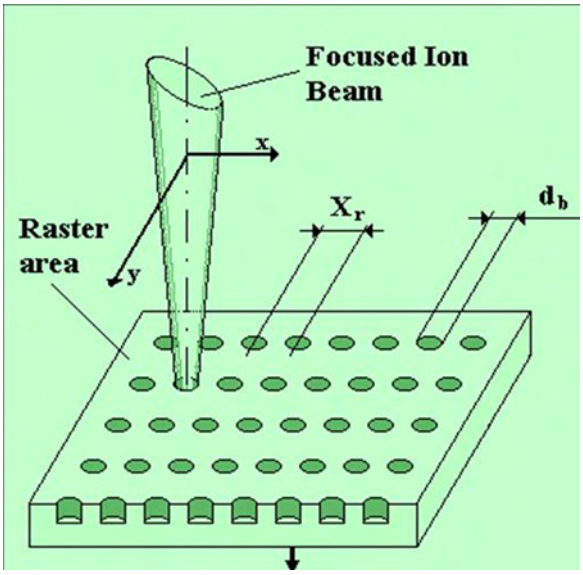

Figure 4.4: Raster milling process of focused ion beam

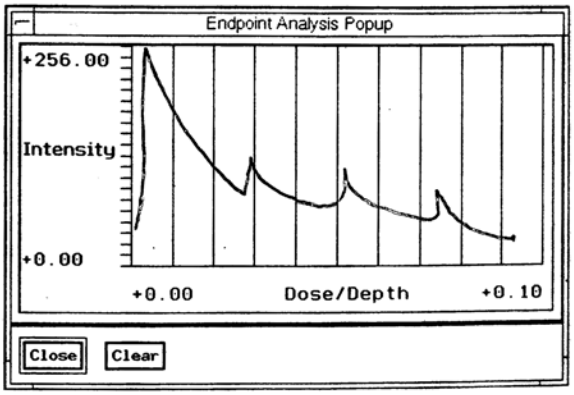

Figure 4.5: End point analysis of focused ion beam

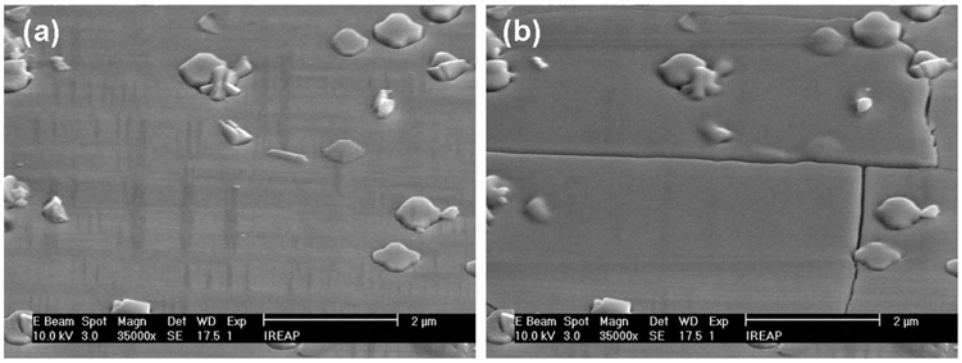

Figure 4.6: Crack formation after the film is exposed to the Ga ion beam for half a minute. (a) before exposure;(b) after exposure

material on the side wall leads to a "V" shape groove. To avoid this problem, the larger width of the grooves is needed to decrease the aspect ratio, or the sidewall needs to be trimmed to keep it straight. Another drawback is the ion damage caused by the heavy gallium ion implantation. When the film is exposed under the ion beam, the film will be damaged, as shown in Figure 4.6. Stanishevsky[96] studied the effect of ion dose on the hysteresis loop of ferroelectric films, which is shown in Figure 4.7. The Ga ion bombardment on the film surface will destroy the periodic structure of the crystalline, resulting in the loss of ferroelectric properties. This surface damage can be avoided by depositing a protection layer before ion milling and later washing it away by a lift-off technique, followed by annealing that recovers the ferroelectric properties. In our work, we first deposited 500 nm thick PMMA by a standard spin on technique, and then a Ti layer of about 100 nm is deposited on the top of the PMMA by RF sputtering. After patterning the film, the PMMA as well as the Ti layer can be washed away by acetone. After the

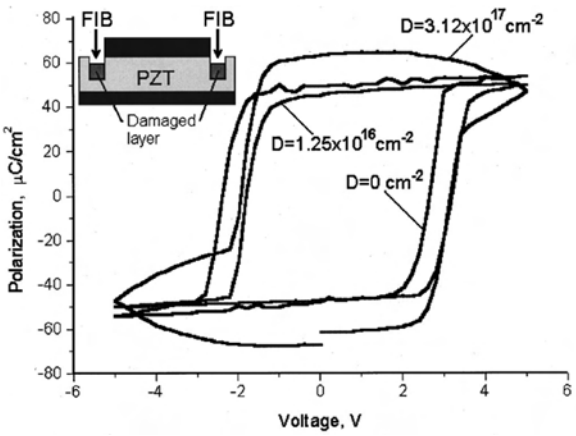

Figure 4.7: The effect of ion dose on the hysteresis loop of ferroelectric films (Stanishevsky, 2002)

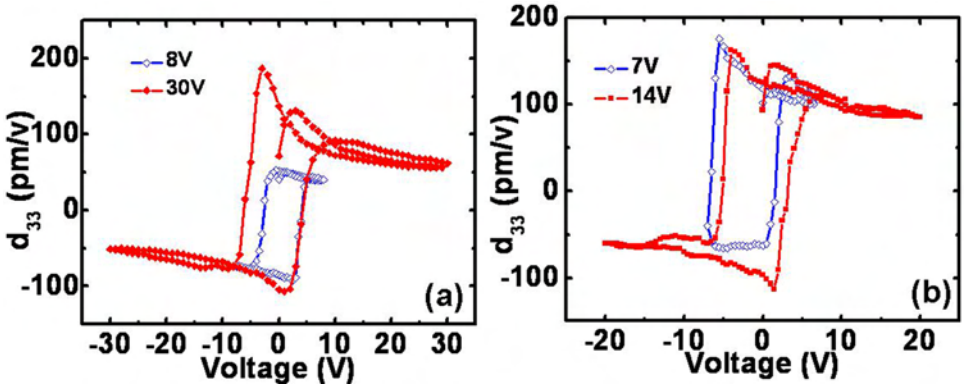

Figure 4.8: The piezoelectric property of patterned device after ion beam milling using the protection layer.(a) before annealing; (b) after annealing

film is protected during the milling, and using the smaller ion current, the device retains piezoelectric properties even before annealing(Figure 4.8). After annealing, the ferroelectric properties are fully recovered as indicated in Figure 4.8.

4.1.2 Piezoelectric coefficient measurement

The piezoelectric property of the ferroelectric films is an important indication of the film quality and also closely related to MEMS related applications. Both a laser

interferometer [52][97]and a piezoelectric force microscope [98][94][99]can be used to measure direct and indirect piezoelectric coefficients. Due to the small response of the film under the electric field, special care needs to be taken while measuring and interpreting the piezoelectric data of the film. In this work, piezoelectric measurements are performed with a piezoelectric force microscope. The schematic of the experimental setup is shown in Figure 3.4.

The principle of piezoelectric coefficient measurement is the same as domain imaging by PFM. Instead of applying a AC signal to "read"the surface displacement, an external combination of DC + AC voltage is applied through the conductive AFM tip, which serves as a probe to detect the hysteresis relationship between piezoelectric response and the external electric field. The measurement is based on the detection of the local electromechanical vibration of the ferroelectric sample caused by the external voltage. The external driving voltage of certain frequency ω, which is much smaller than the resonance frequency of the cantilever, is applied to the sample surface through the tip, and causes the surface to vibrate at the same frequency due to the inverse piezoelectric effect. The surface displacement is shown in Equation (3.1). The deflection response signal of the tip, which vibrates with the sample surface, is detected by photodiode and translated to quantitative piezoelectric coefficient by calibration using a standard X-cut quartz, so the inverse piezoelectric coefficient d_{33} can be expressed as:

$$d_{33} = \frac{(lock-in\ reading) \times (d_{11}\ of\ quartz)}{(conversion\ constant) \times (V_{AC}\ used\ to\ acquire\ the\ d_{33}\ loop)} \tag{4.1}$$

in which conversion constant is obtained from the slope of linear relationship between piezoelectric response of X-cut quartz and the amplitude of AC electric field.

4.1.3 Characterization of ferroelectric properties by polarization measurement

The hysteresis loop of polarization change with electric field, which is characteristic of ferroelectric materials, is measured by either the RT6000 for large capacitors, or by the TF ANALYZER 2000 for micron size capacitors. Here we focus on the polarization measurement of micron-size capacitor. A big problem associated with the measurement of the small-size capacitor is the parasitic capacitance from the circuit. Figure 4.9 shows the measured polarization hysteresis loop with different capacitor size. The parasitic capacitance has larger effect with the scaling of the capacitor size, therefore must be subtracted from the measurement result. This can be accomplished by either measuring parasitic signal itself, or simply obtain the slope of the hysteresis loop (the parasitic signal is linear) and subtracted from the total signal[100].

The TF ANALYZER 2000 is the modular designed for the electrical characterization system for both electroceramic thin film and bulk ceramic samples. The system offers four modules. We use the FE-module in our experiment to obtain the hysteresis relationship of polarization and electric field. FE module can be used

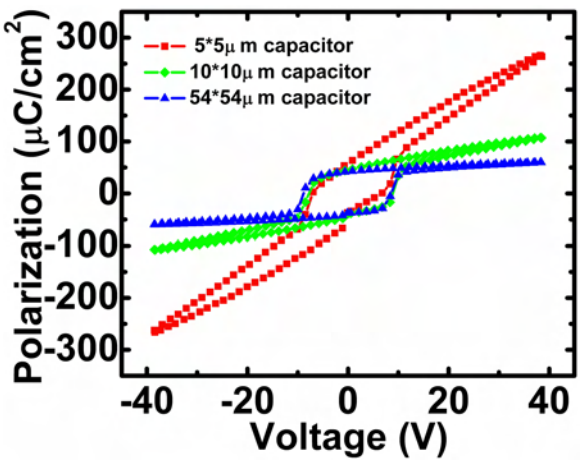

Figure 4.9: Effect of capacitor size on the polarization measurement

to measure the hysteresis loop using either the quasi static or dynamic hysteresis measurement[101]. The system consists of the Basic Unit, where the computer and the high precision power supplies are located, and the Probe Head, which the specific amplifiers are located. The Probe Head can be put very close to the sample to pretty much reduce the loop between drive and return, so it can be connected to any kind of probe station with shorter cables. The setup has an optimum signal to noise ratio by using different amplifier for different measurement type. For the dynamic hysteresis measurement, the system offers an amplifier with the amplitude up to $44V_{pp}$, and allows measurement cycle times between 1 second and 1 ms. The current response of the device during test is detected by another amplifier and the data collected by feedback method. This method has the advantage of reducing greatly the effect of parasitic capacitance and back voltage known from the Sawyer Tower measurement. The measurement setup is shown in Figure 4.10. The probe station in the figure is actually an atomic force mi-

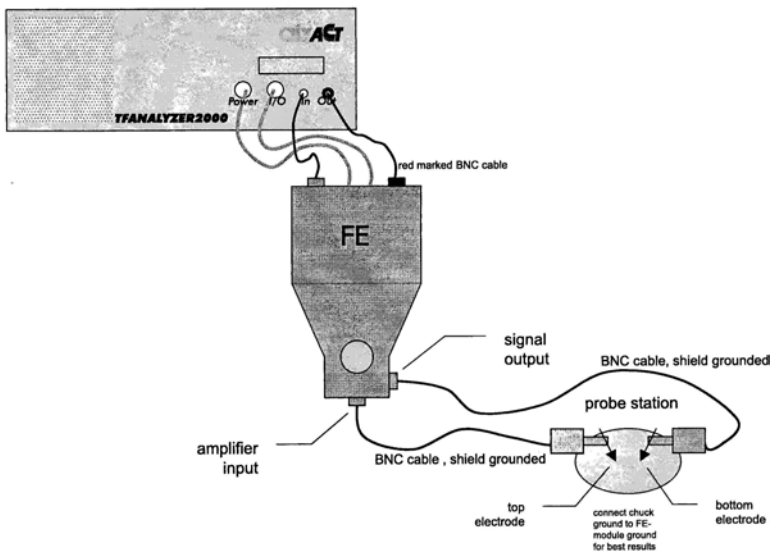

Figure 4.10: The polarization measurement setup for the ferroelectric film capacitor

croscope (AFM) when measuring capacitor at micron size, the conductive AFM tip serves as a probe, in contact with the top electrode of the capacitor, whereas the bottom electrode of the capacitor is connected with the other probe. The dynamic hysteresis program can record characteristic values of a hysteresis loop in a frequency range between 1Hz and 1kHz. In addition, the frequency and amplitude of the excitation signal can also be varied. The typical measurement result by the dynamic hysteresis measurement is shown in Figure 4.11. In which, V_{c+} and V_{c-} are positive and negative coercive voltage, respectively, P_{r+} and P_{r-} are positive and negative state of remnant polarization respectively, and P_{rrel+} and P_{rrel-} are positive and negative state of relaxed remanent polarization, relaxed for one second in the P_r state. It can also characterize the polarization saturation P_s and change of polarization in the switching case and non-switching case. The

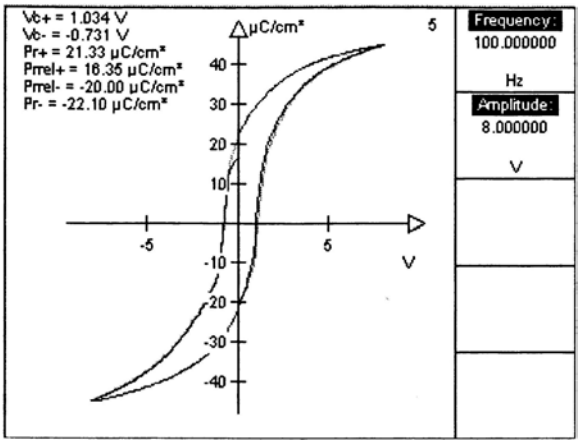

Figure 4.11: The typical polarization measurement result for the ferroelectric film capacitor

triangular voltage excitation signal for the measurement is shown in Figure 4.12. It consists of a pre-polarization and three consecutive bipolar excitation pulses, each separated by 1 second relaxation time. The pre-polarization pulse is to set up a defined polarization state, which in this case is the negative state of relaxed remanent polarization. The first pulse starts in the negative relaxed remnant polarization state (P_{rrel-}) and turns into the positive saturation state (P_{max+}). When the voltage reaches zero, the polarization equals the positive remnant polarization (P_{r+}), then it turns to the negative saturation (P_{max-}) and back to the remnant polarization state (P_{r-}). This value is usually different from the starting point (P_{rrel-}) because of the polarization loss over time. The second pulse switches the sample into positive remanent polarization state without sampling data. The third pulse starts from the the positive relaxed remanet polarization state (P_{rrel+}), turns into the negative saturation(P_{r-}), becomes negative remnant polarization state at

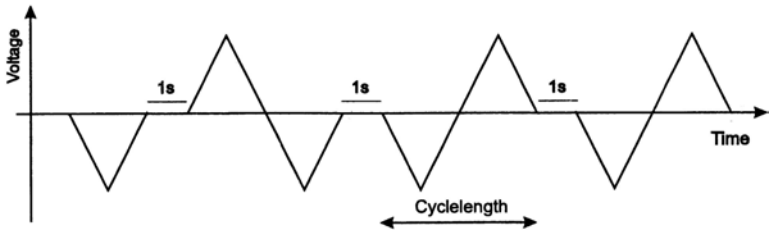

Figure 4.12: The excitation signal for hysteresis measurement

zero excitation voltage signal, finally drives into the positive saturation (P_{max+}) and ends in the positive remnant polarization state (P_{r+}). After that, the data is balanced, respectively, to the values of $P(+V_{max})$ and $P(-V_{max})$. From the first loop the parameters of V_{c-}, P_{r-} and P_{rrel-} are determined and from the third loop $V_{c+}, P_{r+}$and P_{rrel+} are determined. The final hysteresis loop is calculated from the second half of the first and the third loop.

4.2 Experimental results

4.2.1 Patterned structure in 1 micron thick PZT film

Cubic island

Figure 4.13(a) and (b) shows the SEM and PFM image of the domain structure of the square island. It is seen that domain structure on the square island capacitor is the cellular $c/a1/a2$ structure, similar to the structure of the continuous film in morphology as well as the density of the domains. Observation on PZT islands $\sim 1\mu$m grown by hydrothermal synthesis shows similar cellular domain structure

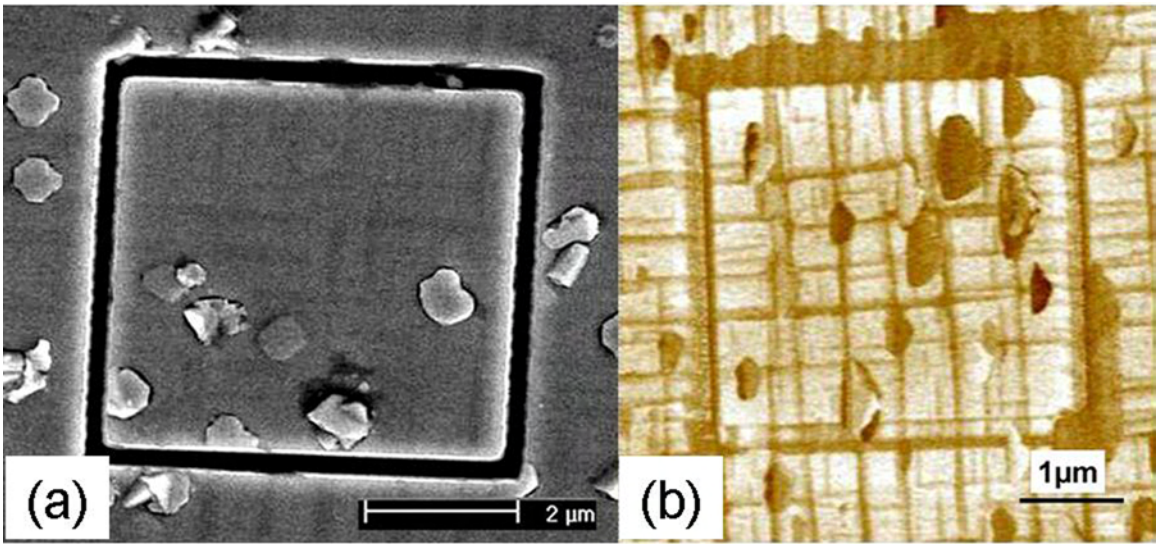

Figure 4.13: SEM (a) and out of plane PFM image (b) of square island of 1μm thick PZT20/80 film grown on Si substrate

as that of the continuous film[102].

Figure 4.14 shows the longitudinal piezoelectric polarization P_r and d_{33} versus maximum applied electric field for the cubic island structure as well as the continuous film. As shown in Figure 4.14(b), the polarization of the island increases to that of the single domain ($\sim 80\mu C/cm^2$) at 12 MV/m, indicating that almost all a domains change to c domains via 90° domain wall movement. On the contrary, the polarization of the continuous film ($\sim 40\mu C/cm^2$) indicates the mixture of c and a domains in the film. At about the same electric field (12 MV/m), it is seen from Figure 4.14(d) that d_{33} of the island has a peak value close to 400pm/V. This value is more than four times larger than the theoretical value of a bulk single crystal (87 pm/V), and eight times larger than d_{33} measured for the continuous film ($\sim$ 50pm/V). Decreased substrate clamping and constraint by surrounding

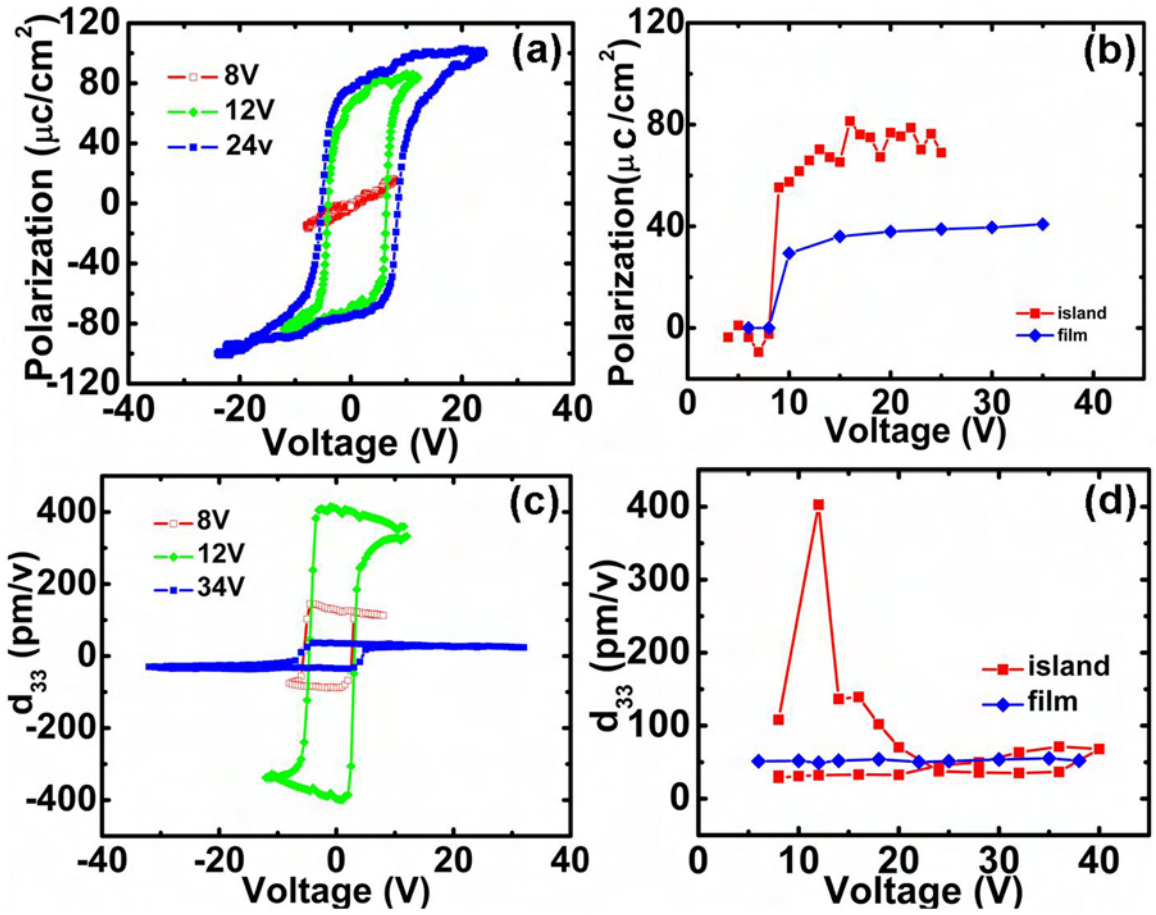

Figure 4.14: Ferroelectric and piezoelectric properties of 1μm thick cubic island patterned on the PZT20/80 film grown on Si substrate. (a) hysteresis loop of polarization for different voltage; (b)change of polarization with maximum applied voltage; (c) hysteresis loop of piezoelectric coefficient d_{33} for different electric voltage; (d)change of piezoelectric coefficient d_{33} with maximum applied voltage.

material cannot explain why the d_{33} of islands dramatically increases, unless an extrinsic contribution of 90° domain movement is taken into account. Based on the PFM observations, we propose that the fraction of a domains start to decrease at about 10MV/m, and most of a domains transform to c domains at about 12MV/m. The movement of a domain is observed to be partially reversible in islands: when the electric field is decreased from 40MV/m, there is no jump of the d_{33}, but the d_{33} value is close to that of the continuous film, indicating that there should be some new 90° domains formed when the applied field decreases.

Strip structure

It has been noted in [6] that patterning an epitaxial film into a narrow strip should diminish the misfit stress across a strip width. For a strip width smaller than its height, the stress state approach the uniaxial one and can be relaxed due to formation of a two-domain polytwin sequence. We employ this design idea to fabricate strip-like islands with the width/length ratio 1 to 8. The PFM and SEM images of the domain structure of strip-like islands are presented in (Figure 4.15). It shows clearly that the domain configuration of the strip structure is periodic $a1/c/a1/c/a1$ structure, the $a2$ variant, which is parallel to the long edge of the strip, is disappeared. The domain period along $\langle 010 \rangle$ direction is similar to that of the continuous film in the same direction, and is less affected by the ion beam milling. This change from the three-domain structure in the film to two domain

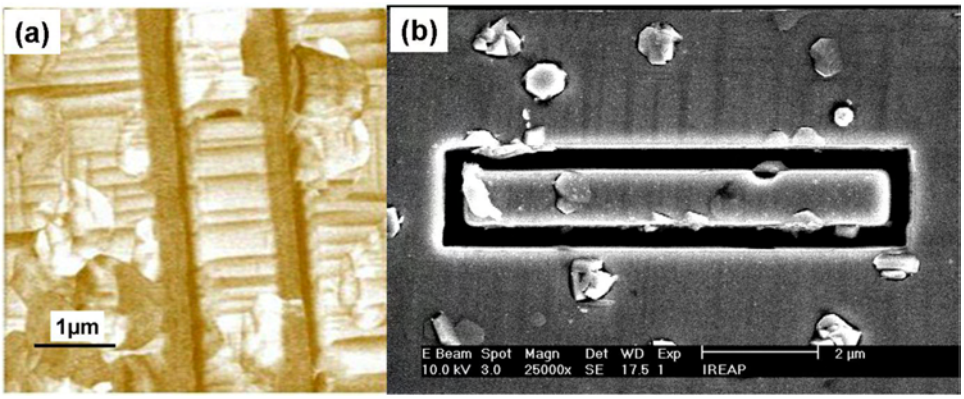

Figure 4.15: The periodic $c/a1/c/a1$ domain structure formation in the long strip island. (a) out of plane PFM image of a $8 \times 1 \mu m$ long strip island in the PZT20/80 film grown on Si substrate; (b) SEM picture of a $5 \times 1 \mu m$ long strip island in the PZT20/80 film

one in the strip island after FIB nanopatterning and annealing is due to the change of the stress field in the strip island. After patterning the film into long island, the constraint along the short side of the strip is released. The in-plane stress in the strip structure is asymmetrical, therefore one set of a domain is sufficient for the stress relaxation. This is also supported by the cross section TEM picture (Figure 3.6), in which only one set of a domain is observed while the other set of a domain is missing. The periodic two-variant domain structure formation by this nanopatterning technique has not been seen reported in any literature up to now.

The effect of local DC electric voltage on the strip structure is shown in Figure 4.16. The 3μm$\times 3\mu$m area of the 5μm$\times 5\mu$m film containing partial of 8μm$\times 1$ μm strip island is written by 10V, -15V, +15V, -20V and 20V respectively. The surface displacements along a horizontal and a vertical line is recorded to observe the change of topography under the local electric field. From the vertical topog-

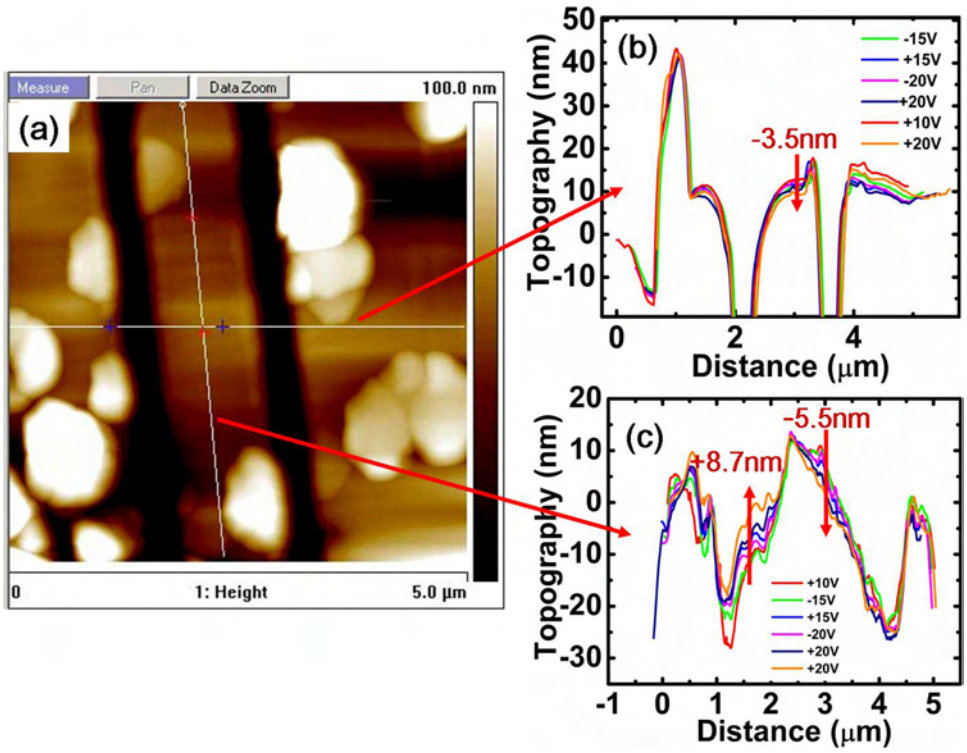

Figure 4.16: Effect of local DC electric voltage on a $8 \times 1\mu$m island strip structure patterned in a PZT20/80 film grown on Si-substrate. (a) topography;(b) topography *vs.* horizontal distance of a horizonal line cross section; (c)topography *vs.* vertical distance of a vertical line cross section;

raphy, it can be seen that the surface displacement changes with electric field. The magnitude of the displacement change depends on the position measured. In some locations, the changes are positive; while in other locations they are negative. This is probably due to the local 90° domain movement in the island. The absolute values of displacement are in order of a few nanometers.

As shown above, the domain structure changes from three domain variants to two domain variants due to nanopatterning. We measured the piezoelectric and ferroelectric properties to see if the change in the domain configuration can lead to the property change. Figure 4.17 shows the polarization P_r and longitudinal

piezoelectric d_{33} versus maximum applied electric field for the strip structure as well as the continuous film. There are two steps in the relationship of polarization vs. maximum applied electric field (Figure 4.17(b)). The first step at about 10MV/m electric field has the polarization value of ($\sim 60\mu C/cm^2$), which corresponds to the polydomain strip containing 30% a domain. The polarization value of the strip jumps to the second peak value ($\sim 80\mu C/cm^2$ at about 20MV/m), this corresponds to the single domain state of the strip island. Similar to the cubic island, a peak value is shown in the relationship of d_{33} $vs.$ maximum applied electric field (Figure 4.17(d)). This peak value is about 470pm/V at 20MV/m. Comparing (Figure 4.17(b)) with (Figure 4.17(d)), the peak value of d_{33} in Figure 4.17(d) can be explained by the movement of 90° domain.

The piezoresponse of the patterned structure and continuous film under AC electric field is shown in Figure 4.18. The cubic and strip island has similar nonlinear piezoresponse at similar voltage while continuous film shows no apparent nonlinearity. The nonlinearity has a peak value of about 270pm/V for the strip island, which is higher than that of the cubic island (∼100pm/V).

The similar phenomenon of improving the mechanical property by patterning was observed in a patterned shape memory alloy film cantilever, which the transformation induced deflection of SMA/Si cantilever bimorphs is increased in comparison to cantilevers with planar film [103]. The difference is due to the stress state of the composite that are determined by the dimensionality of the film. The

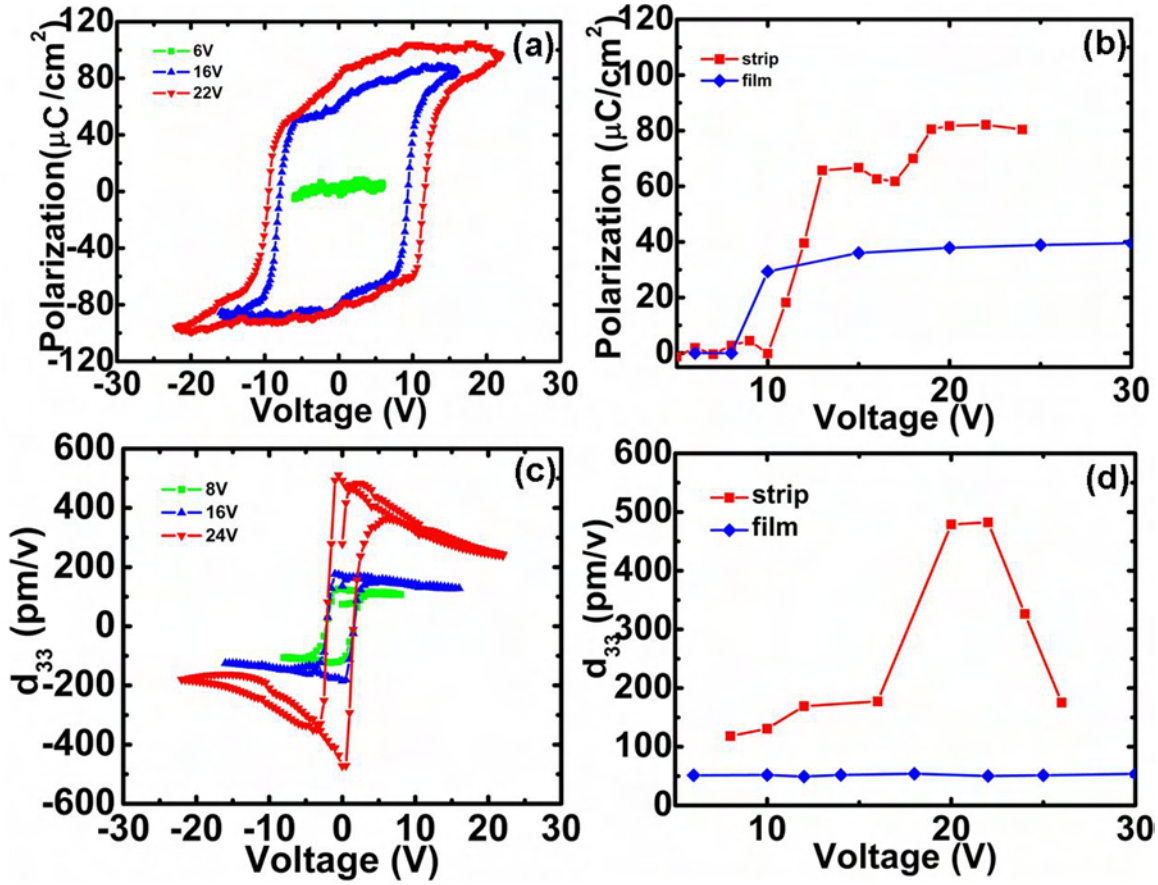

Figure 4.17: Ferroelectric and piezoelectric properties of 1μm thick strip patterned on the PZT20/80 film grown on Si-substrate. (a) hysteresis loop of polarization for different voltage; (b)change of polarization with maximum applied voltage; (c) hysteresis loop of piezoelectric coefficient d_{33} for different electric voltage; (d)change of piezoelectric coefficient d_{33} with maximum applied voltage.

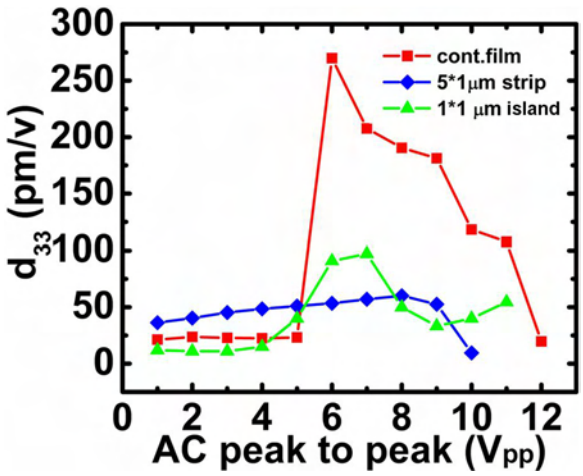

Figure 4.18: Piezoelectric response under AC electric field of patterned structure and continuous film

increase of piezoelectric properties observed in the strip structure in this work can also be explained by the two variant domain structure created by the uniaxial stress field[6].

4.2.2 Square island in 500nm thick PZT film

The above nonlinearity of piezoresponse is also observed in square island of 500nm thick PZT20/80 film. Figure 4.19 shows the longitudinal piezoelectric d_{33} and polarization P_r versus electric field for the cubic island structure as well as the continuous film.

Comparing the square island of $1\mu m$ thick to the square island of 500nm thick Figure 4.20, it is seen that peak value of piezoresponse of a 500nm thick island is less than that of 1μm thick island. Moreover, The electric field at which a domain start to move is almost double for a 500nm thick island compared to the 1μm

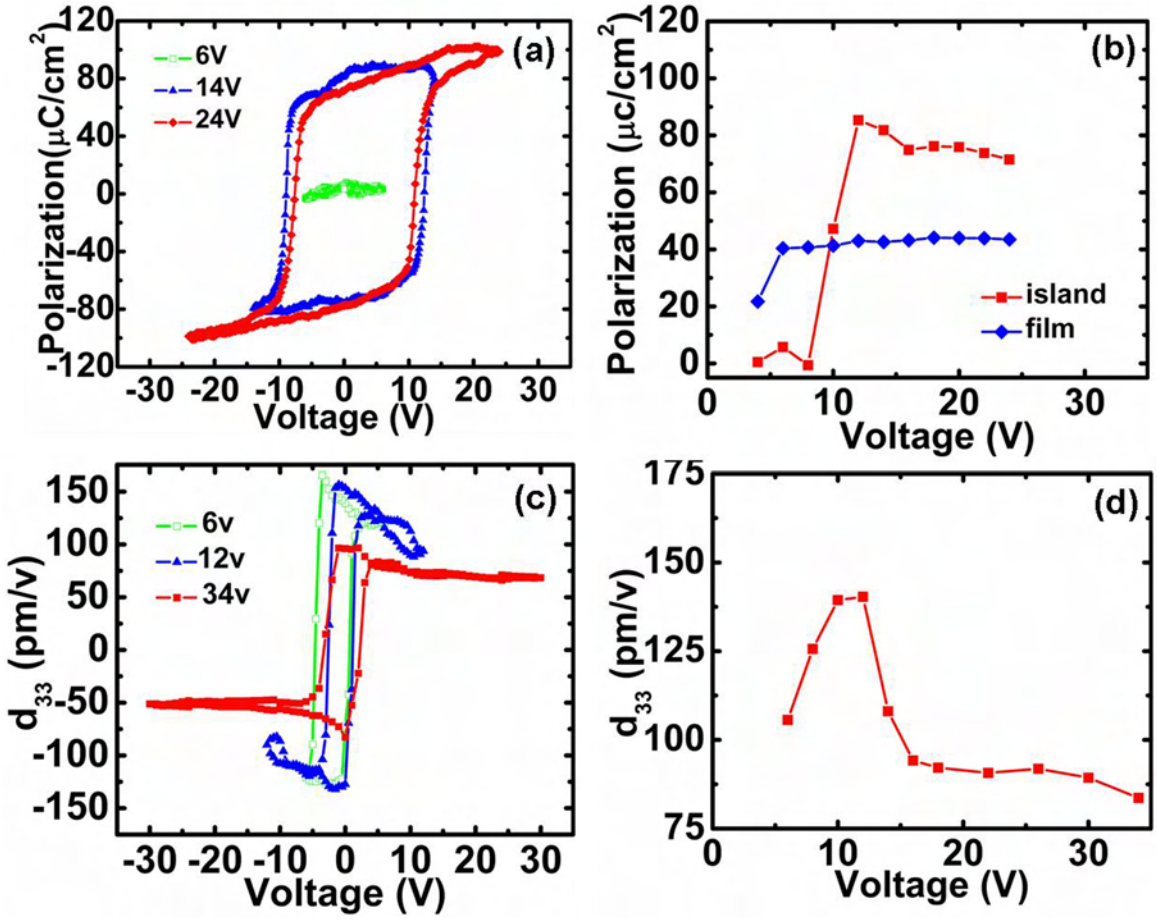

Figure 4.19: Ferroelectric and piezoelectric properties of 500nm thick square island patterned on the PZT20/80 film grown on Si-substrate. (a) hysteresis loop of polarization for different voltage; (b)change of polarization with maximum applied voltage; (c) hysteresis loop of piezoelectric coefficient d_{33} for different electric voltage; (d)change of piezoelectric coefficient d_{33} with maximum applied voltage.

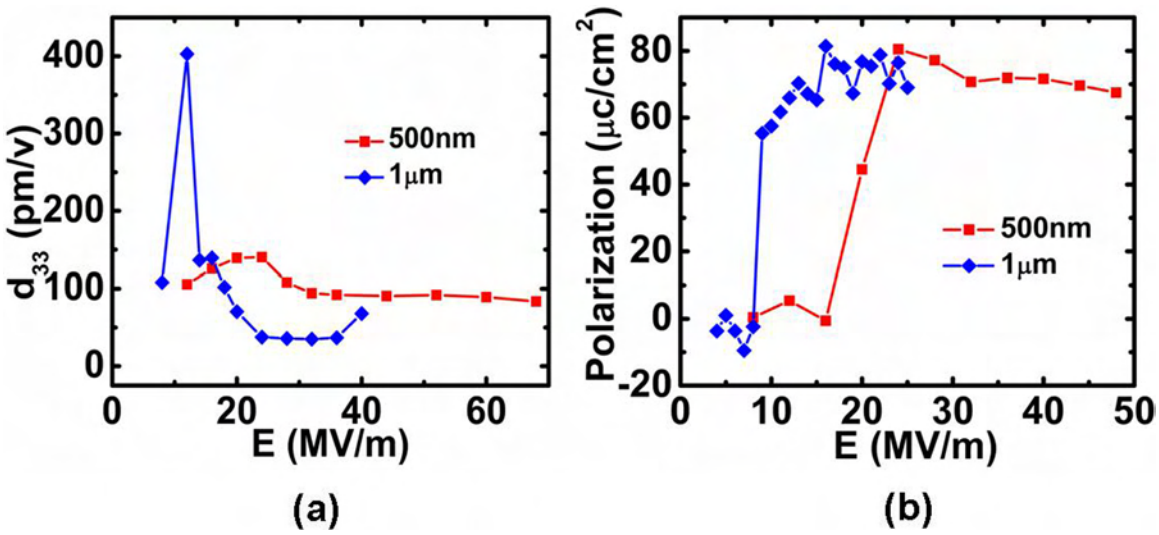

Figure 4.20: The effect of thickness on the piezoelectric and ferroelectric behavior of the patterned $1 \times 1\mu m$ square island. (a)piezoelectric coefficient d_{33} *vs*. electric field; (b) polarization *vs*. electric field

thick island. For 500nm thick film, the ratio of lateral island size to height of the island is 2, the clamping of the island from the substrate is higher than the cubic island of 1μm thick. Moreover, from previous chapter, it can be seen that the *a* domain fraction in 500nm thick is about the half of the amount of *a* domain in a 1 μm thick film, so from both constraint in the island and the amount of movable *a* domain point of view, it is expected that the extrinsic contribution from 90° domain movement in a square island of 500nm thick will be less, resulting in the lower peak value in Figure 4.20.

4.2.3 Patterned structure in 3μm thick lead magnesium niobate-lead titanate (PMN-PT) ferroelectric films

Recently, there have been intensive research works on relaxor-lead titanate type ferroelectric single crystals, among which $xPb(Mg_{1/3}Nb_{2/3})O_3 - (1-x)PbTiO_3$ (PMN-PT) and $xPb(Zn_{1/3}Nb_{2/3})O_3 - (1-x)PbTiO_3$ (PZN-PT) are the center of attentions because of their unusually high piezoelectric constants and electromechanical coupling factors. Like PZT solid solutions, these ferroelectric systems have morphotropic phase boundaries (MPB) separating stable ferroelectric phases of tetragonal and rhombohedral structures. Their superior piezoelectric properties are found on compositions of the rhombohedral side of the MPB. Specifically, giant piezoelectric constants ($>$ 2500pm/V) have been achieved on (001) oriented $xPMN-(1-x)PT$ ($x \leq 0.33$) and $xPZN-(1-x)PT$ ($x \leq 0.09$) single crystals with an engineered domain configuration.

After discovery of these superior domain-engineered ferroelectric crystals, people are trying to integrate them in MEMS devices by growing them in films. However, the clamping from a substrate will reduce the longitudinal piezoelectric response of a film and therefore hinders the development of film-based MEMS devices with high sensitivity. In this work, we will demonstrate the effect of micro-patterning by focus ion beam milling on the piezoelectric response of a $0.67PMN-0.33PT$ epitaxial film with an engineered domain configuration.

$xPMN-(1-x)PT$ epitaxial films with composition x=0.33 are grown on

single-crystal $SrTiO3$ substrates with three different crystallographic orientations, (100), (110) and (111), using an on-axis radio-frequency magnetron sputtering technique. A $SrRuO_3$ layer as bottom electrode was pre-deposited by off-axis radio-frequency (RF) magnetron sputtering from a stoichiometric sintered target. During the film deposition, the substrate temperature was maintained at 670°C with argon and oxygen pressures of 240mTorr, and 160mTorr, respectively. The film thicknesses were kept at 3.3μm in order to have fully relaxed structures and an appropriated aspect ratio for micro-patterning. All of the films were stoichiometric as of the target, which was confirmed by Energy Dispersion Spectroscopy. The X-ray results showed good epitaxy and crystallinity of these films. Platinum top electrode pads (with a diameter of 54μm) were fabricated by pulsed-laser deposition at room temperature. Ferroelectric island devices in a $3\mu m \times 3\mu m \times 3\mu m$ cubic shape are fabricated by focus ion beam milling and are annealed at 650°C for 30 minutes to heal the ion-induced damage.

Polarization results (Figure 4.21(a), with P_r for three films in the order of $(110) < (001) < (111)$) and the composition suggested a rhombohedral structure for these films. Similar to a (001) poled single crystal except for the clamping from substrate, a poled (001) epitaxial film has an engineering domain configuration consisting of 4 equivalent $\langle 111 \rangle$ domains. Therefore the (001) oriented film gives the maximum piezoelectric constant due to the extrinsic contribution from rotation of $\langle 111 \rangle$ domains. The measured remnant (at zero electric field) d_{33} value for (001)

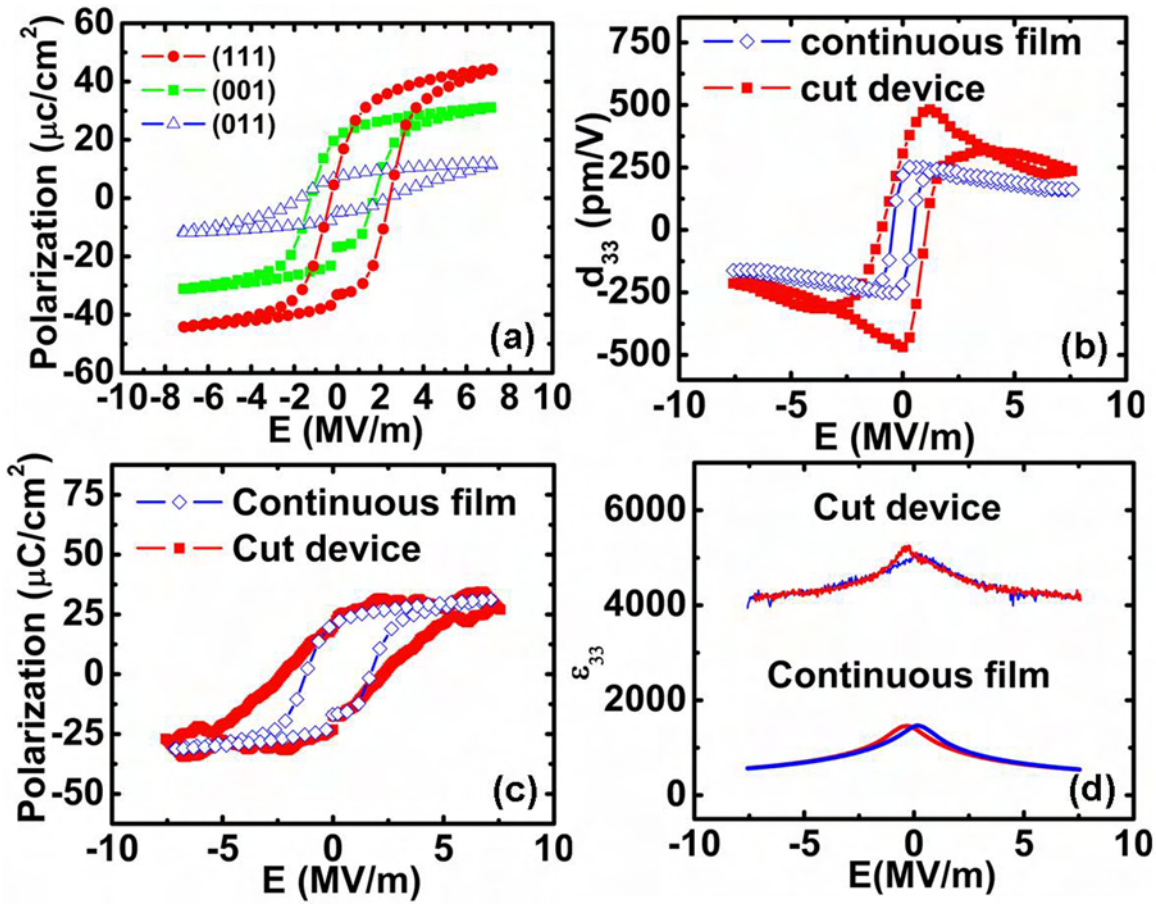

Figure 4.21: (a)Polarization hysteresis of $0.67PMN - 0.33PT$ continuous films; (b)longitudinal piezoelectric constant $d_{33} - E$; (c) Polarization $P - E$, (d) Dielectric constant $\varepsilon_{33} - E$ measurement results of the continuous film and the FIB microfabricated device.

film is about 250pm/V (Figure 4.21(b)), which is much less than that of the bulk value. The clamping from substrate degrades the piezoelectric response of the engineered domains. Therefore, in order to increase d_{33} of the film, it is necessary to reduce the clamping.

The measured remnant d_{33} value ($\sim$500pm/V) on post-annealing microfabricated PMN-PT devices was as twice large as that of continuous films (Figure 4.21(b)). Measurements on local polarization and dielectric constant are shown in Figure 4.21(c) and Figure 4.21(d), respectively. The remnant polarization did not change (Figure 4.21(c)) while the remnant dielectric constant (Figure 4.21(d)) was much larger for a microfabricated device, as compared with those of a clamped film. The enhancement of the piezoelectric and dielectric properties of the discrete island (rhombohedral structure) is due to the reduced substrate clamping and the extrinsic contribution from rotation of $\langle 111 \rangle$ domains (so-called domain engineering). Detailed mechanism of domain engineering in rhombohedral structure film can be found in [104].

4.3 Conclusion

In summary, the converse longitudinal piezoresponse of the $PbZr_{0.2}Ti_{0.8}O_3$ continuous films grown on Si-substrates and nanopatterned structure with different geometry microfabricated from these films are measured by piezoelectric force microscopy. Due to formation of periodic domain configuration in the $PbZr_{0.2}Ti_{0.8}O_3$

strip structure on Si-substrate the effective d_{33} increases up to 430pm/V, which is five times larger than the theoretical intrinsic d_{33} value for a bulk single crystal. The increase of piezoelectric properties of a patterned structure on a thick PMN-PT film is also demonstrated. Enhanced longitudinal piezoelectric responses are achieved in these microfabricated devices, which have an effective d_{33} ($\sim$500pm/V) twice larger than that of the continuous films.

Chapter 5

Finite Element Modeling of Piezoresponse of Polydomain Islands with Immobile Domain Walls and Comparison with Experiments

In this chapter, we estimate the extrinsic contribution from the 90° domain wall movement. Theoretically, the thermodynamic calculation is the only way to determine dielectric and piezoelectric properties of ferroelectric films. However, it is extremely difficult to calculate the piezoresponse of a finite discrete island structure

by traditional phenomenological theory that are developed for an infinite system. Instead, we model the nanostructure by the finite element method and simulated the intrinsic piezoresponse of discrete islands with immobile polydomain structure. The experimental results and simulation are compared to estimate the extrinsic contribution from domain wall movement.

5.1 Finite element method for piezoelectric response

Finite element analysis is a numerical technique to solve a set of differential equations when theoretical calculations cannot provide accurate results, usually in the case when the geometry or process is very complex. It is widely used in computer-based engineering analysis. The method can be used for analysis of a broad range of engineering problems, including the analysis of structural, mechanical, electrical, electromagnetic, electronic, thermal, fluid, and biomedical.

In all finite element models the solid in solid mechanics problems is divided into a finite number of elements. These elements are connected to each other at points called *nodes*. The displacements of each element are directly related to the nodal displacements. The nodal displacements are then related to the strains and the stresses in the elements. The finite element method chooses the nodal displacements in order that the stresses are in approximately equilibrium with

the applied loads, and are consistent with any constraints on the motion of the structure.

There are a number of common steps in the solution procedure using FEA no matter what finite element softwares are used[105].

Build the model

1. Specifying geometry: Defined the geometry of the structure to be analyzed by entering the geometric information in the finite element software directly, or by importing the model from an other solid modeler like Pro/ENGINEER.

2. Define element type and material properties: There are four major types of structural elements defined - beam, two-dimensional, shell, and solid. Generally the element type which will require the minimum hardware resources and minimum time to build and solve the model is chosen. Next, the material properties are defined. For example, the Young's modulus and the Poisson's ratio of the material are specified in an elastic analysis of an isotropic solid.

3. Mesh the geometry: The complicated structure is broken (or meshed) into many simple shapes (finite-elements). This includes defining the types of elements into which the structure will be broken, as well as specifying how the structure will be meshed. This mesh subdivision into elements can either be input by the user or, automatically by the computer with some finite element programs based on the geometry of the structure (automeshing).

Apply loads and obtain the solution

1. Apply boundary conditions and external loads: The boundary conditions (e.g. location of supports) and the external loads are defined.

2. Generate a solution: The solution is generated based on the previously input parameters.

Review the result

1. Postprocessing: Depending on the initial conditions and applied loads, data is returned after a solution is processed, which can be viewed in a variety of graphs and displays.

2. Refine the mesh: Because the finite element methods are approximate methods, their accuracy increases with the number of elements used. In order to judge the accuracy of results from a single finite element run, extra runs for convergence check purposes are needed: each time with a mesh of higher density and see if or how the results change.

3. Interpreting results: This step is the most critical step in the entire analysis because it requires that the modeler use fundamental knowledge of mechanics to interpret and understand the output of the model. It is especially critical for applying correct results to solve real engineering problems.

Finite element methods are extremely versatile and powerful. The designers can

obtain information about the behavior of complicated geometries with almost arbitrary loading. In spite of the significant advances of finite element analysis, the disadvantages of the method cannot be ignored. The most significant limitation of FEA is that the accuracy of the solution is usually a function of the mesh resolution. In the regions of highly concentrated stress, such as around loading points and supports, care must be taken to analyze the model with the use of a sufficiently refined mesh. In addition, special efforts must be made to analyze the problems which are inherently singular such as theoretically infinite stress.

The ANSYS program is a general-purpose computer program for finite element analysis and design which can be used in all disciplines of engineering. It also has the ability to perform $coupled - field$ analysis. A coupled-field analysis is an analysis that takes into account the interaction (coupling) between two or more fields. Examples of coupled-field analysis are piezoelectric analysis thermal-stress analysis, thermal-electric analysis, and fluid-structure analysis.

The piezoelectric analysis handles the interaction between the structural and electric fields: it solves for the displacements distribution due to applied voltage, or vice versa. It is available in the ANSYS/Multiphysics, the types of analysis can be static, modal, prestressed modal, harmonic, prestressed harmonic and transient.

In this work, we use the element type of SOLID98 (Figure 5.1)[106], this is a tetrahedral coupled-field solid element. The piezoelectric only analysis can be activated by setting KEYOPT(1)=3. SOLID98 has large deflection and stress

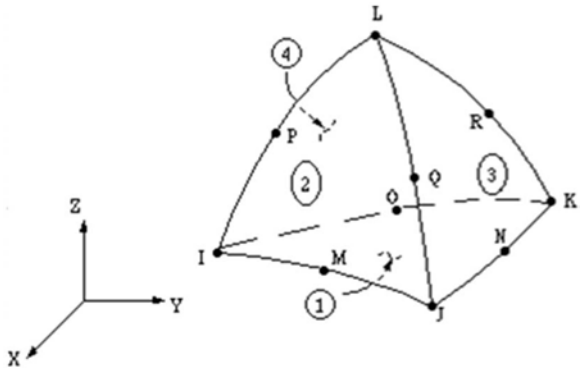

Figure 5.1: SOLID98 tetrahedral Coupled-Field solid element

stiffening capabilities. For static analysis, the sparse matrix solver is the default solver. The piezoelectric model requires permittivity (or dielectric constant), the piezoelectric matrix and the elastic coefficient matrix as materials properties. The relative permittivity is input as $\varepsilon_{11}, \varepsilon_{22}, \varepsilon_{33}$, which represents the diagonal components of the permittivity matrix $[\varepsilon]$. The values are measured at constant strain.

The piezoelectric matrix is defined either in [e] form (piezoelectric stress matrix) or in [d] form (piezoelectric strain matrix). The [e] matrix is associated with the input of the anisotropic elasticity in the form of the stiffness matrix [c], while the [d] matrix is associated with the compliance matrix [s]. Both the [e] and the [d] matrix use the data table input as follows:

$$
[e] = \begin{array}{c} \\ x \\ y \\ z \\ xy \\ yz \\ xz \end{array}
\begin{array}{c}
\begin{array}{cccccc} x & y & z & xy & yz & xz \end{array} \\
\left(\begin{array}{cccccc}
c_{11} & & & & & \\
c_{21} & c_{22} & & & & \\
c_{31} & c_{32} & c_{33} & & & \\
c_{61} & c_{62} & c_{63} & c_{66} & & \\
c_{41} & c_{42} & c_{43} & c_{46} & c_{44} & \\
c_{51} & c_{52} & c_{53} & c_{56} & c_{54} & c_{55}
\end{array} \right)
\end{array}
\tag{5.1}
$$

The 6×6 symmetric matrix of the elastic coefficient matrix uses the following data table input:

$$
[c] = \begin{array}{c} \\ x \\ y \\ z \\ xy \\ yz \\ xz \end{array}
\begin{array}{c}
\begin{array}{cccccc} x & y & z & xy & yz & xz \end{array} \\
\left(\begin{array}{cccccc}
c_{11} & & & & & \\
c_{21} & c_{22} & & & & \\
c_{31} & c_{32} & c_{33} & & & \\
c_{61} & c_{62} & c_{63} & c_{66} & & \\
c_{41} & c_{42} & c_{43} & c_{46} & c_{44} & \\
c_{51} & c_{52} & c_{53} & c_{56} & c_{54} & c_{55}
\end{array} \right)
\end{array}
\tag{5.2}
$$

For isotropic materials, another method to specify elastic constant is to define Young's modulus and Poisson's ratio and/or shear's modulus.

In ANSYS, the unit system of the data must keep consistent. For the system that is at micron size, it is convenient to use μMKSV units. Table 5.1[106] is a list

of conversion factors from standard MKS units to μMKSV units that are used in this work. In addition, the free-space permittivity needs to be properly set for the unit system used, in the μMKSV unit system, this value is: 8.72×10^{-5}PC/μN.

Table 5.1: Conversion factor for MKS to μMKSV

Parameter	MKS Unit	Dimension	Multiply by	To obtain $\mu MKSV$ Unit	Dimension
Length	m	m	10^6	μm	μm
Young's modulus	Pa	$\frac{kg}{(m)(s)^2}$	10^{-6}	MPa	$\frac{kg}{(\mu m)(s)^2}$
Current	A	A	10^{12}	pA	pA
Voltage	V	$\frac{(kg)(m)^2}{(A)(s)^3}$	1	V	$\frac{(kg)(\mu m)^2}{(pA)(s)^3}$
Capacitance	F	$\frac{(A)^2(s)^4}{kg(m)^3}$	10^{12}	pF	$\frac{(pA)^2(s)^4}{kg(\mu m)^2}$
Permittivity	F/m	m	10^6	pF/μm	$\frac{(pA)^2(s)^4}{kg(\mu m)^3}$
Electric field	V/m	$\frac{(kg)(m)}{(s)^3(A)}$	10^{-6}	V/μm	$\frac{(kg)(\mu m)}{(s)^3(pA)}$

5.2 Finite element modeling of patterned structure

5.2.1 Cubic island

Finite element modeling of a cubic island is constructed to calculate the converse longitudinal piezoresponse using a commercial software ANSYS. A model of polydomain island including all three-domain variants: c domain ((001) oriented polarization), $a1$ and $a2$ domain ((100) and (010) oriented polarization) has been considered (Figure 5.2(b)). Domain thickness ($50nm$), period (137.5nm) and a do-

main fraction (60%) in agreement with TEM and XRD observation are used in this modeling. For simplicity, the polydomain ferroelectric is considered as isotropic elastic media with Young's modulus $Y = 148GPa$, Poisson's ratio $\nu = 0.3$[107]. Piezoelectric coefficients $d_{33} = 87$pm/V, $d_{31} = -26$pm/V of PZT20/80 bulk materials are employed for the calculation[108]. The intrinsic piezoresponse is simulated for islands with fixed 90° domain boundaries. The substrate is assumed to be rigid to obtain the maximum possible intrinsic piezoresponse[109]. The normal surface strain of the island is calculated and the result is shown in (Figure 5.2(c)). The extrinsic contribution of 90° domain movement to the effective piezoelectric coefficient can be calculated from the difference between the experiment and the simulation. For instance, the calculated strain of the island is 0.0336% at 12MV/m, while the measured value is 0.1455% (obtained by integration of d_{33} data), so the contribution of 90° domain movement to the effective piezoelectric coefficient of the island is estimated to be ~ 370pm/V.

The extrinsic contribution to piezoresponse from 90° domain movement demonstrated in this work is similar to the results observed for PZT20/80 film grown on a STO substrate(Figure 5.3)[8], but the peak value of d_{33} value is higher. It shows that 90° domain movement is easier for the film grown on a Si substrate than on a STO substrate. The measured result of the polarization change under the electric field supports this argument. There are two steps on the polarization curve for islands grown on the STO substrate. The first jump of polarization near 10MV/m is

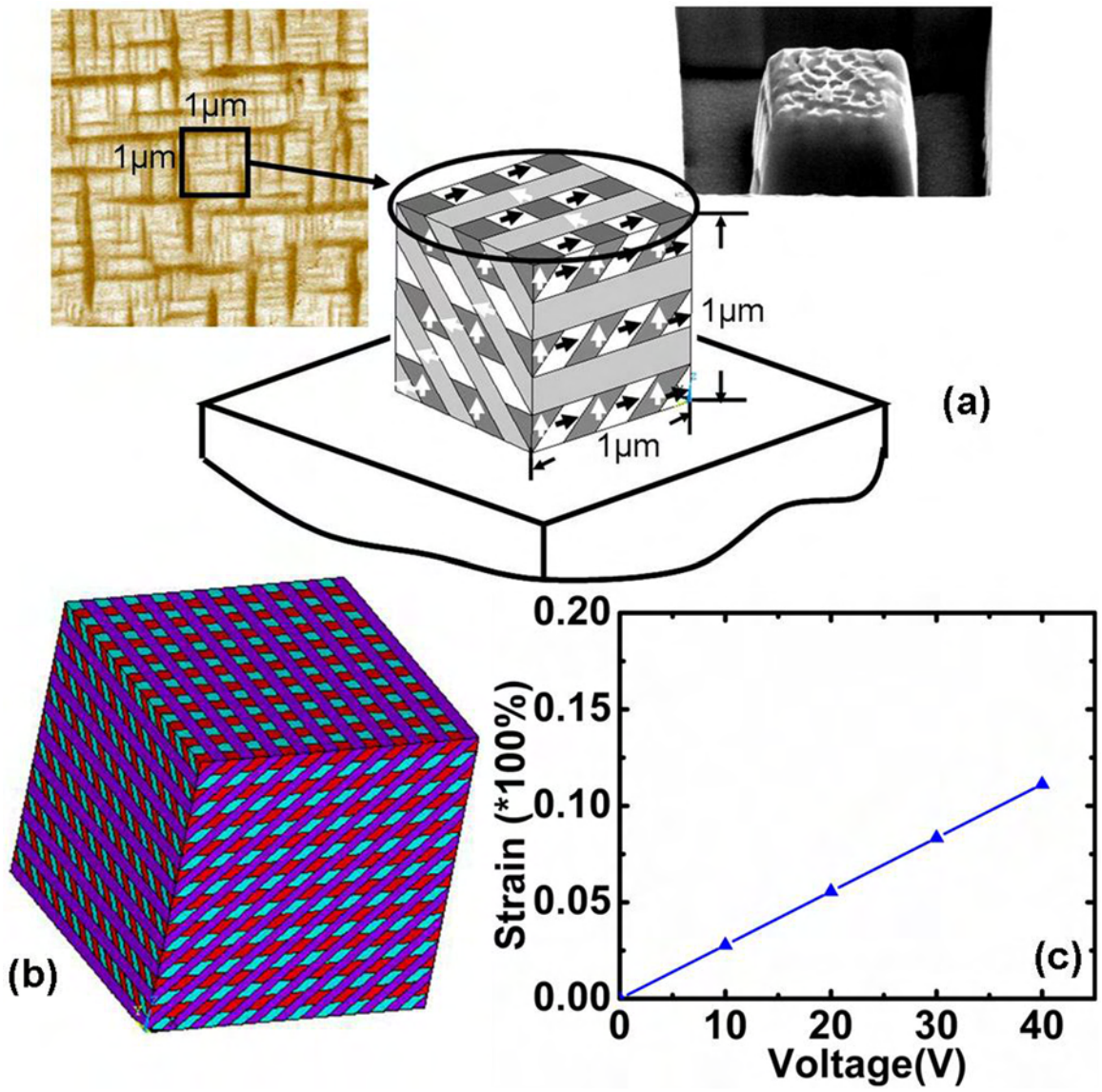

Figure 5.2: Simulation of intrinsic piezoresponse of a 1μm thick cubic island patterned on the PZT20/80 film grown on Si substrate by finite element analysis. (a) illustration of domain configuration on the cubic island; (b) FEA model; (c) simulation of the strain induced by the electric field.

due to the saturation of c domain polarizations, while the second jump of polarization around 15 MV/m shows that a domain have transformed into c domain. For the polarization evolution of the islands on Si substrates, only one step is shown around 10 MV/m. This means that the 90° domain on Si substrates can move at a lower voltage, which is close to the coercive voltage of the film.

5.2.2 Strip structure

From the PFM image observation, the domain structure of strip structure is two-domain configuration. According to this observation, the finite element modeling of the strip structure is constructed (Figure 5.4). From the simulation, the extrinsic contribution from 90° domain motion is estimated to be ∼430pm/V.

5.3 Discussion

From the comparison of experimental results with simulation result, it can be seen that extrinsic contribution from domain wall movement can be observed in all the patterned structures. A peak value at certain applied voltage is observed from longitudinal piezoelectric coefficient measurement, and polarizations of the patterned structure reach the value of the single crystal film value at similar voltage. All of these phenomena indicate that the 90° domain motion can be realized by patterning the film into nanostructures. On the other hand, the magnitudes of extrinsic contribution of the patterned structure with different geometry are different. The

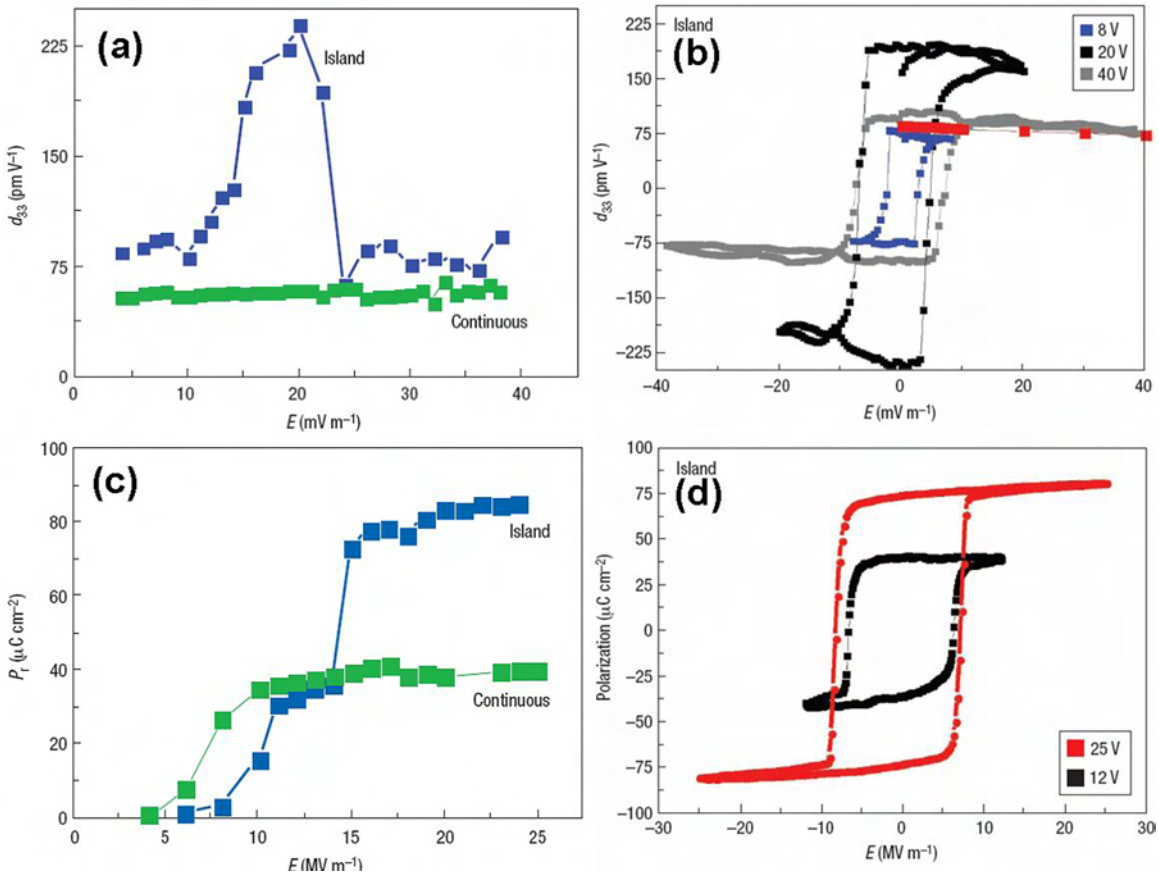

Figure 5.3: Piezoelectric and ferroelectric properties of 1μm thick cubic island patterned on the PZT20/80 film grown on STO substrate. (a) change of piezoelectric coefficient d_{33} with maximum applied electric field; (b) hysteresis loop of piezoelectric coefficient d_{33} for different electric field; (c) change of polarization with maximum applied electric field; (b) hysteresis loop of polarization for different electric field

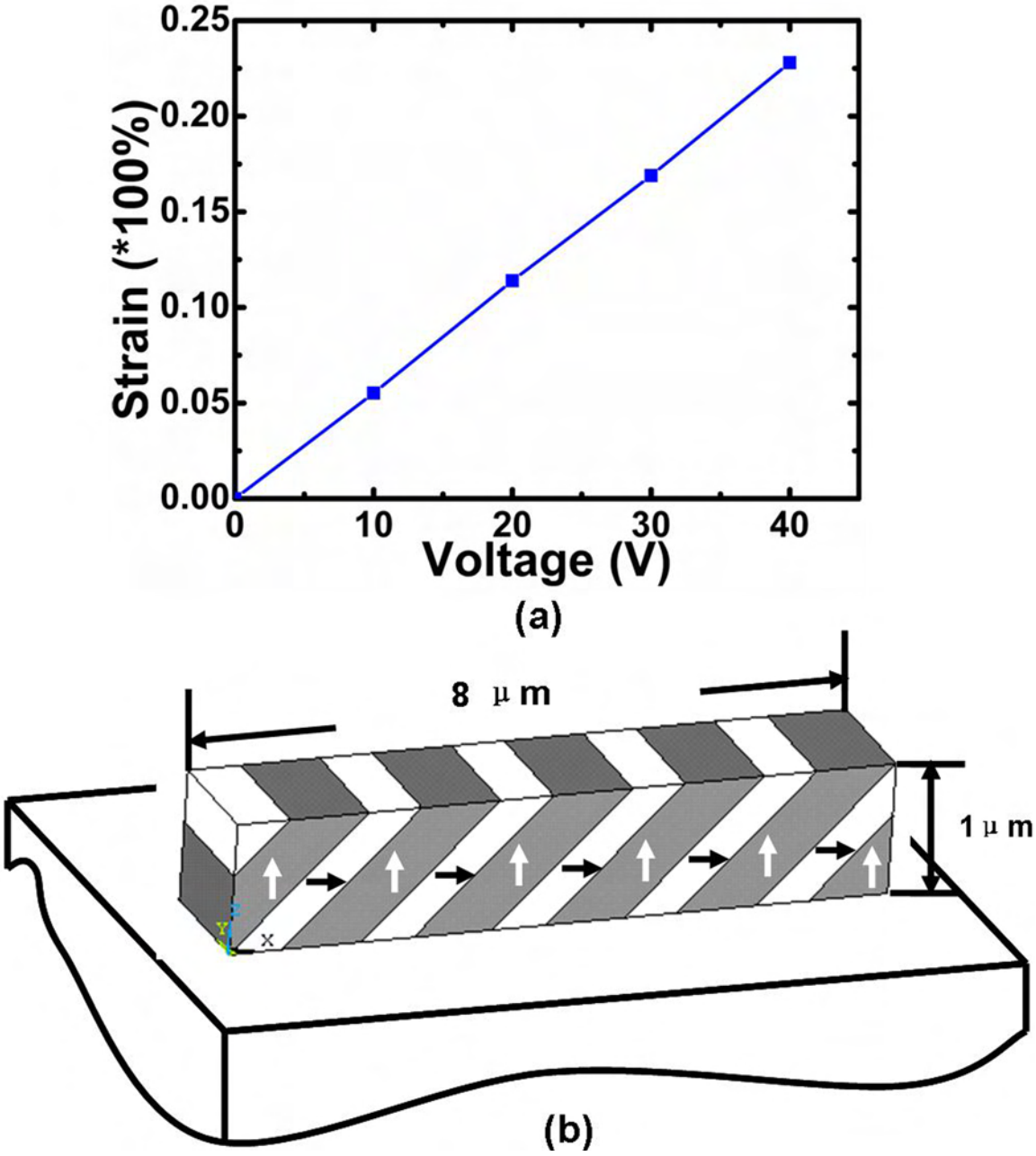

Figure 5.4: Simulation of intrinsic piezoresponse of a $8 \times 1 \mu m$ thick strip structure patterned on the PZT20/80 film grown on Si-substrate by finite element analysis. (a) simulation of the strain induced by electric field; (b) illustration of domain configuration on the strip island.

calculated results vs. experimental results are shown in Table 5.2.

For example, in the cubic $1 \times 1 \times 1\mu m$ island, the experimentally measured longitudinal piezoconstant is 7 times larger than in the continuous 1 micron thick film and 4 times larger than intrinsic piezoconstant of a single domain free standing film. In the strip island, the effective piezoconstant of $8 \times 1 \times 1\mu m$ size island is 5 times larger than the intrinsic piezoconstant of a single domain free standing film. In addition, the maximum contribution of 90° domain movement to the effective piezoelectric coefficient of the islands are estimated as ∼370 pm/V for cubic island and $\sim$ 430 pm/V for strip structure, therefore the extrinsic contribution from 90° domain movement is higher for the strip structure than for the cube island although they have same width of 1m.The difference in stress condition of the film and the patterned structure resides in that the internal stress condition. The cubic island has least film in-plane stress, while the strip structure has "uniaxial" stress constraint along one of the in-plane direction. So the extrinsic contribution should be larger in cubic island. However, in the cube island, three domain variants($c, a1$ and $a2$) are interlocked to each other, and interfere each other from moving easily; while in the strip structure, there are only two parallel domain variants (c and $a1$), the intersections between domains are largely reduced, therefore the a domains have higher mobility in strip structure, which may lead to the higher extrinsic contribution.

5.4 Conclusion

Finite element models of the polydomain patterned structures have been constructed and the intrinsic piezoresponse has been simulated. By comparing the result of simulation with the experimental results, the extrinsic contribution to the piezoresponse from the 90° domain wall movement is calculated (see Table 5.2). The extrinsic contribution is highest in the strip islands due to their special domain structure. The domain wall intersections are eliminated in the polytwin architecture.

Table 5.2: Comparison of experimental results with finite element simulation

Geometry	a Domain Fraction(%)	Experiment d_{33}(pm/V)	Simulation d_{33}(pm/V)	Extrinsic d_{33}(pm/V)	Film d_{33}(pm/V)
Cubic island,1μm	60	393-413	28	374	48-53
Cubic island,0.5μm	26	130-150	51	89	52-58
Strip island,1μm	30	472-492	55	427	48-53

Chapter 6

Summary

Domain nanostructures in ferroelectric films under different constraint conditions and their responses to electrical field have been studied experimentally via PFM imaging and measurement of ferroelectric and piezoelectric properties, and theoretically via finite element modeling. The following conclusions can be drawn from our work:

1. High quality ferroelectric $Pb(Zr_{0.2}Ti_{0.8})O_3$ epitaxial films up to 1 micron thick have been grown by pulsed laser deposition on a Si substrate.

2. A focused ion beam technique has been developed for patterning films to fabricate the micron and submicron size ferroelectric islands of different configurations including cubic and strip-like shape.

3. Measurements of the polarization and piezoelectric response of islands demonstrate dramatic enhancement of ferroelectric and piezoelectric properties in

comparison to continuous films.

4. Finite element modeling of the cubic and strip-like islands with immobile polydomain structure has been performed to calculate their intrinsic piezoresponse. Comparison of the modeling to experimental measurement of piezoeffect allows us to determine the extrinsic piezoeffect due to domain wall movement.

5. Piezoelectric force microscopy study of domain structure has revealed the three-domain cellular architecture in the cubic island and the plane-parallel two-domain structure in the strip-like island. These observations are in good agreement with theoretical analysis of an equilibrium domain structure dependent of the symmetry of the in-plane stress state due to a film substrate misfit.

6. Observation of domain wall movement in the strip island confirms that the plane-parallel domain walls are very mobile due to absence of their intersections.

7. Piezoelectric force microscopy study of domain structure in the continuous films with thickness 500nm and 1 micron has revealed polytwin plates consisting of alternation $a1/a2$ in plane domains with relatively mobile domain walls.

8. Piezoelectric force microscopy studies have been shown that it is possible to

transform of the cellular domain structure into the hierarchical one and back by applying, via a PFM tip, local electric field to a small area of the continuous film. The observation is in agreement with the conclusion following from the phase field modeling of the morphological transition between cellular and hierarchical domain architectures with change of the out-of-plane domain fraction.

9. The investigation of piezoresponse of patterned ferroelectric films and the observation of changeable domain structure under local electric field in continuous films allows us to suggest that a relative small extrinsic contribution of the domain wall movement in the continuous films is a result of the elastic substrate clamping rather than domain wall pinning. Thus, the contribution of domain wall movement can be increased by engineering special domain architectures. The structure of plane-parallel domains in a film, which are patterned to the thin strips is an example of specially design nanostructure with optimum functional properties. Fabrication and investigation of such kind of patterned structures can be recommended for future research direction.

The following papers are the results of my Ph.D. research which have been published or will be submitted:

1. Z. Ma et al., "Effect of 90° domain movement on the piezoelectric response of patterned $PbZr_{0.2}Ti_{0.8}O_3/SrTiO_3/Si$ heterostructures", *Applied Physics Letters*, Vol.87, No.7, p72907 (2005)

2. Z. Ma et al., "Field-induced morphological transition of 90° domain in ferroelectric film on Si substrate", to be submitted for *Applied Physics Letters*

3. Z.Ma et al., "Elastic domain engineering with nanopatterning of $PbZr_{0.2}Ti_{0.8}O_3/SrTiO_3/Si$ ferroelectric heterostructures", to be submitted for *Journal of Applied Physics*

4. Jun Ouyang, Z.K. Ma, R. Ramesh, and A. L. Roytburd,"Theoretical modeling of coexisting tetragonal and rhombohedral heterophase polydomain structures in lead zirconate ferroelectric films near the morphotropic phase boundary", submitted to *Physical Review B*

5. J. Wang, H. Zheng, Z. Ma, S. Prasertchoung, M. Wuttig, R. Droopad, J. Yu, K. Eisenbeiser, and R. Ramesh, "Epitaxial $BiFeO_3$ thin films on Si", *Applied Physics Letters*, Vol.85, p2574 (2004)

6. S. Prasertchoung, V. Nagarajan, Z. Ma, R. Ramesh, J. S. Cross, and M. Tsukada, "Polarization switching of submicron ferroelectric capacitors using an atomic force microscope", *Applied Physics Letters*, Vol. 84, p3130 (2004)

7. H.Zheng, J.Wang, S.E. Lofland, Z.Ma, L. Mohaddes-Ardabili, T. Zhao, L. Salamanca-Riba, S. R. Shinde, S. B. Ogale, F. Bai,D. Viehland, Y. Jia, D. G. Schlom, M. Wuttig, A. Roytburd, R. Ramesh, "Multiferroic $BaTiO_3$-$CoFe_2O_4$ nanostructures", *Science*, Vol.303, no.5658, p661(2004)

8. D. C.Kundaliya, S.B.Ogale, S.E.Lofland, S.Dhar, C.J.Metting, S.R.Shinde, Z.Ma, B.Varughese, K.V.Ramanujachary, L.Salamanca-Riba, T.Venkatesan, "On the origin of high-temperature ferromagnetism in the low-temperature-processed Mn-Zn-O system", *Nature Materials*, Vol.3, p709-714 (2004)

9. Jun Ouyang, D.M. Kim, I. Levin, S. Trolier-McKinstry, Z. K. Ma, S. Y. Yang, J. Melngailis, C. B. Eom, A. L. Roytburd, and R. Ramesh, "Ultrahigh piezoelectric response in epitaxial ferroelectric thin films", to be submitted for *Nature Materials*

10. Jun Ouyang, D.M. Kim, Z. K. Ma, J. Melngailis, A. L. Roytburd, C. B. Eom and R. Ramesh, "Effect of micropatterning by focused ion beam milling on piezoelectric response of $0.67(Mg_{1/3}Nb_{2/3})$-$0.33PbTiO_3$ epitaxial films engineered for MEMS applications", to be submitted for *Applied Physics Letters*

BIBLIOGRAPHY

[1] A. L. Roitburd. Equilibrium structure of epitaxial layers. *Physica Status Solidi A*, 37:329, 1976.

[2] A. L. Roytburd and Y. Yu. Twinning in advanced materials. *TMS*, 221:217, 1994.

[3] N. A. Pertsev and A. Yu. Emelyanov. Domain wall contribution to the piezoelectric response of epitaxial ferroelectric thin films. *Appl. Phys. Lett.*, 71:3646, 1997.

[4] F. Xu, S. Trolier-McKinstry, W. Ren, Baomin Xu, Z.-L. Xie, and K. J. Hemker. Domain wall motion and its contribution to the dielectric and piezoelectric properties of lead zirconate titanate films. *J. Appl. Phys.*, 89:1336, 2001.

[5] K. S. Lee, Y. K. Kim, S.Baik, J. Kim, and I. S.Jung. In situ observation of ferroelectric 90°-domain switching in epitaxial Pb(Zr, Ti)O_3 thin films by synchrotron x-ray diffraction. *Appl. Phys. Lett.*, 79:2444, 2001.

[6] A. L. Roytburd, S. P. Alpay, V. Nagarajan, C. S. Ganpule, S. Aggarwal, E. D. Williams, and R. Ramesh. Measurement of internal stresses via the polarization in epitaxial ferroelectric films. *Phys. Rev. Lett.*, 85:190, 2000.

[7] J. Melngailis. Focused ion beam technology and applications. *J.Vac. Sci. and Technol. B*, 5:469, 1987.

[8] V. Nagarajan, A. Roytburd, A. Stanishevsky, S. Prasertchoung, T. Zhao, L. Chen, J. Melngailis, O. Auciello, and R. Ramesh. Dynamics of ferroelastic domains in ferroelectric thin films. *Nat. Mater.*, 2:43, 2003.

[9] Chandan S. Ganpule. *Nanoscale Phenomena in Ferroelectric Thin Films*. PhD thesis, University of Maryland, 2001.

[10] B. Jaffe, W. R. Cook, and H. Jaffe. *Piezoelectric Ceramics*. Academic Press, 1971.

[11] Ferroelectrics Standards Committee of the IEEE Ultrasonics and Frequency Control Society. *An American National Standard IEEE Standard on Piezoelectricity*. The Institute of Electrical and Electronics Engineers, Inc, 1987.

[12] J. F. Nye. *Physical Properties of Crystals: Their Representation by Tensors and Matrices*. Oxford University Press, Great Britain, 1st edition, 1957.

[13] Dragan Damjanovic. Ferroelectric,dielectric and piezoelectric properties of ferroelectric thin films and ceramics. *Rep. Prog.Phys.*, 61:1267–1324, 1998.

[14] S.-E. Park and T. R. Shrout. Ultrahigh strain and piezoelectric behavior in relaxor based ferroelectric single crystals. *J. Appl. Phys.*, 82:1804, 1997.

[15] R. W. Whatmore. Pyroelectric devices and materials. *Rep. Prog. Phys.*, 49:1335, 1986.

[16] IEEE Standard Definitions of Primary Ferroelectric Terms. *An American National Standard IEEE Standard on Piezoelectricity*. The Institute of Electrical and Electronics Engineers, Inc, 1986.

[17] F. Jona and G. Shirane. *Ferroelectric Crystals*. New York: Pergamon, 1962.

[18] Y. Shiozaki, E. Nakamura, and T. Mitsui. Landolt-bornstein: GroupIII condensed matter. In *Ferroelectrics and Related Substances:Oxides*.

[19] M. E. Lines and A. M. Glass. *Principles and Applications of Ferroelectrics and Related Materials*. Oxford, 1977.

[20] B. A. Strukov and A. P. Levanyuk. *Ferroelectric Phenomena in Crystals*. Springer-Verlag Berlin Heidelberg, 1998.

[21] T. Tsurumi, Y. Kumano, N. Ohashi, T. Takenaka, and O. Fukunaga. 90° domain reorientation and electric-field-induced strain of tetragonal lead zirconate titanate ceramics. *Jpn. J. Appl. Phys.*, 36:5970, 1997.

[22] T. Tsurumi, Y. Kumano, N. Ohashi, and O. Fukunaga. Contribution of 90° domains in electric-field-induced strain of PZT ceramics. *Journal of the Korean Physical Society*, 32:S1241, 1998.

[23] E. Burcsu, G. Ravichandran, and K. Bhattacharya. Large strain electrostrictive actuation in barium titanate. *Appl. Phys. Lett.*, 77:1698, 2000.

[24] L. Chen, J. Ouyang, Z. Ma, and A. L. Roytburd. submitted.

[25] E. A. Little. Dynamic behavior of domain walls in barium titanate. *Phys. Rev.*, 98:978, 1955.

[26] Ennio Fatuzzo and Walter J. Merz. *Ferroelectricity.* John Wiley and Sons, Inc., 1967.

[27] X. L. Zhang, Z. X. Chen, and L. E. Cross. Dielectric and piezoelectric properties of modified lead titanate zirconate ceramics from 4.2 to 300k. *J. Mater. Sci.*, 18:968, 1983.

[28] Q. M. Zhang, H. Wang, N. Kim, and L. E. Cross. Direct evaluation of domain-wall and intrinsic contributions to the dielectric and piezoelectric response and dependence on lead zirconate-titanate ceramics. *J. Appl. Phys.*, 75:454, 1994.

[29] D. Damjanovic, M. Demartin, F. Chu, and N. Setter. Practical consequences of the extrinsic contributions to the properties of piezoelectric sensors and actuators. New York, NY, USA, 1996. ISAF'96. Proceedings of the tenth IEEE International Symposium on-Applications of Ferroelectrics.

[30] Xiao Hong Du, Jiehui Zheng, Uma Belegundu, and Kenji Uchinoa. Crystal orientation dependence of piezoelectric properties of lead zirconate titanate near the morphotropic phase boundary. *Appl. Phys. Lett.*, 72:2421, 1998.

[31] A. Gruverman, O. Auciello, and H. Tokumoto. Nanoscale investigation of fatigue effects in $Pb(Zr,Ti)O_3$ films. *Appl. Phys. Lett.*, 69:3191, 1996.

[32] L. A. Bursill and P. J. Lin. Electron microscopic studies of ferroelectric crystals. *Ferroelectrics*, 70:191, 1986.

[33] F. Tsai, V. Khiznichenko, and J. M. Cowley. High-resolution electron microscopy of 90° ferroelectric domain boundaries in $BaTiO_3$ and $Pb(Zr_{0.52}Ti_{0.48})O_3$. *Ultramicroscopy*, 45:55, 1992.

[34] S. Stemmer, S.K. Streiffer, F. Ernst, and M. Ruhle. Atomistic structure of 90° domain walls in ferroelectric $PbTiO_3$ thin films. *Phil. Mag. A*, 71:713, 1995.

[35] M. Foeth, A. Sfera, P. Stadelmann, and P-A. Buffat. A comparison of hrem and weak beam transmission electron microscopy for the quantitative measurement of the thickness of ferroelectric domain walls. *J. Electron Microscopy*, 48:717, 1999.

[36] N. Floquet, C. M. Valot, M. T. Mesnier, J. C. Niepce, L. Norrnand, A. Thorel, and R. Kilaas. Ferroelectric domain walls in $BaTiO_3$: Fingerprints diagrams and quantitative HRTEM image analysis. *J Phys. III France*, 7:1105, 1997.

[37] N. Floquet and C. Valot. Ferroelectric domain walls in $BaTiO_3$: structural wall model interpreting fingerprints in XRPD diagrams. *Ferroelectrics*, 234:107, 1999.

[38] J. Padilla and D. Vanderbilt. Ab initio study of $BaTiO_3$ surfaces. *Phys. Rev. B*, 56:1625, 1997.

[39] W. Zhong, D. Vanderbilt, and K. M. Rabe. Phase transitions in $BaTiO_3$ from first principles. *Phys. Rev. Lett.*, 73:1861, 1994.

[40] B. Meyer and D. Vanderbilt. Ab initio study of ferroelectric domain walls in $PbTiO_3$. *Physical Review B*, 65:104111, 2002.

[41] S. Poykko and D. J. Chadi. Ab initio study of dipolar defects and 180° domain walls in $PbTiO_3$. *J. Phys. Chem. Solids*, 61:291, 2000.

[42] Rainer Waser. *Nanoelectronics and Information Technology: Advanced Electronic Materials and Novel Devices*. Wiley-VCH Gmbh and Co. KGaA, 2003.

[43] G. Arlt, H. Dederichs, and R. Herbiet. 90° domain wall relaxation in tetragonally distorted ferroelectric ceramics. *Ferroelectrics*, 74:37, 1987.

[44] G. Arlt and N. A. Pertsev. Force constant and effective mass of 90° domain walls in ferroelectric ceramics. *J. Appl. Phys.*, 70:2283, 1991.

[45] D. Damjanovic. Stress and frequency dependence of the direct piezoelectric effect in ferroelectric ceramics. *J. Appl. Phys.*, 82:1788, 1997.

[46] D. Damjanovic and M. Demartin. Contribution of the irreversible displacement of domain walls to the piezoelectric effect in barium titanate and lead zirconate titanate ceramics. *J. Phys.: Condens. Matter*, 9:4943, 1997.

[47] M. J. Haun. *Thermodynamic theory of the lead zirconate-lead titanate solid solution system*. PhD thesis, Penn. State Univ. at University Park, 1988.

[48] O. Auciello, J. F. Scott, and R. Ramesh. The physics of ferroelectric memories. *Physics Today*, 51:22, 1998.

[49] P. Muralt. Ferroelectric thin films for micro-sensors and actuators: A review. *J. Micromech. Microeng.*, 10:136–146, 2000.

[50] N. A. Pertsev, V. G. Kukhar, H. Kohlstedt, and R. Waser. Phase diagrams and physical properties of single-domain epitaxial $Pb(Zr_{1-x}Ti_x)O_3$ thin films. *Physical Review B*, 67:054107, 2003.

[51] K. Binder. Surface effects on phase transitions in ferroelectrics and antiferroelectrics. *Ferroelectrics*, 35:99, 1981.

[52] A. L. Kholkin, M. L. Calzada, P. Ramos, J. Mendiola, and N. Setter. Piezoelectric properties of Ca-modified $PbTiO_3$ thin films. *Appl. Phys.Lett.*, 69:3602, 1996.

[53] S. Trolier-Mckinstry, J. F. Shepard Jr, J. L. Lacey, T. Su, G. Zavala, and J. Fendler. Piezoelectricity in ferroelectric thin films: domain and stress issues. *Ferroelectrics*, 206-207:381–92, 1998.

[54] K. Lefki and G. J. M. Dormans. Measurement of piezoelectric coefficients of ferroelectric thin films. *J. Appl. Phys.*, 76:1764, 1994.

[55] T. M. Shaw, S. Trolier-Mckinstry, and P. C. McIntyre. The properties of ferroelectric films at small dimensions. *Annu. Rev. Mater. Sci.*, 30:263–298, 2000.

[56] G. H. Haertling. Ferroelectric ceramics: History and technology. *J. Am. Ceram. Soc.*, 82:797, 1999.

[57] A. I. Kingon, J. P. Maria, and S. K. Streiffer. Alternative dielectrics to silicon dioxide for memory and logic devices. *Nature*, 406:1032, 2000.

[58] J. F. Scott and C. A. Paz de Araujo. Ferroelectric memories. *Science*, 246:1400, 1989.

[59] P. Muralt. PZT thin films for microsensors and actuators: Where do we stand? *IEEE Transactions on Ultrasonics, Ferroelectrics and Frequency Control*, 47:903, 2000.

[60] P. Muralt. Micromachined infrared detectors based on pyroelectric thin films. *Rep. Prog. Phys.*, 64:1339, 2001.

[61] O. Auciello, C. M. Foster, and R. Ramesh. Processing technologies for ferroelectric thin films and heterostructures. *Annu. Rev. Mater. Sci.*, 28:501, 1998.

[62] R. N. Castellano and L. G. Feinstein. Ion-beam deposition of thin films of ferroelectric lead zirconate titanate (PZT). *J. Appl. Phys.*, 50:4406, 1979.

[63] S. B. Krupanidhi, N. Maffei, M. Sayer, and K. El-Assal. RF planar magnetron sputtering and characterization of ferroelectric $Pb(Zr,Ti)O_3$films. *J. Appl. Phys.*, 54:6601, 1983.

[64] M. Okuyama, Y. Matsui, H. Nakano, and T. Nakagawa. Preparation of $PbTiO_3$ ferroelectric thin film by RF sputtering. *Jpn. J. Appl. Phys.*, 18:1633, 1979.

[65] K. Sreenivas, M. Sayer, and P. Garrett. Properties of DC magnetron-sputtered lead zirconate titanate thin films. *Thin Solid Films*, 172:251, 1989.

[66] K. D. Budd, S. K. Dey, and D. A. Payne. Sol-gel processing of $PbTiO_3$, $PbZrO_3$, PZT, and PLZT thin films. *British Ceramic Proceedings*, 36:107, 1985.

[67] S. K. Dey, K. D. Budd, and D. A. Payne. Thin-film ferroelectrics of PZT of sol-gel processing. *IEEE Transactions on Ultrasonics, Ferroelectrics and Frequency Control*, 35:80, 1988.

[68] B. S. Kwak, E. P. Boyd, and A. Erbil. Metalorganic chemical vapor deposition of $PbTiO_3$ thin films. *Appl. Phys. Lett.*, 53:1702, 1988.

[69] M. Kojima, M. Okuyama, T. Nakagawa, and Y. Hamakawa. Chemical vapor deposition of $PbTiO_3$ thin film. *Jpn. J. Appl. Phys.*, 22:14, 1983.

[70] C. J. Brierley, C. Trundle, L. Considine, and R. W. Whatmore. The growth of ferroelectric oxides by MOCVD. *Ferroelectrics*, 91:181, 1989.

[71] S. Otsubo, T. Maeda, T. Minamikawa, and Y. Yonezawa. Preparation of $Pb(Zr_{0.52}Ti_{0.48})O_3$ films by laser ablation. *Jpn. J. Appl. Phys.*, 29:L133–6, 1990.

[72] H. Buhay, S. Sinharov, W. H. Kasner, and M. H. Francombe. Pulsed laser deposition and ferroelectric characterization of bismuth titanate films. *Appl. Phys. Lett.*, 58:1470, 1991.

[73] D. Roy, S. B. Krupanidhi, and J. P. Dougherty. Excimer laser ablated lead zirconate titanate thin films. *J. Appl. Phys.*, 69:7930, 1991.

[74] D. Dijkkamp, T. Venkatesan, X. D. Wu, S. A. Shaheen, N. Jisrawi, Y. H. Minlee, W. L. Mclean, and M. Croft. Preparation of Y-Ba-Cu oxide superconductor thin-films using pulsed laser evaporation from high-Tc bulk material. *Appl. Phys. Lett.*, 51:619, 1987.

[75] V. Nagarajan, I. G. Jenkins, S. P. Alpay, H. Li, S. Aggarwal, L. Salamanca-Riba, A. L. Roytburd, and R. Ramesh. Thickness dependence of structural and electrical properties in epitaxial lead zirconate titanate films. *J. Appl. Phys.*, 86:595, 1999.

[76] Y. Wang, C. Ganpule, B. T. Liu, H. Li, K. Mori, B. Hill, M. Wuttig, R. Ramesh, J. Finder, Z. Yu, R. Droopad, and K. Eisenbeiser. Epitaxial ferroelectric $Pb(Zr,Ti)O_3$ thin films on Si using $SrTiO_3$ template layers. *Appl. Phys. Lett.*, 80:97, 2002.

[77] M. Alexe and A. Gruverman (Eds.). *Nanoscale Characterization of Ferroelectric Materials: Scanning Probe Microscopy Approach*. Springer-Verlag, 2004.

[78] P. Gthner and K. Dransfeld. Local poling of ferroelectric polymers by scanning force microscopy. *Appl. Phys. Lett.*, 61:1137, 1992.

[79] A. Gruverman, H. Tokumoto, A. S. Prakash, S. Aggarwal, B. Yang, M. Wuttig, R. Ramesh, O. Auciello, and T. Venkatesan. Nanoscale imaging of domain dynamics and retention in ferroelectric thin films. *Appl. Phys. Lett.*, 71:3492, 1997.

[80] P. Paruch, T. Tybell, and J.-M. Triscone. Nanoscale control of ferroelectric polarization and domain size in epitaxial $Pb(Zr_{0.2}Ti_{0.8})O_3$ thin films. *Appl. Phys. Lett.*, 79:530, 2001.

[81] A. K. Sarin Kumar, P. Paruch, J.-M. Triscone, W. Daniau, S. Ballandras, L. Pellegrino, D. Marr, and T. Tybell. High-frequency surface acoustic wave device based on thin-film piezoelectric interdigital transducers. *Appl. Phys. Lett.*, 85:1757, 2004.

[82] A. Gruverman, O. Auciello, and H. Tokumoto. Scanning force microscopy for the study of domain structure in ferroelectric thin films. *J. Vac. Sci. Technol. B*, 14:602, 1996.

[83] R. Luthi, H. Haefke, K. P. Meyer, E. Meyer, L. Howald, and H. J. Guntherodt. Surface and domain structures of ferroelectric crystals studied with scanning force microscopy. *J. Appl. Phys.*, 74:7461, 1993.

[84] G. Zavala, J. H. Fendler, and S. Trolier-McKinstry. Characterization of ferroelectric lead zirconate titanate films by scanning force microscopy. *J. Appl. Phys.*, 81:7480, 1997.

[85] S. V. Kalinin and D. A. Bonnell. Imaging mechanism of piezoresponse force microscopy of ferroelectric surfaces. *Phys. Rev. B*, 65:125408, 2002.

[86] S. P. Alpay and A. L. Roytburd. Thermodynamics of polydomain heterostructures. III. domain stability map. *J. Appl. Phys.*, 83:4714, 1998.

[87] C. S. Ganpule, V. Nagarajan, B. K. Hill, A. L. Roytburd, E. D. Williams, R. Ramesh, S. P. Alpay, A. Roelofs, R. Waser, and L. M. Eng. Imaging three-dimensional polarization in epitaxial polydomain ferroelectric thin films. *J. Appl. Phys.*, 91:1477, 2002.

[88] A. Roelofs, N. A. Pertsev, R. Waser, F. Schlaphof, L. M. Eng, C. Ganpule, V. Nagarajan, and R. Ramesh. Depolarizing-field-mediated 180° switching in ferroelectric thin films with 90° domains. *Appl. Phys. Lett.*, 80:1424, 2002.

[89] A. L. Kholkin, K. G. Brooks, D. V. Taylor, and S. Hiboux. Self-polarization effect in $Pb(Zr,Ti)O_3$ thin films. *Integrated Ferroelectrics*, 22:525, 1998.

[90] J. Slutsker, A. Artemev, and A. L. Roytburd. Elastic domain architectures in constrained layers. Washington, DC, USA, 2002. Fundamental Physics of Ferroelectrics 2002.

[91] J. Slutsker, A. Artemev, and A. L. Roytburd. Engineering of elastic domain structures in a constrained layer. *Acta Materialia*, 52:1731, 2004.

[92] Jon Orloff, Lynwood Swanson, and Mark Utlaut. *High Resolution Focused Ion Beams: FIB and Its Applications*. Kluwer Academic Publishers, 2002.

[93] Micrion Corp., Peabody, MA. *Micrion 2100/2500 FIB system operation manual*, 1996.

[94] C. S. Ganpule, A. Stanishevsky, S. Aggarwal, J. Melngailis, E. Williams, R. Ramesh, V. Joshi, and Carlos Paz de Araujo. Scaling of ferroelectric and piezoelectric properties in $Pt/SrBi_2Ta_2O_9/$ Pt thin films. *Appl. Phys. Lett.*, 75:3874, 1999.

[95] A. Stanishevsky, S. Aggarwal, A. S. Prakash, J. Melngailis, and R. Ramesh. Focused ion-beam patterning of nanoscale ferroelectric capacitors. *J. Vac. Sci. Technol. B*, 16:3899, 1998.

[96] A. Stanishevsky, B. Nagaraj, J. Melngailis, R. Ramesh L. Khriachtchev, and E. McDaniel. Radiation damage and its recovery in focused ion beam fabricated ferroelectric capacitors. *J. Appl. Phys.*, 92:3275, 2002.

[97] A. L. Kholkin, E. K. Akdogan, A. Safari, P.-F. Chauvy, and N. Setter. Characterization of the effective electrostriction coefficients in ferroelectric thin films. *J. Appl. Phys.*, 89:8066, 2001.

[98] A. Gruverman, O. Auciello, and H. Tokumoto. Scanning force microscopy: application to nanoscale studies of ferroelectric domains. *Integr. Ferroelectr.*, 19:49, 1998.

[99] C. S. Ganpule, A. Stanishevsky, Q. Su, S. Aggarwal, J. Melngaillis, E. Williams, and R. Ramesh. Scaling of ferroelectric properties in thin films. *Appl. Phys. Lett.*, 77:3275, 2000.

[100] S. Tiedke, T. Schmitz, K. Prume, A. Roelofs, T. Schneller, U. Kall, R. Waser, C. S. Ganpule, V. Nagarajan, A. Stanishevsky, and R. Ramesh. Direct hysteresis measurements of single nanosized ferroelectric capacitors contacted with an atomic force microscope. *Appl. Phys. Lett.*, 79:3678, 2001.

[101] aixACCT Systems GmbH, Aachen, Germany. *TF Analyzer 2000 FE-module instructional manual*, 2000.

[102] D. J. You, W. W. Jung, S. K. Choi, and Y. Cho. Domain structure in a micron-sized $PbZr_{1-x}Ti_xO_3$ single crystal on a Ti substrate fabricated by hydrothermal synthesis. *Appl. Phys. Lett.*, 84:3346, 2004.

[103] K. Mori, J. Li, A. L. Roytburd, and M. Wuttig. Patterned shape memory alloy films. *Materials Transactions*, 43:951–5, 2002.

[104] Jun Ouyang. *Orientation Dependence of the Piezoelectric properties of Epitaxial Ferroelectric Thin Films*. PhD thesis, University of Maryland, 2005.

[105] S. Moaveni. *Finite element analysis: theory and application with ANSYS*. Prentice Hall, 2003.

[106] Swanson Analysis Systems. Inc. *ANSYS5.0 Reference Manual*, 1992.

[107] J.-H. Li, L. Chen, V. Nagarajan, R. Ramesh, and A. L. Roytburd. Finite element modeling of piezoresponse in nanostructured ferroelectric films. *Appl. Phys. Lett.*, 84:2626, 2004.

[108] M. J. Haun, Z. Q. Zhuang, E. Furman, S. J. Jang, and L. E. Cross. Thermodynamic theory of the lead zirconate-titanate solid solution system. III. Curie constant and sixth-order polarization interaction dielectric stiffness coefficients. *Ferroelectrics*, 99:45, 1989.

[109] Lang Chen, J. H. Li, J. Slutsker, J. Ouyang, and A. L. Roytburd. Contribution of substrate to converse piezoelectric response of constrained thin films. *J. Mater. Res.*, 19:2853, 2004.